Global validation over ocean of the Jason-2 GDR-F data reprocessing

CLS Reference :	CLS-ENV-RP-24-0776
Contract :	SALP
Project Reference :	SALP-RP-MA-EA-23622-CLS
Issue :	1.1
Date :	May 19, 2025

Customer:	CNES	Contract No.:	SALP
Document Reference :			
Project	SALP-RP-MA-EA-23622-CLS		
CLS	CLS-ENV-RP-24-0776		
Date:	May 19, 2025	**Issue**	1.1

Project:	SALP		
Title:	Global validation over ocean of the Jason-2 GDR-F data reprocessing		
Author(s):	J. Coquelin, ALTEN for CLS H. Roinard, CLS		
Approved by:	P. Prandi **CLS**	**Authorized by:**	J-F. Legeais SALP Coordinator, **CLS**
Accepted by	F. Bignalet-Cazalet **CNES**		
Filename:	SALP-RP-MA-EA-23622-CLS-ENV-RP-24-0776		

Change Log

Version	Date	Changes
1.0	2025/01/31	First version
1.1	2025/05/19	add of USO drift correction patch + CNES review

Table of Content

List of Figures

List of Tables

1 Introduction

By succeeding to TOPEX/Poseidon and Jason-1 on their primary ground track, Jason-2 has extended the high-precision ocean altimetry data record. It was launched on June, 20th 2008 and its last measurement was on October, 1st 2019. Jason-2 was the reference mission on TOPEX/Poseidon historical ground track for mean sea level applications from 2008 to 2016. It was also used to observe mesoscale ocean dynamics.

Previously in version "D", Jason-2 GDR (Geophysical Data Record) have been recently reprocessed with GDR-F standard to improved data performance. This document presents the synthesis report concerning validation activities of Jason-2 Level 2 data, reprocessed in standard GDR-F. This work has been done in the frame of the SALP contract supported by CNES.

The present global report deals with the Jason-2 mission between cycle 0 and cycle 644 (year 2008 to 2019), thanks to comparison with previous Jason-2 GDR-D standard for the same period, as well as comparison with Jason-1 and Jason-3. It also contains the impact of the reprocessing on the mean sea level trend. It is split into 7 main sections, after this introduction, describing the keys of the reprocessing campaign:

- first, the **data used** are presented, with a status of the geophysical content of the fields that have changed between GDR-D and GDR-F.
- the **data coverage** and **measurement validity** issues are then presented.
- a global overview of the **performance improvement** is synthetized.
- the **impact of the reprocessing on the main altimeter, radiometer parameters and new geophysical models** is presented.
- the impact of the reprocessing on **Mean Sea Level** is detailed on the global and regional drift.

The two final chapters deal with new available variables:

- first, the analysis of the **differences between the MLE4 and Adaptive** retracking data
- and finally, the analysis of the **new sea state bias solution**.

Jason-2 GDR-F product contain MLE3, MLE4 and Adaptive retraking algorithm outputs. Except on the dedicated Adaptive retracking analysis chapter, only the data from MLE4 retracking algorithm are analysed.

2 Data used and processing

This document deals with the global impact of Jason-2 altimeter mission reprocessing (cycle 000 to 644) covering the period from 4th of july 2008 to 1st of october 2019. In this document, some comparisons are realized with AVISO L2P product in version 2021 (more information about L2P in dedicated handbook [10]) available at https://www.aviso.altimetry.fr/en/home.html.

2.1. Processing baseline

GDR-F reprocessing uses two processing baselines:

- Processing Baseline F v1.02 : for cycles 0 to 102, 113 to 128 and 165 to 202
- Processing Baseline F v1.04 : for cycles 103 to 112, 129 to 164 and 203 to 644

Both versions include last correction on GDR-F :

- Correction on RTK Adaptive for coastal areas
- Correction on S1S2 Tropo Correction

The only difference between these two processing baselines is a correction of fonctionnal anomaly due to gaussian grid changing en 2011 (install on BA 6.10p1 the 24/11/2022). There is no impact on GDR-F standard.
In addition, please note that files between 11/06/2013 23:09:44 (cycle 182 pass 031) and 01/10/2013 01:40:04 (cycle 193 pass 083) were post-processed to correct an anomaly that were present in the file refered as xref_doris_uso in global attributes (see part 5.4.1.). The released products include the correction.

All files contain the global attibute xref_doris_uso :

JA2_OS1_AXXCNE20191003_111600_20080622_145801_20191001_235355

except patched files with correction whose global attribute is set to

JA2_OS1_AXXCNE20250307_092900_20080622_145801_20191001_235355

2.2. GDR Standards

Table 1 gives the content of L2 data used in this report, for the previous version ("D") and for the new version ("F").

Model	Product Version "D"	Product Version "F"
Reference Ellipsoid	TOPEX/Poseidon : axis = 6378136.3 flattening = 0.0033528131778969	WGS84 : axis = 6378137 flattening = 0.00335281066474748
Orbit	DORIS and/or SLR and/or GPS tracking data (Orbit standard "POE-D" until cycle 253), DORIS and/or GPS tracking data (Orbit standard "POE-E" from cycle 254 onwards).	DORIS and/or GPS tracking data (Orbit standard "POE-F").

Model	Product Version “D”	Product Version “F”
Altimeter Instrument Corrections	Two sets : • one set consistent with MLE4 retracking • one set consistent with MLE3 retracking	Identical to version “D”. But updated Look Up Tables applied. No set needed for Adaptive retracking
Jason-2 Advanced Microwave Radiometer (AMR) Parameters	Using calibration parameters derived from long term calibration tool developed and operated by NASA/JPL	Using **new calibration parameters** derived from long term calibration tool developed and operated by NASA/JPL
Altimeter Retracking	“Ocean MLE4” retracking : MLE4 fit from 2nd order Brown analytical model : MLE4 simultaneously retrieves the 4 parameters that can be inverted from the altimeter waveforms : • Epoch (tracker range offset : altimeter range) • Composite Sigma : SWH • Amplitude : Sigma0 • Square of mispointing angle (Ku band only, a null value is used in of the C band retracking algorithm) “Ocean MLE3” retracking : MLE3 fit from 1st order Brown analytical model : MLE3 simultaneously retrieves the 3 parameters (Epoch, composite Sigma and Amplitude, see ocean MLE4 retracking) that can be inverted from the altimeter waveforms. “Ice” retracking : Geometrical analysis of the altimeter waveforms, which retrieves Epoch and Amplitude (see ocean MLE4 retracking)	“Ocean MLE4” retracking : Identical to version “D”. “Ocean MLE3” retracking : Identical to version “D” “Ice” retracking : Identical to version “D” “Adaptive” retracking : Adaptive retracking fit from Brown numerical model taking the real on-board PTR. Adaptive simultaneous retrieves the 4 parameters that can be inverted from the altimeter waveforms : • Epoch (tracker range offset : altimeter range) • Composite Sigma : SWH • Amplitude : Sigma0 • Gamma

Model	Product Version "D"	Product Version "F"
Sea State Bias	Two empirical models derived from Jason-2 data (one consistent with MLE4 retracking + one consistent with MLE3 retracking)	• MLE3 version derived from 1 year of MLE3 Jason-2 altimeter data with version "D" geophysical models • CLS empirical solution fitted on one year of Jason-3 GDR-F data. Two solutions for each retracking (MLE4 and Adaptive): – 2D model from SWH and altimeter wind-speed (standard version) – 3D model from SWH, altimeter wind-speed and t02 mean wave period from model (improved version)
Altimeter wind speed model	Table derived from Jason-1 GDR data, using GDR-D inputs	Following Gourrion's approach (Gourrion, 2020), based on Collard's model computed from Jason-1 (Collard, 2005)
Wind speed from model	ECMWF model	Identical to version "D"
Ionopheric correction	From Ku/C range difference	Two solutions for each retracking: • From Ku/C range difference correction • From Ku/C range difference filtered correction
Ionospheric model correction	Based on Global Ionophere TEC Maps from JPL	Identical to version "D"
Wet Troposphere Range Correction from Model	From ECMWF model.	From ECMWF model. 2 solutions : integration from sea surface level or using altimetry range
Dry Troposphere Range Correction	From ECMWF atmospheric pressures and model for S1 and S2 atmospheric tides.	From ECMWF atmospheric pressures and model for S1 and S2 atmospheric tides. 2 solutions : integration from sea surface level or using altimetry range
Inverse Barometer Correction	Computed from ECMWF atmospheric pressures after removing S1 and S2 atmospheric tides	Identical to version "D"
Non-tidal high-frequency dealiasing correction	Mog2D high resolution ocean model. Ocean model forced by ECMWF atmospheric pressures after removing S1 and S2 atmospheric tides	not available

Model	Product Version “D”	Product Version “F”
Dynamical Atmospheric Correction	not available	Mog2D high resolution ocean model + inverse barometer. Ocean model forced by ECMWF wind field and atmospheric pressures after removing S1 and S2 atmospheric tides
Tide solution 1	GOT4.8 + S1 ocean tide. S1 load tide ignored	GOT4.10c
Tide solution 2	FES2004 + S1 and M4 oceans tides. S1 and M4 load tide ignored	FES2014b (non-equilibrium long-period ocean tide model not included)
Internal tide model	not available	HRET_v8.1, Zaron (2019)
Equilibrium long-period ocean tide model	From Cartwright and Taylor tidal potential	Identical to GDR-D
Non-equilibrium long-period ocean tide model	Mm, Mf, Mtm and Msqm from FES2004	Mm, Mf, Mtm, Msqm, Sa and Ssa from FES2014b
Solid earth tide model	From Cartwright and Taylor tidal potential	Identical to version “D”
Pole tide model	Equilibrium model	From Desai (2015) and MPL (2017)
Mean Sea Surface	MSS_CNES-CLS11 (7 years reference) for repetitive phase and CNES-CLS15 for LRO and iLROs	2 solutions: MSS_CNES-CLS15 and MSS_DTU_2018
Mean Dynamic Topography	MDT_CNES-CLS09	MDT_CNES-CLS18
Geoid	EGM96	EGM2008
Bathymetry Model	DTM2000.1	ACE2 (from EAPRS Laboratory)
Rain flag	Derived from Jason-2 sigma naught MLE3 values	Derived from comparisons to threshold of the radiometer-derived integrated liquid water content and of the difference between the measured and the expected Ku-band backscatter coefficient , using an updated table of the difference between the measured and the expected Ku-band backscatter coefficient
Ice flag	Derived from comparison of the model wet tropospheric correction to a dual-frequency wet tropospheric correction retrieved from radiometer brightness temperatures, with a default value issued from climatology table	Identical to version “D”

Table 1: Models and standards adopted for Jason-2 product version “D” and “F”

2.3. Jason-3 GDR-F data used for comparison

Between Febuary 12 2016 to October 2 2016 (cycle 280 to 303 for Jason-2, cycle 0 to 23 for Jason-3), the tandem flight phase is specially suited for intercomparison between Jason-3 and Jason-2, as both satellite were only 80 seconds apart on the same ground track. In this current report, Jason-3 GDR-F standard was used to compare to Jason-2 reprocessed data. Jason-2 GDR-F and Jason-3 GDR-F use the same standard.

2.4. Jason-1 L2P data used for comparison

Between July 4 2008 to January 26 2009 (cycle 001 to 020 for Jason-2, cycle 240 to 260 for Jason-1), the tandem flight phase is specially suited for intercomparison between Jason-1 and Jason-2, as both satellite were only 55 seconds apart on the same ground track. In this current report, Jason-1 GDR-D standard from L2P DT21 is used to compare to Jason-2 reprocessed data. Model standard used in L2P is detailled in table 2 (information from [10]).

Model	Version
Orbit	POE-E
Range	MLE4
Sea state bias	Non parametric (N. Tran 2015)
Ionospheric correction	Filtered dual-frequency altimeter range measurement [22] (DORIS on Poseidon)
Wet tropospheric correction model	JMR (GDRE) radiometer
Dry tropospheric correction model	ERA5 (1-hour) model based
Dynamic atmospheric correction	TUGO High frequencies forced with analysed ERA5 pressure and wind field + inverse barometer Low frequences
Ocean tide height	FES2014b [25]
Internal tide	ZARON2019 (HRETv8.1 tidal frequencies: M2,K1,S2,O1) [25]
Pole tide	DESAI et al.2015 ; Mean Pole Location 2017 [23]
Solid earth tide	Elastic response to tidal potential [24]
Mean Sea Surface	Composite (SCRIPPS, CNES/CLS15, DTU15)

Table 2: Models and standards used for Jason-1 SLA L2P 2021

2.5. Jason-2 L2P data used for comparison

Jason-2 GDR-D standard from L2P is used to compare to Jason-2 reprocessed data as an intermediate version from Jason-2 GDR-D standard. Model standard used in L2P is detailled in table 2 (information from [10]) except for:

- orbit: POE-F
- SSB: Non parametric (N. Tran 2015)
- Ionospheric correction: Filtered dual-frequency altimeter range [22]
- Dynamic atmospheric correction: TUGO High frequencies forced with analysed ERA5 pressure and wind field. After 02/2016, MOG2D HF forced with analysed ECMWF pressure and wind-field + inverse barometer LF

3 Data coverage and validity of measurements

This part consists in analysing the availability of data for level 2 products before and after the reprocessing exercise. Futhermore the edited (invalidated) measurements are monitored.

3.1. Data availability

Each event of missing data is detailed on the previous annual and cyclic validation reports [2] and the main events are summarized in table 4.

Data availability is first analysed by comparing the number of available points. Another way to check the data coverage is to monitor the missing points. Missing data are detected using the time difference between 2 available points, with regard to a waiting for theoretical time difference of about 1 second. The two methods can lead to a slight difference in number of counted points.

Data coverage over ocean:
The data selection over ocean can be done thanks to the use of the surface_classification variable available in GDR. It is worth noting that this information evolved between GDR-D and GDR-F standards. It leads to a higher number of identified as ocean points for GDR-F than GDR-D. Note that the previous surface classification had 4 classes and new has 7 (see details in table 3 and figure 1). Both of them use 0 for ocean. However, there are more measurements flagged to 0 in new classiffication (GDR-F) than in previous (GDR-D), with near 500 additionnal ocean data per cycle in GDR-F. These additional measurements are mainly near coast and were flagged as land in GDR-D (see figure 2).

The reprocessed GDR-F data are globally as available as GDR-D (see upper row of figure 3). The cyclic number of available points at 1Hz can slightly change from GDR-D to GDR-F, with a difference lower than 6 points per cycle. This is mainly due to a difference in the method applied to pack and average the 20Hz elementary measurements in GDR-D ground segment version until mid-2017. To ease the comparison between GDR-D and GDR-F availability/missing rate over ocean, the new GDR surface_classification was applied on GDR-D data. This leads to slight difference in cyclic number of points but with a similar conclusion as on global point of view (see middle row of figure 3). Finally, missing points over ocean are monitored on bottom of figure 3, this highlights that differences are mainly for 1Hz measurements over land, which is coherent with the evolution of 20Hz elementary measurements packaging as source of differences between GDR-D and GDR-F.

GDR-F dataset coverage over ocean is equivalent to GDR-D's.

	Previous classification (GDR-D)	New classification (GDR-F)
0	ocean	open ocean
1	lake, enclosed sea	land
2	ice	continental water
3	land	aquatic vegetation
4	-	continental ice or snow
5	-	floating ice
6	-	salted basin

Table 3: Previous (GDR-D) and new (GDR-F) surface classification

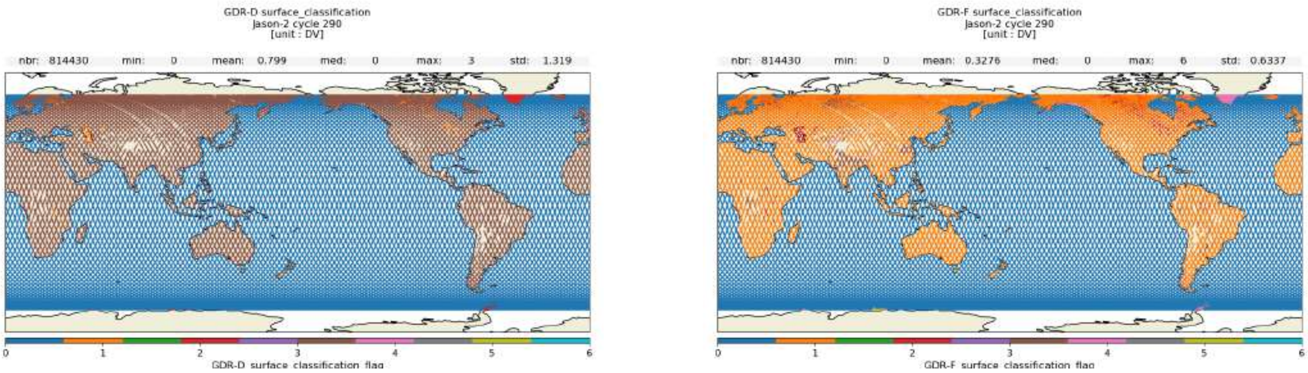

*Figure 1: Surface type / classification over one cycle in GDR-D (**left**) and GDR-F (**right**)*

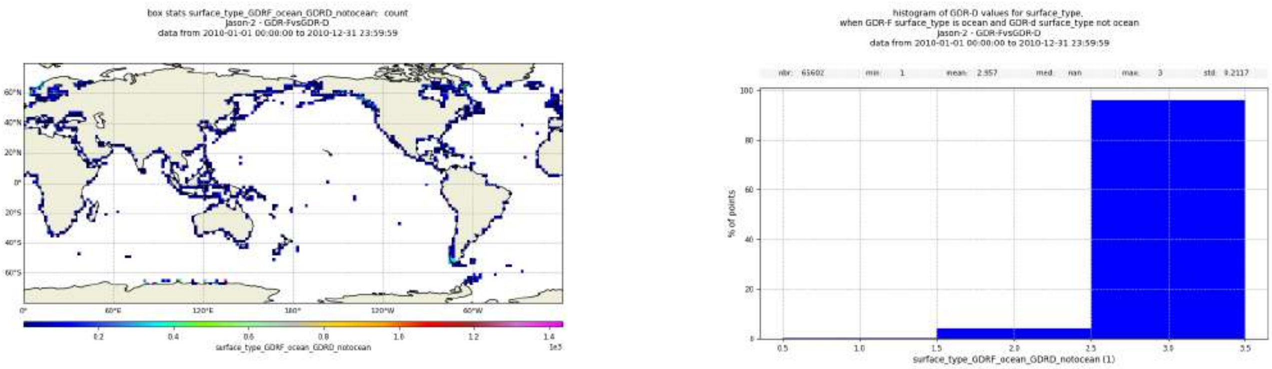

*Figure 2: Number of identified ocean point in GDR-F that are not ocean in GDR-D (**left**). GDR-D surface_type values for ocean additional GDR-F points (**right**)*

Table 4 gives the main data gaps during mission Jason-2 and the associated events. More details are available in [2].

Jason-2 cycle	Pass	Date	Event
Cycle 0	Passes 222 to 224	2008-07-10 from 18:28:03 to 20:26:03	Missing telemetry : Usingen station problem

Jason-2 cycle	Pass	Date	Event
Cycle 1	Passes 44 to 46 and 48 to 50	2008-07-13 from 17:39:59 to 19:37:30 and 2008-07-13 from 20:25:56 to 21:22:11	Missing telemetry : Usingen and NOAA stations problems
Cycle 33	Passes 204 to 213	2009-06-02 from 06:55:12 to 15:58:07	Software upload
Cycle 101	Passes 133 to 135	2011-04-04 from 18:49:07 to 21:03:49	Telemetry outage at Usingen
Cycle 174	Passes 43 to 161	From 2013-03-25 02:42:31 to 2013-03-29 17:52:47	Safe Hold Mode (SHM)
Cycle 174/175	Passes 191 (cycle 174) to 83 (cycle 175)	From 2013-03-30 21:57:48 to 2013-04-05 14:18:13	Safe Hold Mode (SHM)
Cycle 190/191	Passes 185 (cycle 190) to 116 (cycle 191)	From 2013-09-05 07:44:17 to 2013-09-12 12:25:52	Safe Hold Mode (SHM)
Cycle 285	Passes 217 to 241	From 2016-04-05 13:35:09 to 2016-04-06 12:02:41	Upload of new GPS On Board software
Cycle 304/305	Passes 1 (cycle 304) to 164 (cycle 305)	From 2016-10-02 11:53:32 to 2016-10-13 20:00:00	Move to interleaved ground track
Cycle 320/321	Passes 18 (cycle 321) to 137 (cycle 322)	From 2017-03-15 18:33:16 to 2017-03-30 08:47:31	Safe Hold Mode (SHM)
Cycle 327/500	Passes 111 (cycle 327) to 33 (cycle 500)	From 2017-05-17 22:08:10 to 2017-07-11 10:32:40	Move to LRO ground track
Cycle 506/509	Passes 178 (cycle 506) to 162 (cycle 509)	From 2017-09-14 06:12:04 to 2017-10-13 05:59:13	Safe Hold Mode (SHM)
Cycle 522/523	Passes 215 (cycle 522) to 215 (cycle 523)	From 2018-02-20 13:04:35 to 2018-03-02 09:56:11	Safe Hold Mode (SHM)
Cycle 537/600	Passes 211 (cycle 537) to 179 (cycle 600)	From 2018-07-18 07:44:41 to 2018-07-25 08:26:36	Move to iLRO ground track
Cycle 621/631	Passes 151 (cycle 621) to 56 (cycle 631)	From 2019-02-16 13:25:51 to 2019-05-22 11:27:54	Safe Hold Mode (SHM)

Table 4: Jason-2 level 2 missing passes from 2008 to 2019

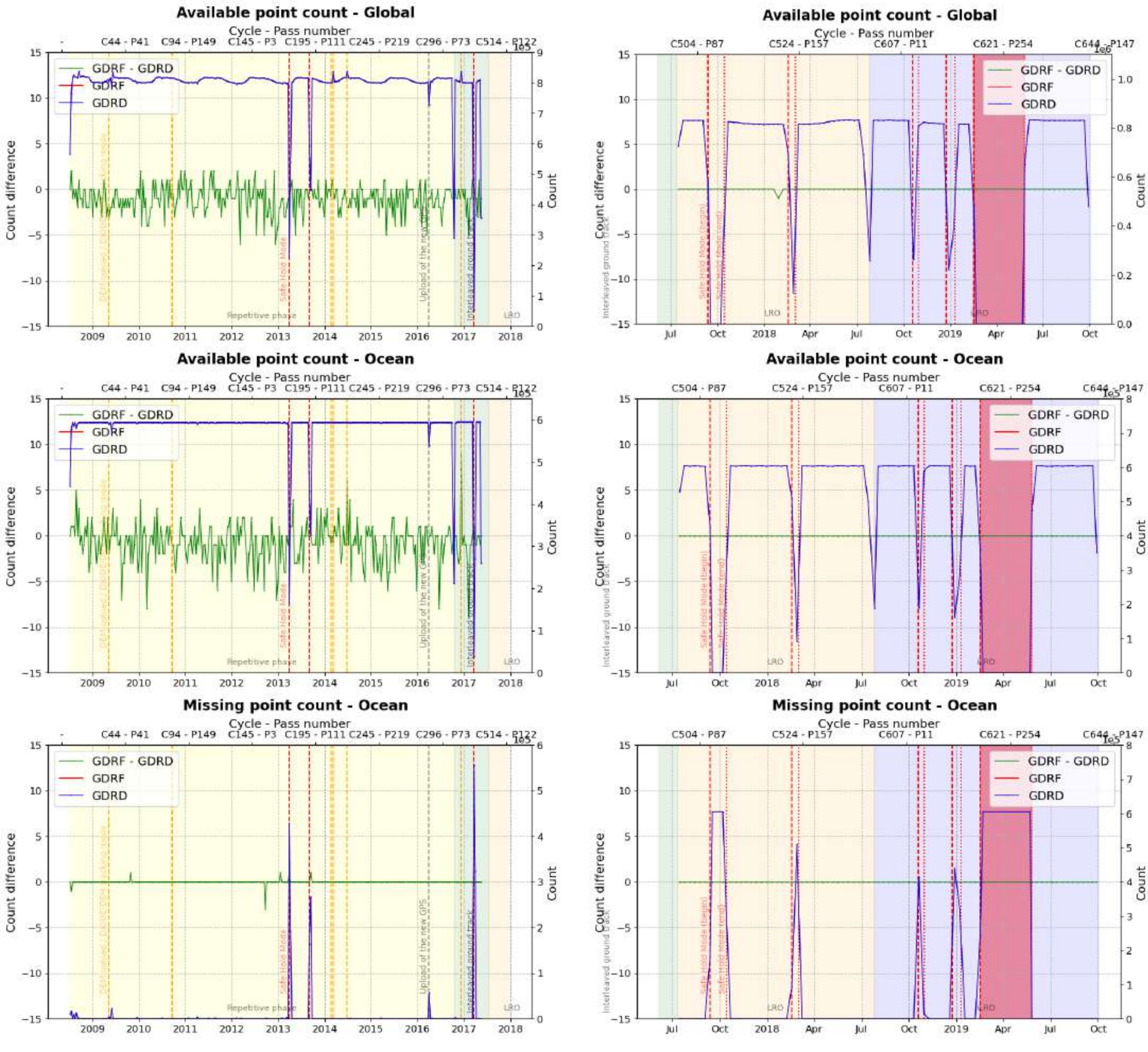

Figure 3: Number of available / missing data in 1 Hz products for GDR-F and GDR-D with difference during repetitive phase and interleaved ground track (**left**) and during LRO and iLRO phase (**right**)

3.2. Edited measurements

Data editing is necessary to remove altimeter measurements having lower accuracy. Once data over land are excluded, it consists in:

- First, removing the data corrupted by ice.
- Then, threshold criteria are applied on altimeter, radiometer and geophysical parameters as described in the following table 5. Except for the dual frequency ionosphere correction, only Ku-band measurements are used in this editing procedure, as they mainly represent the end user dataset.
- The third step uses cubic splines adjustement to the Sea Surface Height Anomaly (SSH-MSS) to detect remaining spurious measurements.
- The last step consists in removing an entire pass if SSH-MSS mean and standard deviation have higher values than thresholds. This criterion is used to detect problems such as bad orbit quality or time tag problems.

Data that are not removed by these four steps are declared valid data in the coming analysis.

Please note that as all rejected points rates by criterion are computed after the removal of land data, the differences in surface_classification between GDR-D and GDR-F impacts the compared statistics. In order to avoid the impact of this difference in the following results, the new GDR-F surface_classification has been applied on GDR-D dataset on this analysis.

3.2.1. Global overview

The percentage of valid data per cycle after editing process for GDR-F and GDR-D product is monitored on figure 4. The rate of rejected data is quite equivalent on GDR-D and GDR-F datasets (figure 4).

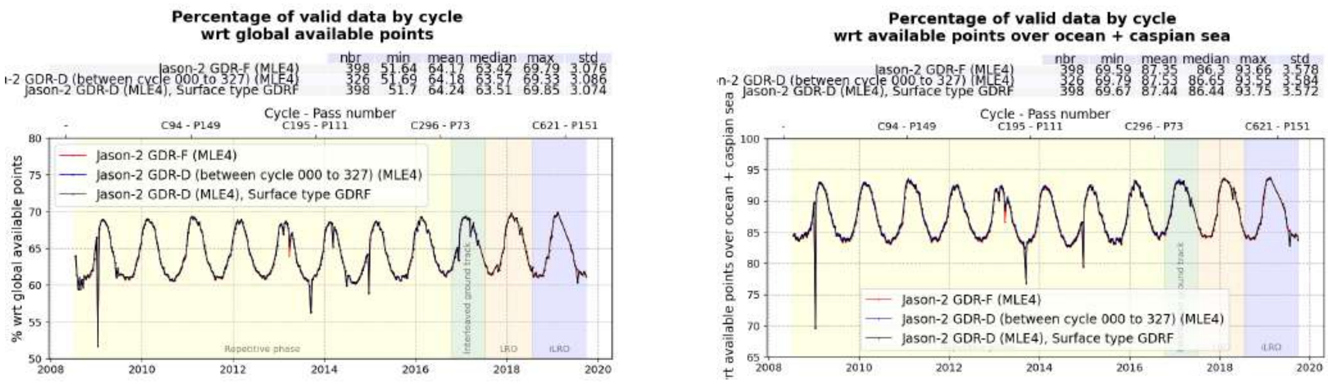

*Figure 4: Percentage of valid measurement for GDR-D and GDR-F with no surface type selection (**left**), and points selections over ocean (**right**).*

The main events leading to an incease of rejected points (for both datasets) are :

- cycle 019 due to radiometer wet tropospheric correction set to defaut value during an AMR anomaly between passes 24 to 42 and 119 to 161 [9],
- cycle 191 (passes 116 to 125), again due to AMR anomaly after SHM [8],
- cycle 238 (passes 20 to 43), during another AMR anomaly [6] ,

Except for these cycles, valid data represent 60 to 70 % of global available data, depending on seasonal ice coverage, for both GDR-F and GDR-D. Over ocean, valid data rate is between 83 and 94 %.

Except to noticeable events (cycle 174 , loss of 1.3% points in GDR-F compared to GDR-D round SHM event, and cycle 637 gain of 1.7% of points in GDR-F), GDR-F rate of valid points is slithly lower (0,1%) than GDR-D (figure 4 and figure 5)

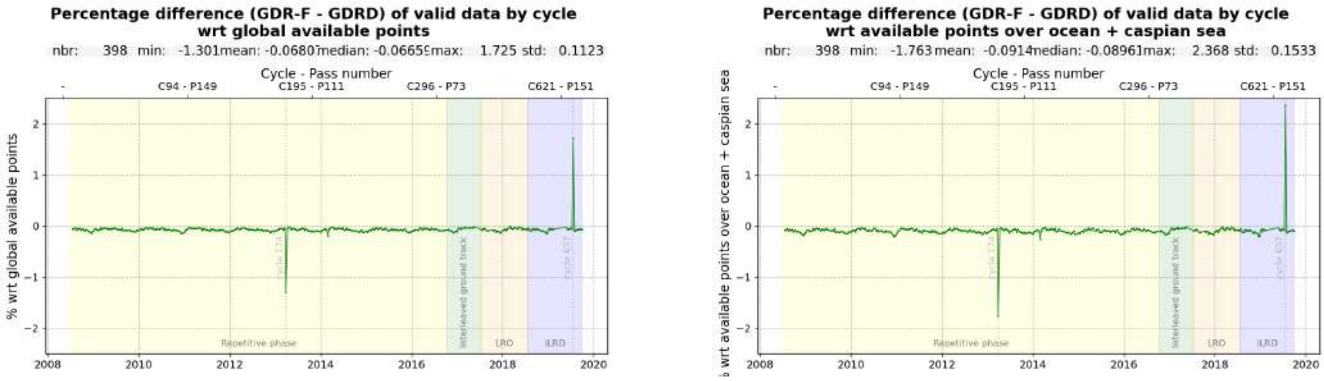

*Figure 5: Percentage of valid measurement differences (GDR-F minus GDR-D) with no surface type selection (**left**), and points selections over ocean (**right**).*

The discrepancies are also visible on the spatial distribution of the valid data (figure 7). Globally, measurements are more valid over open ocean on GDR-F dataset than in GDR-D dataset (red boxes on left of figure 6), but there are more rejected data in GDR-F mainly near ice and coasts (blue boxes on figure 6).

Note that GDR-D SSH was computed thanks to a non filtered ionospheric correction, whereas GDR-F SSH ionospheric correction solution is a filtered one. GDR-F rejected data near coast and ice are then mainly due to the ionospheric correction filtering behavior near coasts and ice (the same effect was described during Jason-3 GDR-F reprocessing assessment, see part 3.2.4 in [11]).
In addition, the valid points for GDR-D / invalid points for GDR-F monitoring (blue curve on top of figure 7) is more sensitive to seasonal ice coverage than the valid points for GDR-F / invalid points for GDR-D (red curve). This is due to the annual evolution of ionospheric filtering (loss of points near ice).

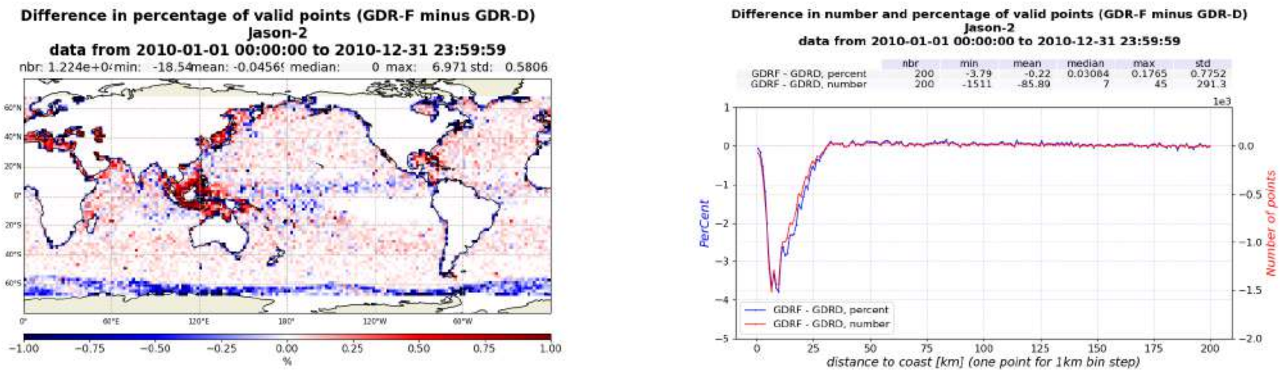

*Figure 6: Map of the number of valid points difference in percentage (**left**). Blue boxes indicate that there are more valid measurements in GDR-D. Red boxes indicate that there are more valid measurements in GDR-F. Monitoring in function of distance to coast (**right**). Both figures are computed over one year of data.*

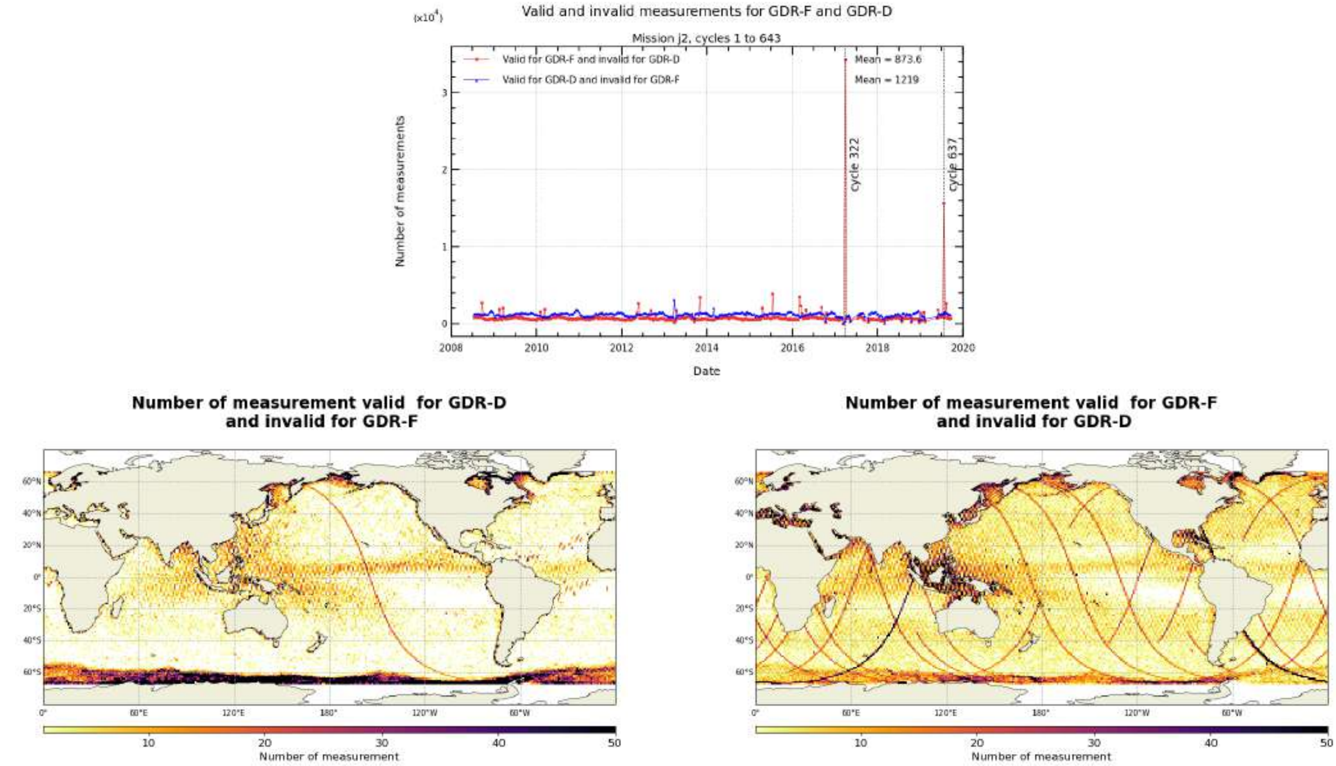

*Figure 7: Cyclic number of measurements that are valid in one case and not in the other between cycle 1 and 644 (**top**). Map of valid GDR-D / invalid GDR-F points (**left**) and map of valid GDR-F / invalid GDR-D points (**right**). All the other records have the same valid/invalid status on both GDR-D and GDR-F datasets.*

3.2.2. Rejection on land and ice detection

The first step of editing process includes the removal of points over land (thanks to surface_classification_flag variable), and ice detection (thanks to ice_flag variable). As a reminder, in this analysis, surface classification differences - described in table 3 and figure 1 - impact is known : an homogeneous to GDR-F classification ocean selection is used for both datasets. When considering GDR-F surface_classification_flag set to "open ocean" (value 0 both in GDR-D and GDR-F products), there are more points with altimeter ice flag activated for GDR-F data than GDR-D data (see figure 8).

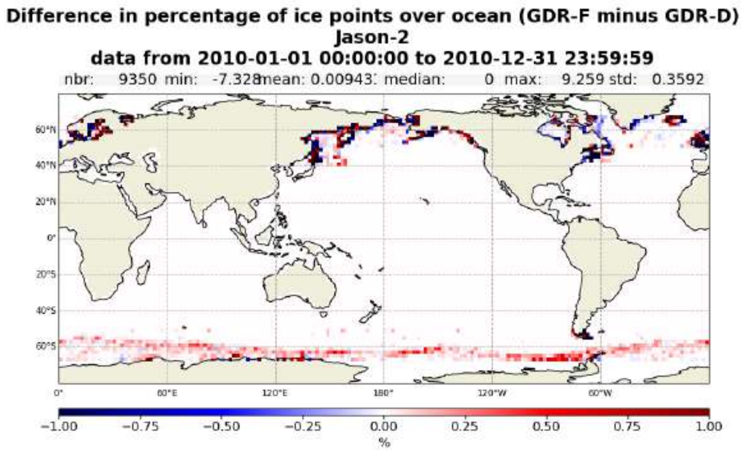

Figure 8: Percentage difference on ice flaggeg points (computed over one year of data). Blue boxes indicate that there are more ice flagged measurements in GDR-D. Red boxes indicate that there are more ice flagged measurements in GDR-F.

3.2.3. Rejection on thresholds criteria

Editing on thresholds criteria is done after remove of land and ice points, so that the change in surface_type / surface_classification described in part 3.1. has an impact on the rate of measurements rejected at this step.

The evolution of rejected on thresholds number of points is computed on GDR-D data, using the updated to GDR-F version of surface_classification is detailled in table 4 in [11]. As explained during Jason-3 reprocessing from GDR-D to GDR-F analysis ([11] part 3.2.4), considering the same ocean surface definition, significant differences in rejected on thresholds rate are only visible on ionospheric correction and sea level anomaly criteria. In both cases these differences are linked to the filtering solution of ionospheric correction : there are slightly less rejected points on ionospheric correction over open ocean, but more rejected points on SLA thresholds due to set to Default Value points near coasts and ice. At a second order, differences can be seen on FES ocean tide and sea state bias. Finally 3.38% points are rejected in GDR-F against 3.28% in GDR-D.
Note that users interested in coastal studies can recompute their own ssha values using the non filtered iono_cor_alt variable that is still available in products.

Parameter	Threshold: min	Threshold: max	GDR-D MLE4 (GDR-F surface class type)	GDR-F MLE4 (GDR-F surface class type)
swh	0	11 m	0.71 %	0.71 % ↔
square off nadir angle	-0.2 deg^2	0.64 deg^2	0.65 %	0.65 % ↔
sea surface height (orbit - range)	-130 m	100 m	0.84 %	0.84 % ↔
range : number of 20 Hz meas.	10	20	1.11 %	1.11 % ↔
range : std of 20 Hz meas.	0 m	0.2 m	1.47 %	1.47 % ↔
sigma0	7 dB	30 dB	0.64 %	0.63 % ↔
.../...				

Parameter	Threshold: min	Threshold: max	GDR-D MLE4 (GDR-F surface class type)	GDR-F MLE4 (GDR-F surface class type)
sigma0 : number of 20 Hz meas. sigma0 : std of 20 Hz meas.	10 0	20 1 dB	1.10 % 2.00 %	1.10 % ↔ 1.99 % ↔
wind speed from altimeter	0	30 m/s	1.08 %	1.07 % ↔
sea state bias	-0.5 m	0	0.68 %	0.59 % ↘
ionospheric correction (filtered) ionospheric correction (raw data)	-0.4 m -0.4 m	0.4 m 0.4 m	- 1.11 %	0.95 % ↘ (compared to raw iono) 1.10 % ↔
radiom. wet tropospheric corr.	-0.5 m	-0.001 m	0.22 %	0.22 % ↔
sea level anomaly sea level anomaly (iono raw)	-2 m -2 m	+2 m +2 m	- 1.09 %	1.59 % ↗ (compared to raw iono) 1.07 % ↔
ocean tide (FES) ocean tide (GOT)	-5 m -5 m	5 m 5 m	0.20 % 0.01 %	<0.01 % ↘ <0.01 % ↔
cyclic mean number of edited points by thresholds - GDR-D: non filtered iono. - GDR-F: filtered iono.			17428	17642
percentage of rejected points by thresholds wrt non ice (ocean + caspian sea)			3.28 %	3.38 % ↗

Table 5: Thresholds editing rates from 2008 to 2019 (cycles 001 to 644)

4 Quality overview and performances

In this chapter the performances of Jason-2 GDR-F data are analyzed at crossovers and along-track.

4.1. Sea Surface Height at crossover points

Ascending and descending SSH (Sea Surface Height) differences are computed at crossover points. These differences are done for time differences less than 10 days between points from ascending and descending tracks. This allows to minimize the contribution of the oceanic variability on mesoscale. Therefore the variance of the SSH differences at crossover points gives an information of the altimeter system performance.

4.1.1. Performance at crossover between GDR-F and GDR-D

The SSH calculation for Jason-2 are defined below :

$$SSH_{GDR-D} = Orbit_{GDR-D} - AltimeterRange_{GDR-D} - \sum_{i=1}^{n} Correction_{GDR-D_i} \quad (1)$$

with $Orbit_{GDR-D}$ = POE-D until cycle 253 and POE-E from cycle 254 onwards.

$$SSH_{GDR-F} = Orbit_{GDR-F} - AltimeterRange_{GDR-F} - \sum_{i=1}^{n} Correction_{GDR-F_i} \quad (2)$$

	$\sum_{i=1}^{n} Correction_{GDR-D_i}$ equal to the sum of	$\sum_{i=1}^{n} Correction_{GDR-F_i}$ equal to the sum of
Non parametric sea state bias corr.	from GDR-D	from GDR-F (2D)
Dual frequency ionospheric corr.	from GDR-D (non filtered)	from GDR-F (filtered)
Radiometer wet tropospheric corr.	from GDR-D	from GDR-F
Dry tropospheric corr.	operational ECMWF	identical to GDR-D
Dynamical atmospheric corr.	operational MOG2D	identical to GDR-D
Ocean tide corr.	GOT4.8 (including loading tide)	FES14B (including loading tide and dynamical waves)
Internal tide corr.	N/A	HRET8.1 (ZARON2019), 4 waves included
Earth tide height	Cartwright and Taylor	identical to GDR-D
Pole tide height	Wahr85 (constant mean pole location)	Desai2015 / MPL2017

Table 6: GDR-D versus GDR-F SSH components for performances at crossover points analysis

In order to monitor the performances over stable surfaces, additional editing is applied to remove shallow waters (bathymetry above -1000 m), areas of high ocean variability (variability above 20 cm rms) and high

latitudes ($> |50|$deg). SSH performances are then always estimated with equivalent conditions.
Geographical patterns of mean SSH differences at crossovers, averaged over the whole period, are significantly reduced (see bottom of figure 9) : this was already noticed in [5] thanks to POE-D to POE-E orbit version evolution. This is linked to the way the solar radiation pressure has been differently modelised in POE-D and from POE-E onwards.
The cyclic mean of SSH differences at crossover points shows a more than doubled 120 days signal, and a significantly reduced near 90 days signal (top of figure 9) from GDR-D to GDR-F. It has been shown in [4] and [12] that the choice of ocean tide solution used to compute ssh impacts the amplitude of the observed signals. In particular, using the couple POE-D + GOT4.8 led to a visible 120days signal on Jason-2, whereas the couple POE-E + GOT4.8 led to no visible 120days signal. Finally, the couple POE-E + FES14 led again to a visible 120days signal, and so POE-F + FES14. The way these solutions are correlated together is not completely known and will be further investigated.
Note that in GDR-F, the reference SSHA uses the FES model instead of GOT in GDR-D. So that comparing GDR-F to GDR-D solution leads to compare POE-F/FES14 to POE-D_POE-E/GOT4.8.

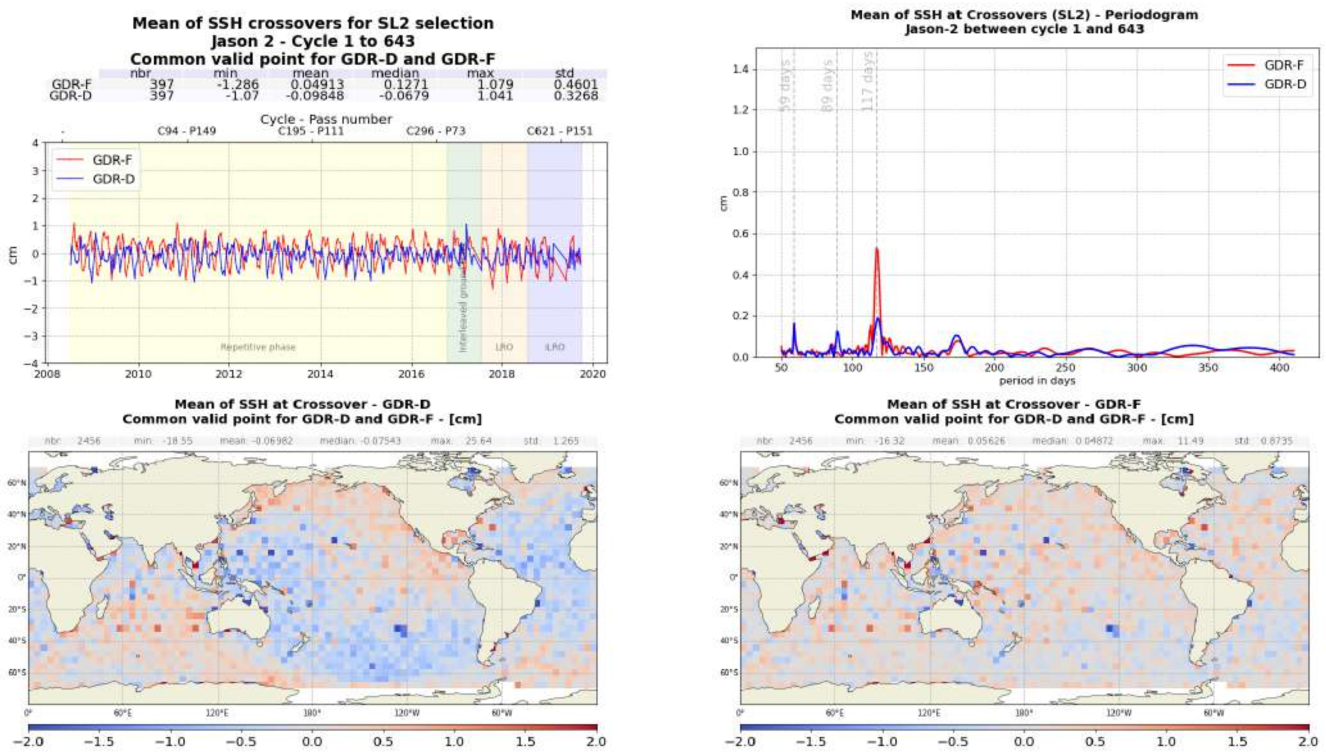

*Figure 9: Cyclic mean of SSH differences at crossovers for GDR-F and GDR-D (selection on $|latitude| <$ 50, oceanic variability $<$ 20 cm and bathymetry $<$ -1000 m) (**top**). Mean of SSH differences at crossovers map average over the whole period for GDR-D (**bottom left**) and GDR-F (**bottom right**)*

The global variance reduction from GDR-D to GDR-F, is -5.74 cm^2 (figure 10). The error estimated from standard deviation of SSH differences at crossovers (error = standard deviation divided by $\sqrt{2}$) confirms this gain for GDR-F compared to GDR-D, Jason-2 GDR-F error is similar to Jason-3 GDR-F error (top left of figure 10).

The main contributor to this variance reduction of SSH differences between ascending and descending passes is the filtering version of the ionospheric correction (see figure 14 in [11]). It is reduced everywhere between 5 and 25% (blue boxes on right part of figure 10).

Finally, the different contributors involved in this improvement of -5.74 cm^2 at monomissions crossover points are detailed in figure 11.

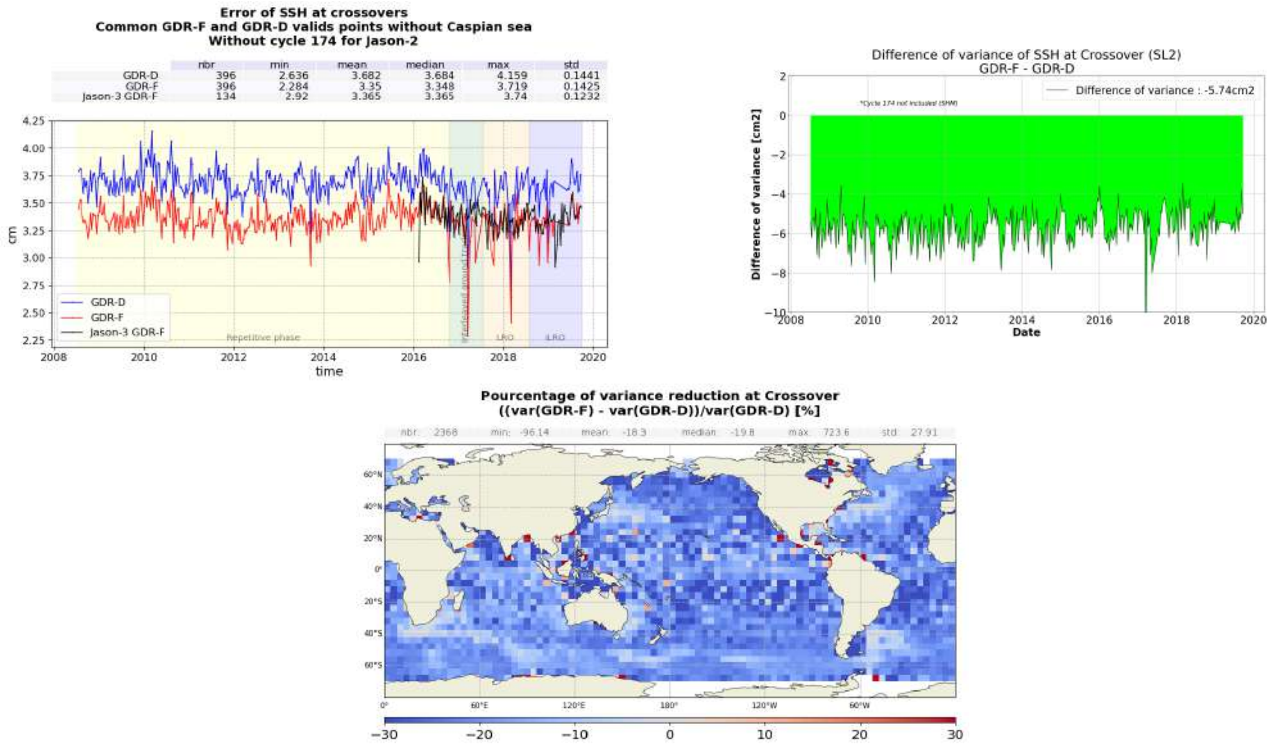

*Figure 10: Top : Cyclic statistics of SSH differences at crossovers with selection on $|latitude| < 50$, oceanic variability $<$ 20 cm and bathymetry $<$ -1000 m. **Top left** : error per cycle for GDR-F, GDR-D et Jason-3 GDR-F. **Top right** : difference (GDR-F - GDR-D) of variance.**Bottom** : map of difference (GDR-F - GDR-D) of variance in percentage*

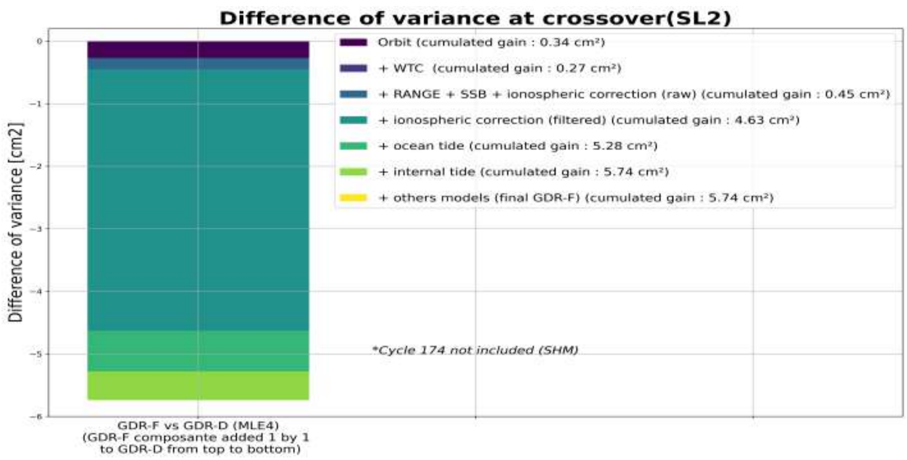

Figure 11: Impact on variance at monomissions crossover points for each contributor between GDR-D and GDR-F

4.1.2. Estimation of the pseudo datation bias

The pseudo time tag bias is found by computing at SSH crossovers a regression between SSH and orbital altitude rate ($\dot{H}$), also called satellite radial speed :

$$SSH = \alpha \dot{H} \tag{3}$$

This method allows us to estimate the time tag bias but it absorbs also other errors correlated with $\dot{H}$ as for instance orbit errors. Therefore it is called "pseudo" time tag bias. The monitoring of this coefficient estimated at each cycle is performed for Jason-3 and Jason-2 and shown on figure 12: it highlights that pseudo time tag bias is close to zero (mean value lower than 0.04 ms) for both missions. There is no significant impact of reprocessing on pseudo datation bias estimation.

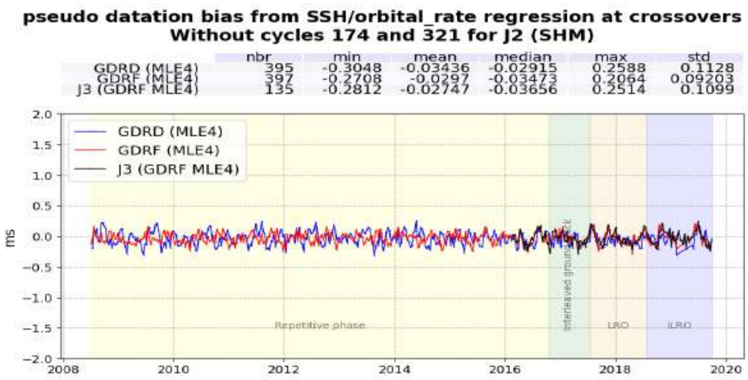

Figure 12: Cyclic monitoring of pseudo time tag bias for Jason-3 and Jason-2

4.2. Along-track performance of Sea Level Anomaly

The Sea Level Anomaly corresponds to the Sea Surface Height where the Mean Sea Surface is removed (SLA = SSH - MSS). In the frame of this analysis, only CNES/CLS15 mean sea surface solution has been used for GDR-F dataset, whereas a mix of CNES/CLS11 (before cycle 327 = repetitive+interleaved track) and CNES/CLS15 (for cycle 500 onwards = LRO+iLRO track) is used for GDR-D dataset. Note that this MSS change leads to a step of 2.4cm in the GDR-D dataset occuring in 07/2017. Along track sea level anomaly standard deviation is reduced by 0.8 cm with GDR-F compared to GDR-D (figure 13). The variance of the SLA is lower for GDR-F than GDR-D: -14.6 cm^2 with GDR-F, caspian sea included (see figure 13).

Computing the standard deviation of Sea Level Anomaly for each major oceanic basin (see figure 14) allows to highlight the ENSO event at end of 2015 / beginning 2016. The elevation of this indicator over global ocean is clearly visible only on pacific (= green) curve on bottom figures. Out of this event period, GDR-F sla standard deviation is lower for GDR-F than for GDR-D at global point of view (top figure 13). It is mainly due to the drop in pacific ocean, probably linked to a closer to Jason-2 averaging period for mean sea surface, including now data from 1993 to 2012 instead of 1993 to 1999 for GDR-D repetitive phase.

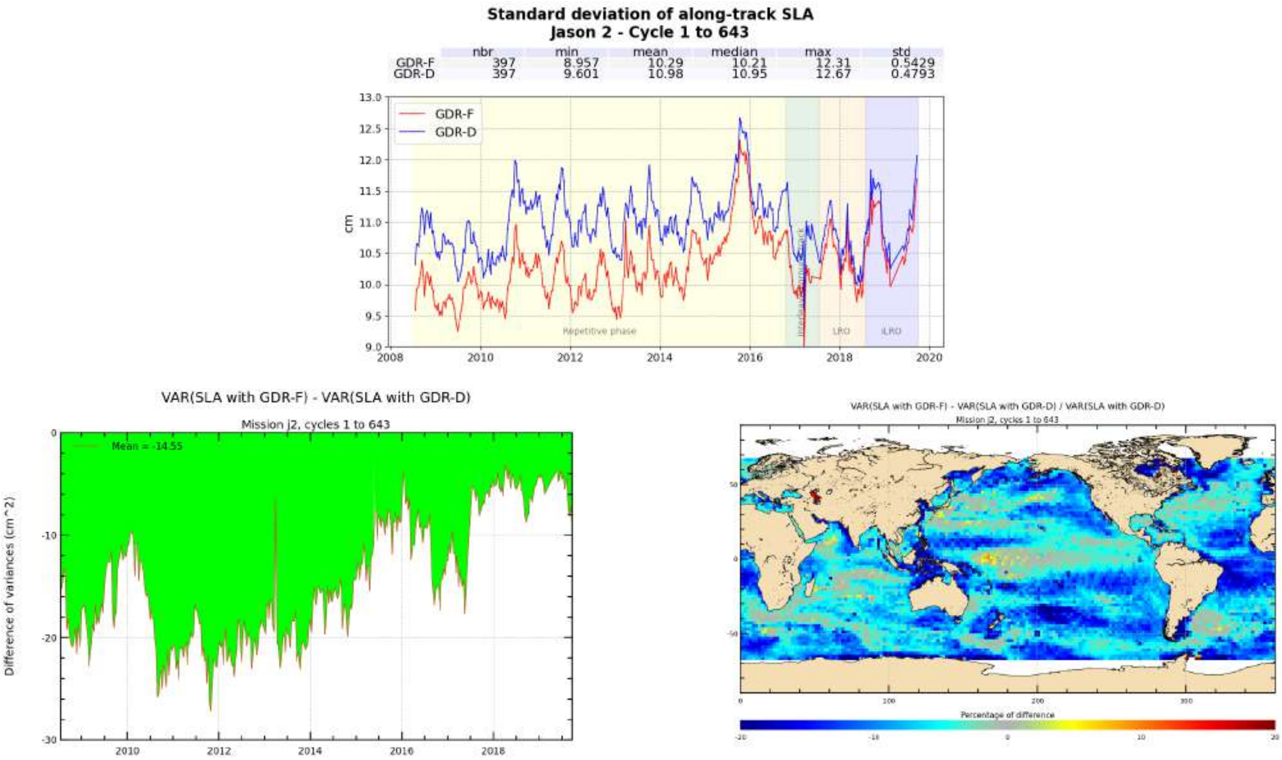

*Figure 13: Standard deviation of sea level anomaly (over ocean + Caspian Sea) (**top**), SLA variance difference between GDR-F and GDR-D (**bottom left**) and Map of SLA variance difference between GDR-F and GDR-D with regard to GDR-D level of variance (**bottom right**)*

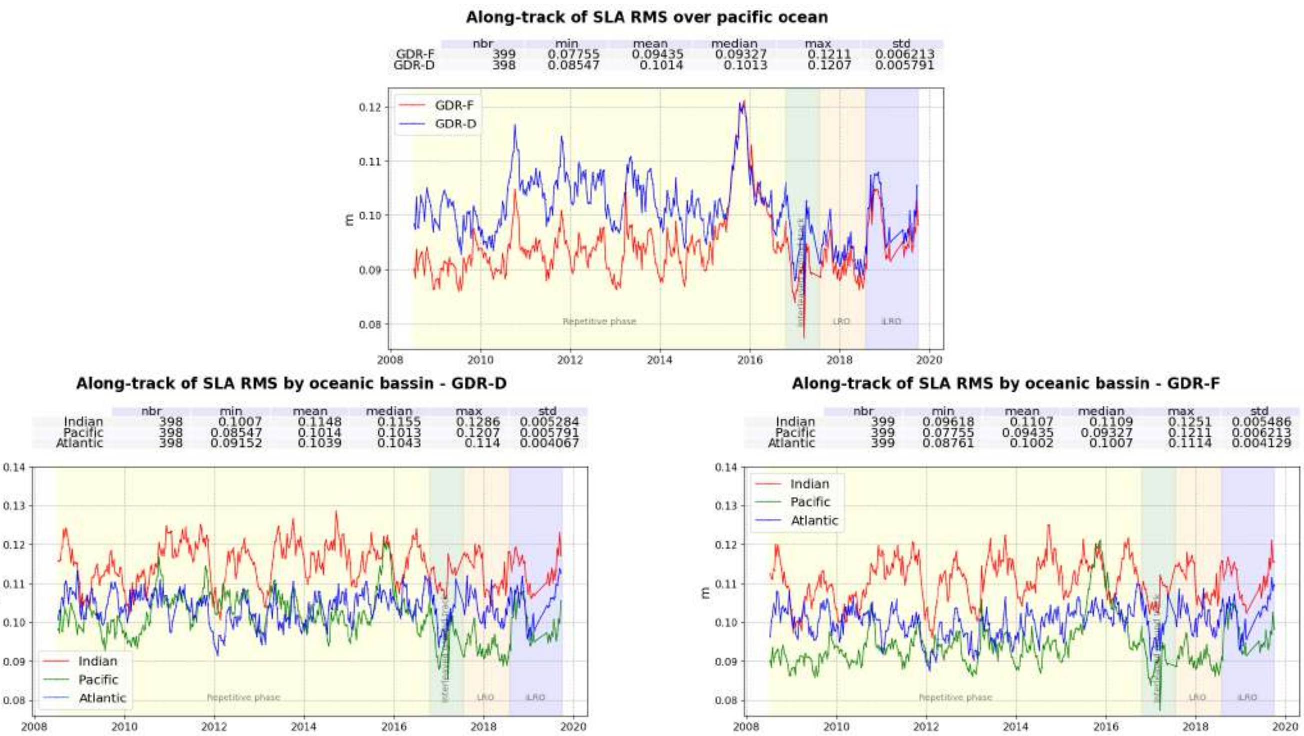

*Figure 14: Standard deviation of sea level anomaly over Pacific ocean for GDR-D and GDR-F (**top**). Standard deviation of sea level anomaly over Pacific ocean, atlantic ocean and indian ocean for GDR-D (**bottom left**) and for GDR-F (**bottom right**)*

5 Details of the changes in GDR-F standard

In this chapter we aim to detail the changes of the GDR-F standard compared to GDR-D and there impact.

The following points are adressed:

- the datation
- the orbit standard
- the radiometer related parameters
- the altimeter related parameters
- the other corrections.

5.1. Datation difference

Datation can be different between GDR-F and GDR-D. This is due to slight differences in the 20hz measurements that are taken into account to compute each 1hz point.
Figure 15 shows the number of measurements where the difference is higher than 1μs. The global number of point per cycle with datation difference higher than 1μs is mostly between 500 and 2500 points but can reach higher level for some cycles, especially between cycle 130 and cycle 175. In particular, difference in datation for cycles 155, 290, 514 and 635 are shown on figure 16. This highlights that this could concern some isolated points but also sometimes quite longer part of passes. As mentioned in part 3.1., this differences in processing software are known for data until mid-2017, so that on figure 15 differences are clearly lower over the LRO and iLRO periods (from mid 2017 onwards).

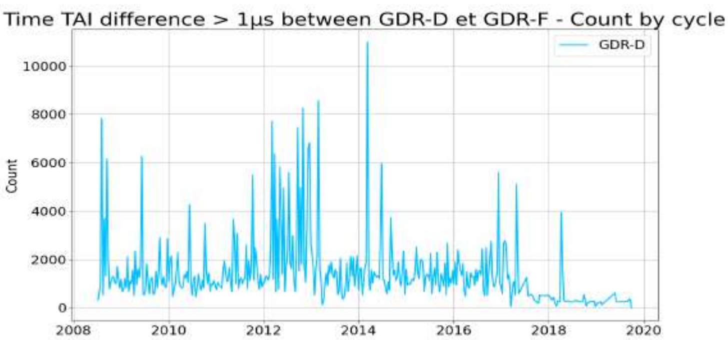

Figure 15: Cyclic count of measurements with time difference between GDR-F and GDR-D $> 1\mu s$

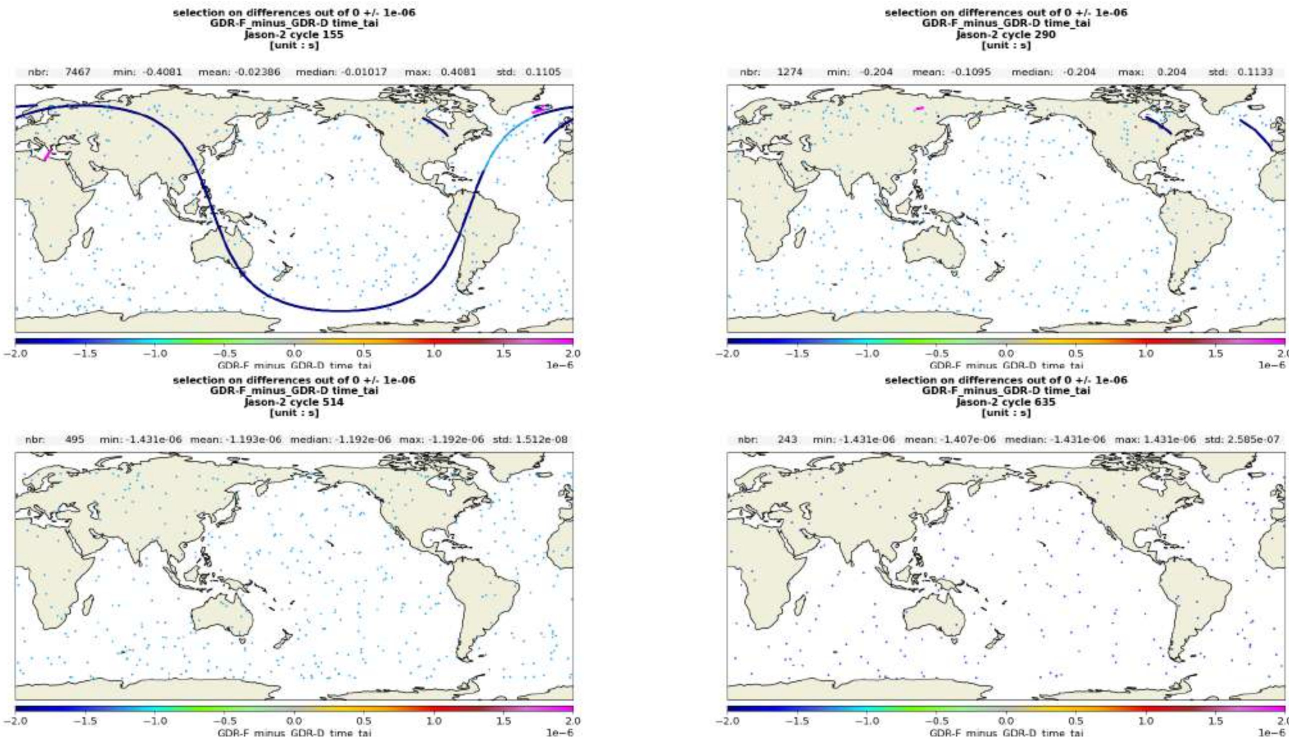

Figure 16: Points with difference in datation between GDR-D and GDR-F for cycle 155, 290, 514 and 635

5.2. GDR-F Precise Orbit Ephemeris POE-F

GDR-D orbit solution is the CNES Precise Orbit Ephemeris standard D (POE-D) until cycle 254 and standard E (POE-E) from cycle 254 onwards. GDR-F orbit solution is POE-F. Differences between POE-F and previous versions POE-E and POE-D are summarized below.

Parameter	POE-D	POE-E	POE-F
Gravity model	• EIGEN-GRGS_RL02bis_MEAN-FIELD (2011) • Non-tidal TVG : **Annual, Semi-annual, and drifts up to deg/ord 50** • Solid Earth tides : IERS2003 conventions • Ocean tides : **FES2004** • Oceanic/atmospheric gravity : **6hr NCEP pressure fields + tides from Biancale-Bode model** • Pole tide : solid earth and ocean from IERS2010 conventions • Thirds bodies : Sun, Moon, Venus, Mars and Jupiter	• EIGEN-GRGS.RL03-v2.MEAN-FIELD • Non-tidal TVG : one annual, one semi-annual, one bias and one drift terms for each year up to **deg/ord 80**; C21/S21 modeled according to IERS2010 conventions • Solid Earth tides : IERS2003 conventions • Ocean tides : **FES2012** • Oceanic/atmospheric gravity : **6hr NCEP pressure fields (70x70) + tides from IERS2010 conventions** • Pole tide : solid earth and ocean from IERS2010 conventions • Thirds bodies : Sun, Moon, Venus, Mars and Jupiter	• EIGEN-GRGS.RL04-v1.MEAN-FIELD • Non-tidal TVG : one annual, one semi-annual, one bias and one drift terms for each year up to **deg/ord 90**; C21/S21 modeled according to IERS2010 conventions • Solid Earth tides : Unchanged • Ocean tides : **FES2014** • Oceanic/atmospheric gravity : **3hr dealiasing products from GFZ AOD1B RL06** • Pole tide : Unchanged • Thirds bodies : Unchanged
Surface forces	• Radiation pressure model : calibrated semi-empirical solar radiation pressure model • Earth radiation : Knocke-Ries albedo and IR satellite model • Atmospheric density model : **DTM-94 for Jason satellites. MSIS-86 for other satellites**	• Radiation pressure model : Unchanged • Earth radiation : Unchanged • Atmospheric density model : **DTM-13 for Jason satellites and HY-2A. MSIS-86 for other satellites**	• Radiation pressure model : Unchanged • Earth radiation : Unchanged • Atmospheric density model : **DTM-13 for Jason satellites and HY-2A. MSIS-00 for other satellites**
Estimates dynamical parameters	**Drag coefficient every 2 or 3 revolutions. Along-track and Cross-track 1/rev per day or every 12 hours**	**Stochastic solutions**	Unchanged

Parameter	POE-D	POE-E	POE-F
Satellite reference	• Mass and center of gravity : post-launch values + variations generated by Control Center • Attitude model : **For jason satellites, quaternions and solar panel orientation from control center, completed by nominal yaw steering law when necessary. Other satellites nominal attitude law**	• Mass and center of gravity : Unchanged • Attitude model : Unchanged	• Mass and center of gravity : Unchanged • Attitude model : **Refined nominal attitude laws**
Displacement of reference points	• Earth tides : IERS2003 conventions • Ocean loading : **FES2004** • Pole tide : solid earth pole tides • Reference GPS constellation : **JPL solution - fully consistent with IGS08**	• Earth tides : IERS2003 conventions • Ocean loading : **FES2012** • Pole tide : solid earth pole tides **and ocean pole tides (DESAI, 2002), cubic+linear mean pole model from IERS2010** • S1-S2 atmospheric pressure loading: **implementation of Ray and Ponte (2003) by Van Dam** • Reference GPS constellation : Unchanged	• Earth tides : Unchanged • Ocean loading : **FES2014** • Pole tide : solid earth pole tides **and ocean pole tides (DESAI, 2002), new linear mean pole model** • S1-S2 atmospheric pressure loading : Unchanged • Reference GPS constellation : **GRG solution - fully consistent with IGS14**
Geocenter variations	-	• Tidal: Ocean loading and S1-S2 atmospheric pressure loading • Non-tidal: **Seasonal model from J.ies applied to DORIS/SLR stations**	• Tidal: Unchanged • Non-tidal: **Full non-tidal model (semi-annual, annual and inter-annual) derived from DORIS data and the OSTM/Jason-2 satellite, applied to DORIS/SLR stations and GPS satellites**

Parameter	POE-D	POE-E	POE-F
Terrestrial Refrence Frame	**Extended ITRF2008 (SLR-F/ITRF2008, DPOD2008, IGS08)**	Unchanged	**Extended ITRF2014 (SLR-F/ITRF2014, DPOD2014, IGS14)**
Earth orientation	Consistent with IERS2010 conventions and **ITRF2008**	Unchanged	Consistent with IERS2010 conventions and **ITRF2014**
Propagation delays	• SLR troposphere correction : Mendes-Pavlis • SLR range correction : **Constant 5.0cm range correction for Envisat, elevation dependent range correction for Jason** • DORIS troposphere correction : **GPT/GMF model** • GPS PCO/PCV (emitter and receiver) consistent with constellation orbits and clocks **(IGS08 ANTEX)** • GPS phase wind-up correction	• SLR troposphere correction : Unchanged • SLR range correction : Unchanged • DORIS troposphere correction : Unchanged • DORIS beacons phase center correction • GPS PCO/PCV (emitter and receiver) consistent with constellation orbits and clocks **(IGS08 ANTEX), prelaunch GPS receiver phase map** • GPS phase wind-up correction : Unchanged	• SLR troposphere correction : Unchanged • SLR range correction : **Geometrical models for all satellites** • DORIS troposphere correction : **GPT2/VMF1 model** • Unchanged • GPS PCO/PCV (emitter and receiver) consistent with constellation orbits and clocks **(IGS14 ANTEX), in flight adjusted GPS receiver phase map** • GPS phase wind-up correction : Unchanged
Estimated measurement parameters	• DORIS : one frequency bias per pass, one troposphere zenith bias per pass • SLR : Bias per arc solved for a few stations, bias per pass for a few stations • GPS : **Floating ambiguity** per pass, receiver clock adjusted per epoch	• DORIS : Unchanged • SLR : Reference used to evaluate orbit precision and stability • GPS : Unchanged	• DORIS : one frequency bias per pass **and drift (for "SAA stations")** per pass, one troposphere zenith bias per pass, **horizontal tropospheric gradients per arc** • SLR : Unchanged • GPS : **fixed ambiguity (when possible)** per pass, receiver clock adjusted per epoch

Parameter	POE-D	POE-E	POE-F
Tracking Data corrections	Jason-1 DORIS data : South Atlantic Anomaly model (J.-M. Lemoine et al.) applied before and after DORIS instrument change. DORIS datation bias for Envisat and Jason aligned with SLR before and after instrument change	Jason-1 DORIS data : **Updated** South Atlantic Anomaly model (J.-M. Lemoine et al.) applied before and after DORIS instrument change. Doris Time-tagging bias for Envisat and Jason aligned with SLR before and after intrument change.	Unchanged
DORIS weight	**1.5 mm/s (1.5cm over 10sec)**	Unchanged	**Process data down to as low elevation angles as possibles (from 10° to 5° elevation cut-off angle) with a consistent down-weightling law**
SLR weight	**10cm**	**15cm. Reference used to evaluate orbit precision and stability**	Unchanged
GPS weight	**10cm (phase) / 10m (code)**	**2cm (phase) / 2m (code)**	Unchanged

Table 7: POE-D, POE-E and POE-F orbit standard

Cyclic mean of the differences between orbits solutions (POE-D vs POE-F, then /POE-E vs POE-F) is stable in time for each period, with a small 1mm bias at cycle 254 when orbit solution changed in GDR-D. Variations under +/- 2mm (see top left of figure 17) are visible, mainly over the POE-D period of GDR-D (before cycle 254). As POE-F is closer to POE-E than to POE-D, the standard deviation of the difference is slightly lower after the orbit solution change for GDR-D (POE-D to POE-E) (top right of figure 17).

The maps of the differences between the two orbit solutions (bottom figure 17), computed between cycle 001 to 643 shows no significant global bias (<1mm in average), this is coherent with top left of figure 17. Geographically correlated patterns can reach +/-0.4 cm, but are not stable in time, particularly due to the inhomogeneous solution used in GDR-D dataset. Note that details on POE-D to POE-E differences are available on [6].

Variance of SSH differences at crossovers are compared using different solutions as a key performance indicator (figure 18). In our case, a global reduction of 0.27 cm^2 using POE-F SSH computation compared to SSH POE-E indicates an improvement. This is particularly visible on the beggining of the period when GDR-D orbit solution was POE-D (blue boxes, except over Indonesia on left of figure 18). Differences between sla variance levels are not significant after cycle 254 (POE-E in GDR-D, right of figure 18).

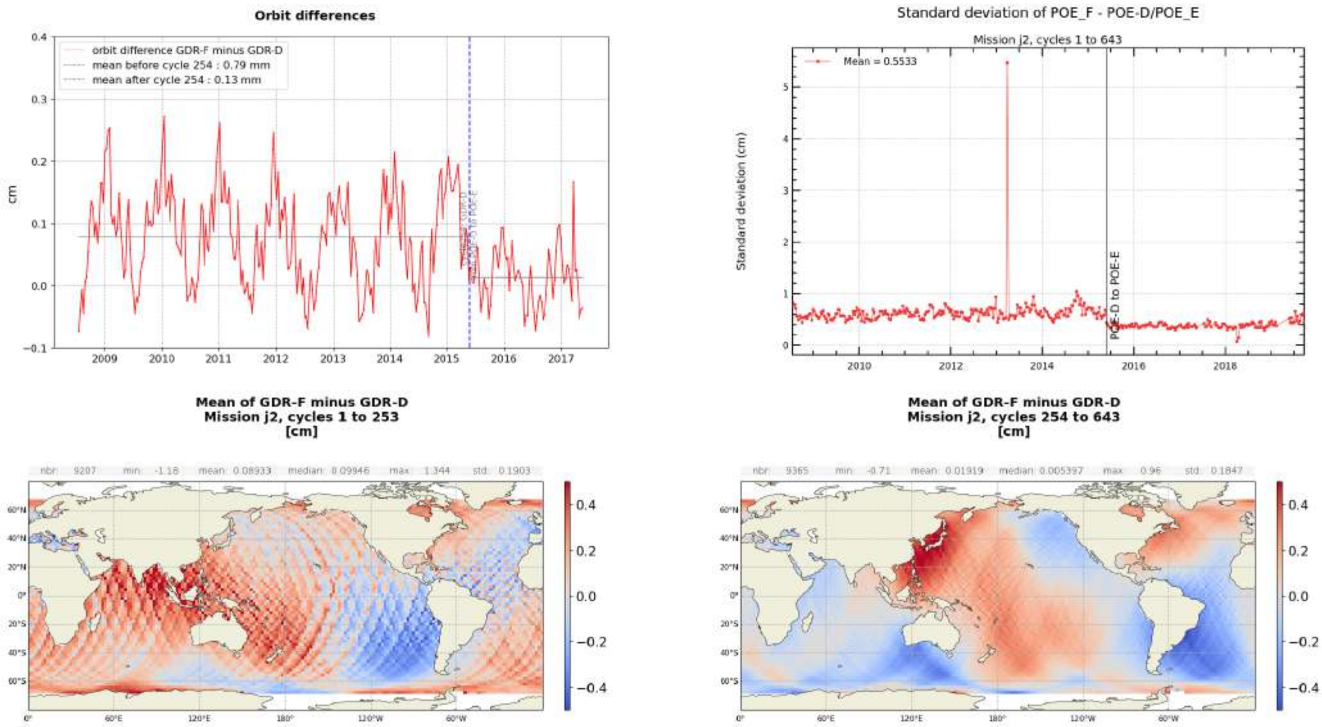

*Figure 17: Difference between GDR-F (POE-F) and GDR-D (POE-D+POE-E) orbit solutions : Mean (**left**) and standard deviation (**right**). Mean difference map between GDR-F and GDR-D orbits before cycle 253 (**bottom left**) and after cycle 254 (**bottom right**).*

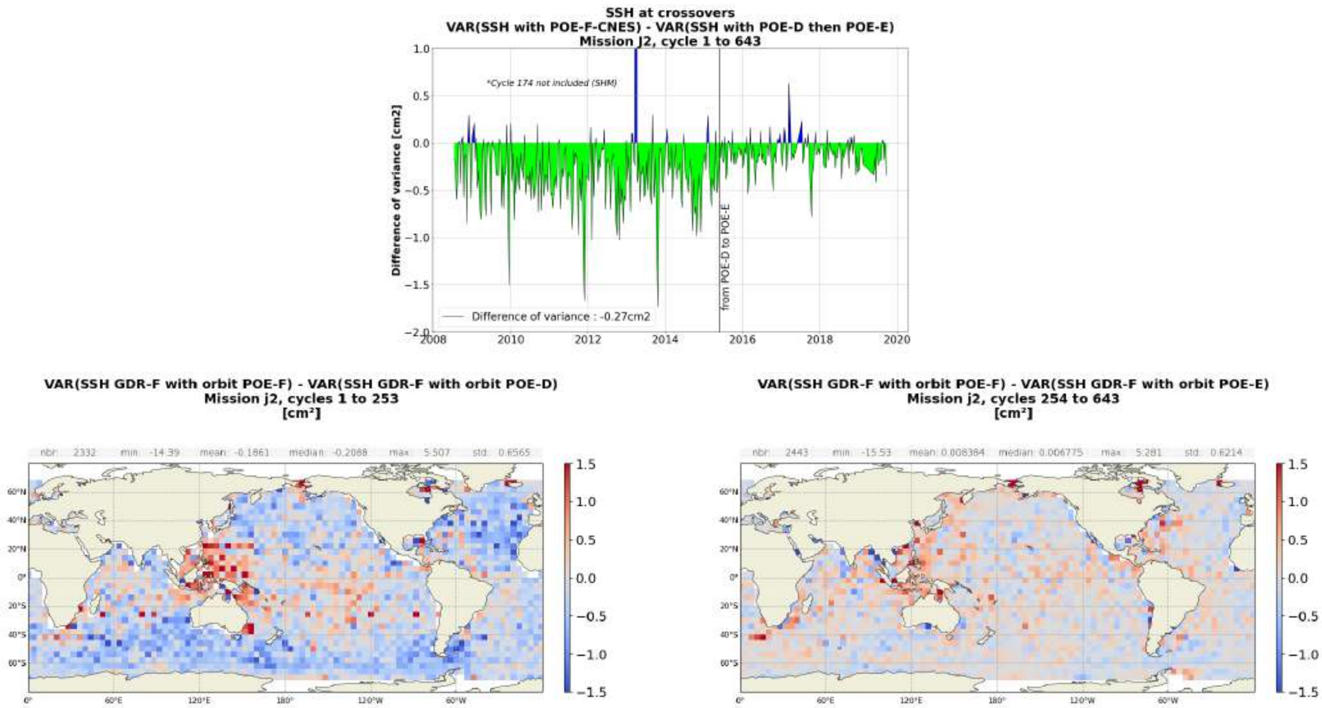

*Figure 18: Difference of variance between POE-F and POE-D/POE-E, monitoring (**top**) and map before cycle 253(**bottom left**) and after cycle 254 (**bottom right**)*

5.3. Radiometer parameters

In this part, a comparison between GDR-D and GDR-F is realized for radiometer parameters. Note that an AMR drift had been observed in GDR-D dataset and mentioned since 2015 annual report [6].

5.3.1. Brightness temperatures

Daily monitoring of the mean difference (GDR-F minus GDR-D) of brightness temperatures are really stable during repetitive phase but there is some jump for tb_340 and tb_187 between 2017 and 2019. In average, these differences are (see figure 19):

- near -1.2 K for tb_340 before move from interleaved ground track to LRO, near -0.9 K during LRO phase and at the beginning of iLRO phase then near -0.6 K for the rest of iLRO phase
- near 0.9 K for tb_238 stable in time during all the mission
- near 0.4 K for tb_187 before 2017, then 0.68 K during a chort period on 2017 and near 1 K between 2017 and 2019.

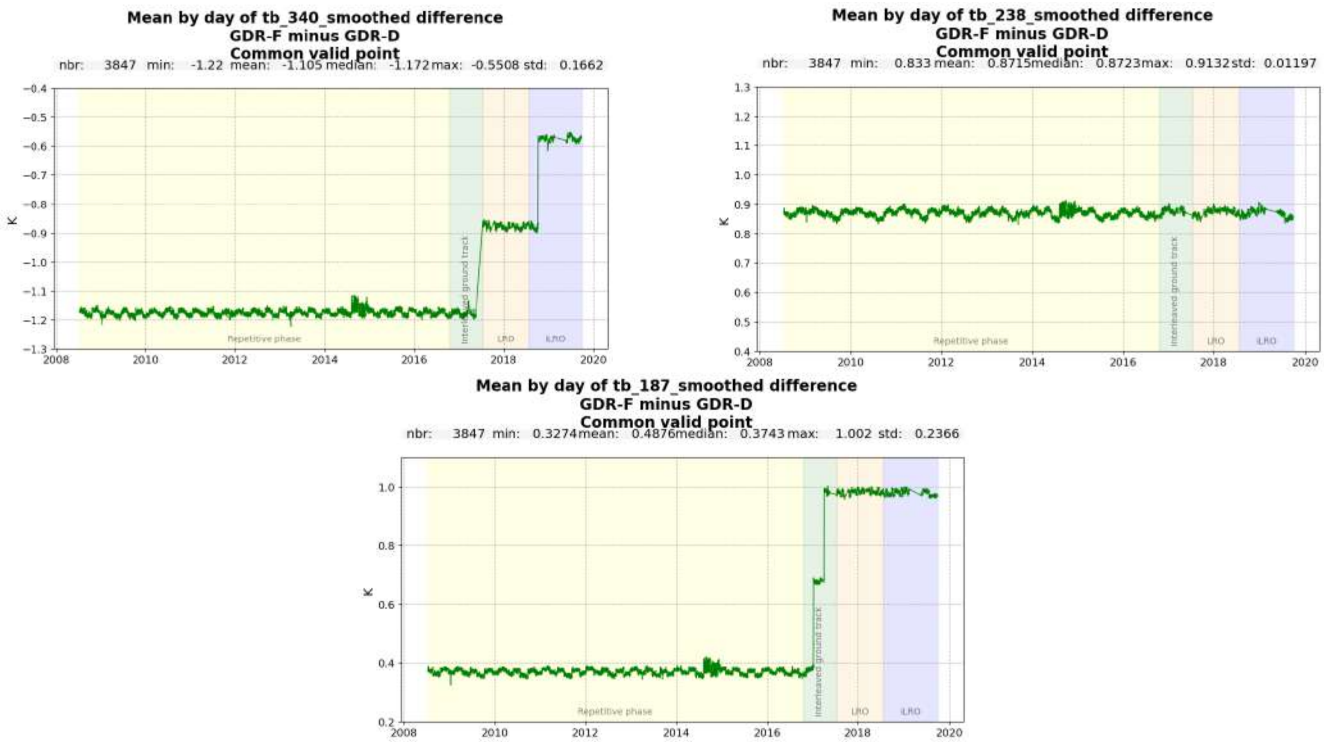

Figure 19: Brightness temperatures: mean per day (selection on SLA_MLE4 valid points only).

5.3.2. Radiometer minus model wet tropospheric corrections difference

Thanks to new calibration coefficients, radiometer minus model wet tropospheric corrections difference (d_tropo) is closer to zero (bottom left of figure 20). Mean difference between GDR-D and GDR-F radiometer wet tropospheric correction is quite stable between -7.4 and -7.0 mm in average over the repetitive phase. Some jump are observed on wet tropospheric corrections difference between 2017 and 2019 (+3.5 mm in total) and can be linked to jump on brigthness temperature for channel 18.7 GHz and 34.0 GHz (figure 19). Regional variations averaged over the whole periode are lower than 2 mm (bottom right figure 20).

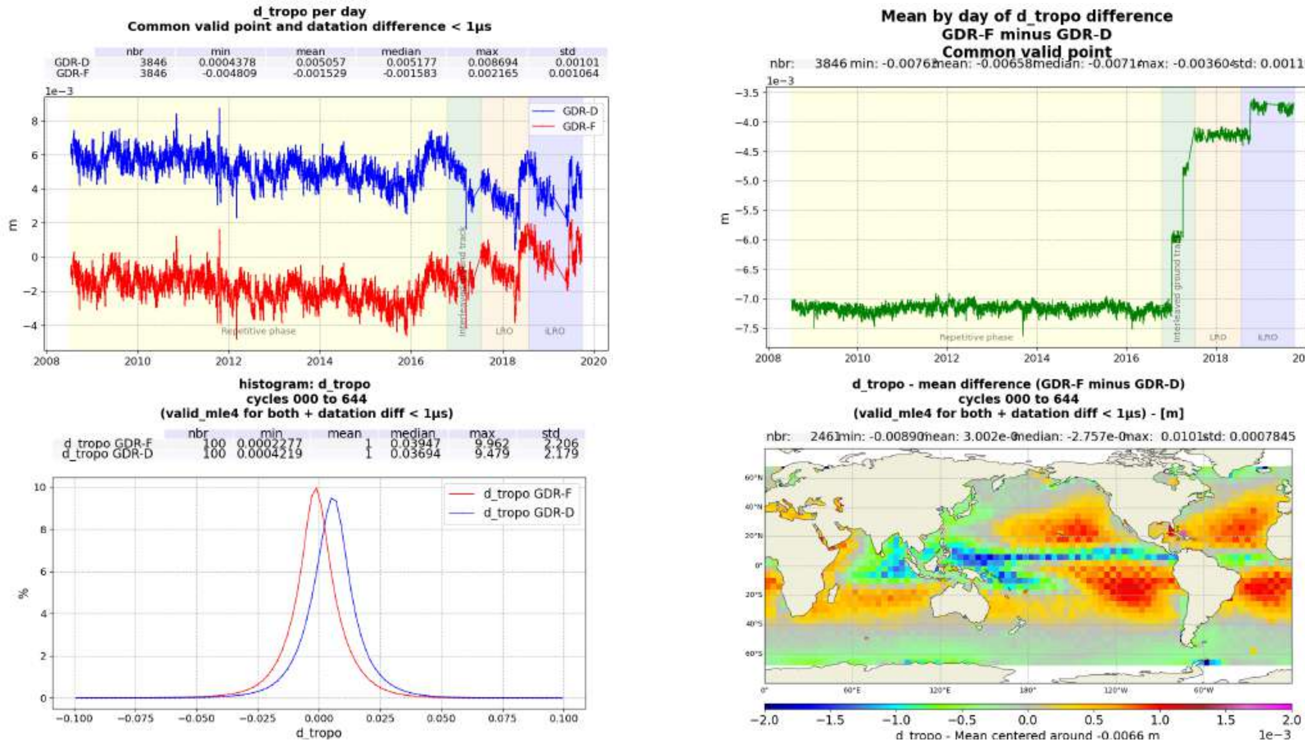

Figure 20: Radiometer minus model wet tropospheric corrections (selection on SLA_MLE4 valid points only).

Except over the Caspian sea and the gulf of Carpentaria in northern Australia, there is no significant impact on SSH variance at crossovers. The global variance difference is lower than $0.1cm^2$ (figure 21).

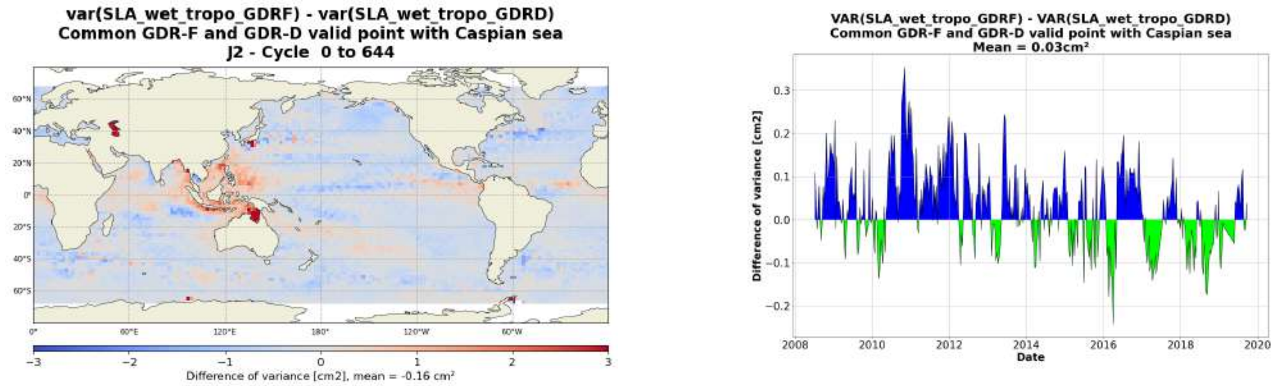

Figure 21: Difference of along-track SLA variance using wet tropospheric correction GDR-F or GDR-D

A small impact of this radiometer reprocessing is visible near coast (figure 22) as differences are slightly less stable for distance to coast under 50km.

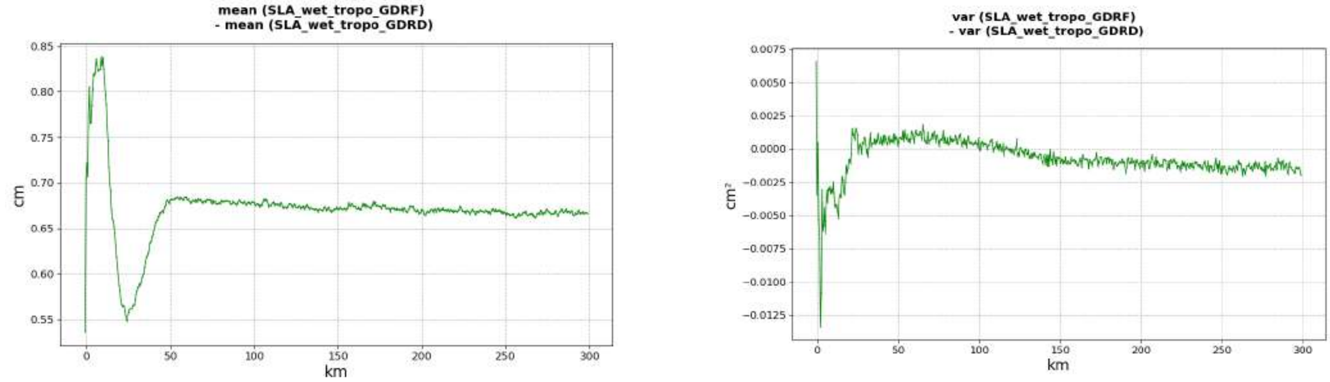

Figure 22: Difference of along-track SLA mean and variance with regard to distance to coast

5.3.3. Atmospheric attenuation

The atmospheric attenuation applied to sigma0 is derived from radiometer parameters. Atmospheric attenuation is slightly lower for GDR-F than GDR-D: the difference between GDR-F and GDR-D atmospheric attenuation is very low (<0.01 dB on daily averaging), with a mean of 0.005 dB during all the repetitive phase. Some jumps are observed between 2017 and 2019 (linked to jumps on brigthness temperature for channel 18.7 GHz and 34.0 GHz, visible on figure 19). This change is small (1 to 2%) compare to mean of atmospheric attenuation (near 0.25 dB). Differences are slightly higher in the inter-tropical zone, where the atmospheric attenuation is higher, and near coast (see right of figure 23).

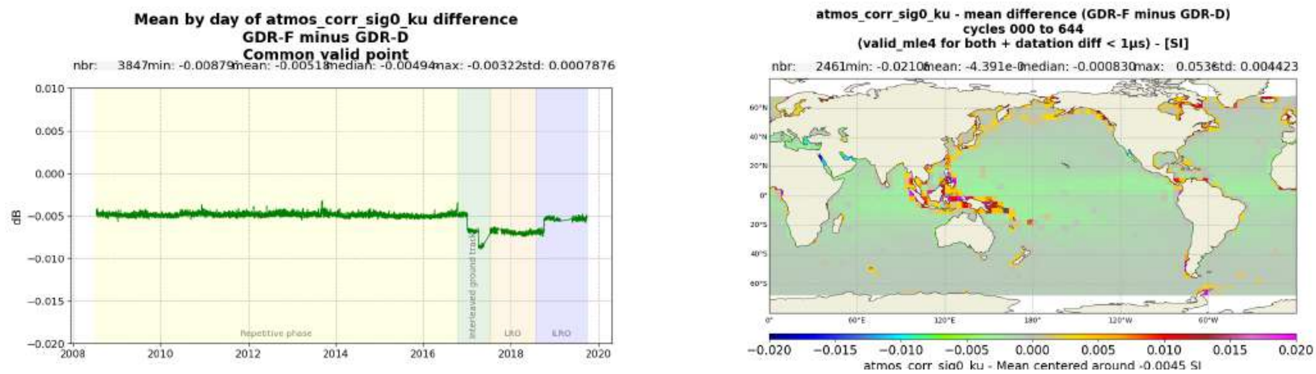

Figure 23: atmos_corr_sig0_ku (selection on SLA_MLE4 valid points only).

5.3.4. Atmosphere cloud liquid water and water vapor content

Radiometer atmosphere cloud liquid water and water vapor content are slightly modified with reprocessing. It leads to a water vapor content from radiometer difference about 1.07 kg/m^2 in average during the repetitive period (top of figure 24). Some jumps are observed between 2017 and 2019 (linked to jumps on brigthness temperature for channel 18.7 GHz and 34.0 GHz visible on figure 19). Atmosphere cloud liquid water from radiometer difference is about 0.011 kg/m^2 in average over the whole reprocessed period (bottom of figure 24).

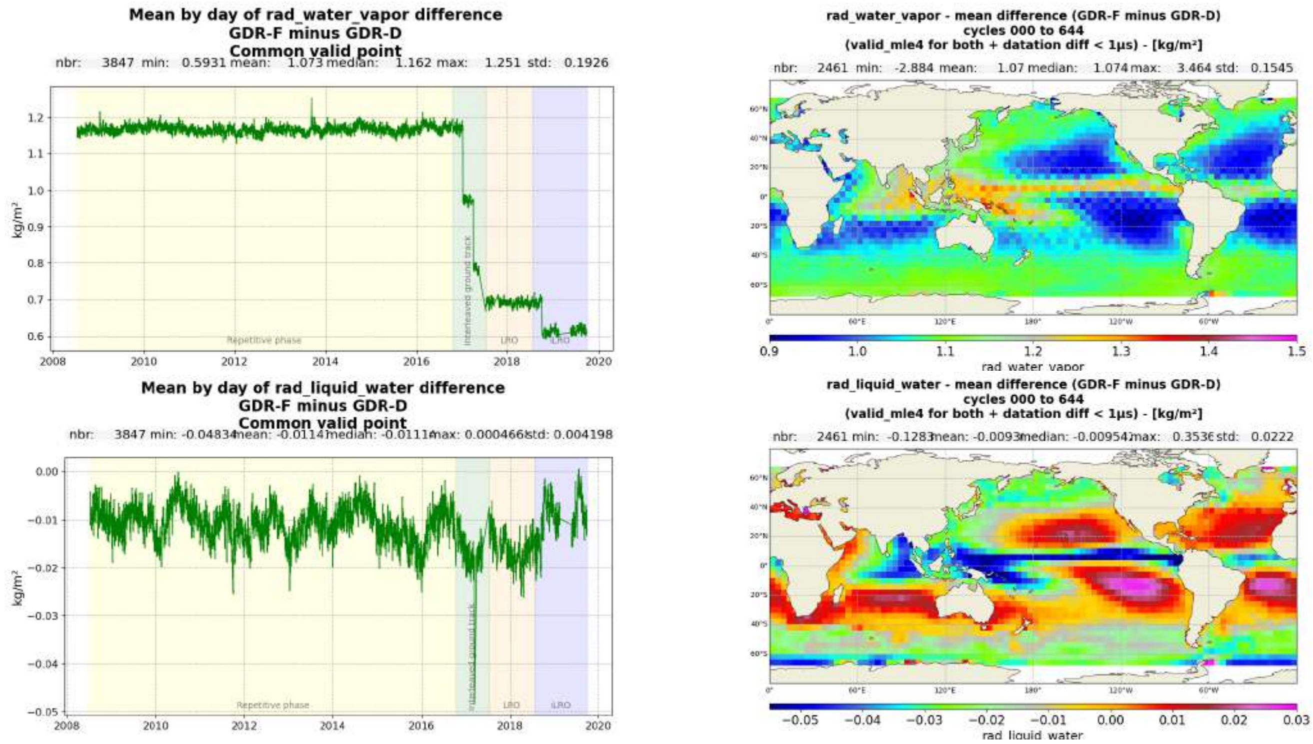

*Figure 24: Water vapor content from radiometer difference in kg/m^2 **(top)** and atmosphere cloud liquid water from radiometer difference in kg/m^2 **(bottom)** (selection on SLA_MLE4 valid points only).*

5.4. Altimeter parameters and corrections derived from the altimeter

In this part, a comparaison between GDR-D and GDR-F is realized for altimeter parameters and corrections derived from the altimeter. Main differences in product are detailed in table 8.

	GRD-D	GRD-F
CAL1 Total Power of the PTR	1e-2 precision	1e-4 precision
CAL 2 (LPF) normalization	Normalization by max gate	Normalization by averaging gates
MLE4 Mispointing validity map	Not provided	Provided
Waveform classification	-	Neural network
Adaptive retracking	-	Adaptive retracking
Tracker Range Rate	Not reported in S-IGDRs and S-GDRs	Reported in S-IGDRs and S-GDRs
Waveform	Provide the waveforms non corrected from the LPF filter	Provide the waveforms corrected from the LPF filter
Doppler correction	Applied on ocean retracked ranges	Applied on all retracked ranges

Table 8: Altimeter difference between GDR-D and GDR-F

5.4.1. Range estimations from waveforms and range rms of 20Hz measurements

GDR-F reprocessing introduce no significant change for range_rms of 20Hz elementary measurements versus waves height (figure 25).

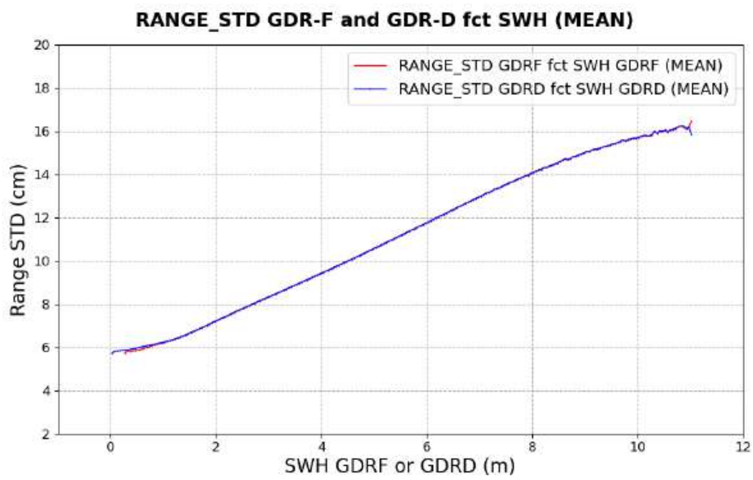

Figure 25: Range RMS fct SWH

NOTE : In a original (not released) GDR-F processing, range estimations in GDR-F were slightly depreciated in 2013 due to an anomaly in USO drift correction information used between 13th june and 1st october, which led to a near linear drift of 1.3mm during this period (figure 26). In order to correct this anomaly, a correction had been applied on GDR-F between 13th june and 1st october to all variable using USO drift correction: USO drift correction, range (MLE4, MLE3, Adaptive, etc. in Ku/C band for 1hz and 20hz data), SSHA (MLE4, MLE3 and Adaptive in Ku/C band). In the final released reprocessing, a residual piece-wise constant anomaly can always be seen on this correction (bottom right of figure 26) due to data encoding (0.0001m). As mentioned in part 2, netcdf files in this case can be identified thanks to the xref_doris_uso global attribute.

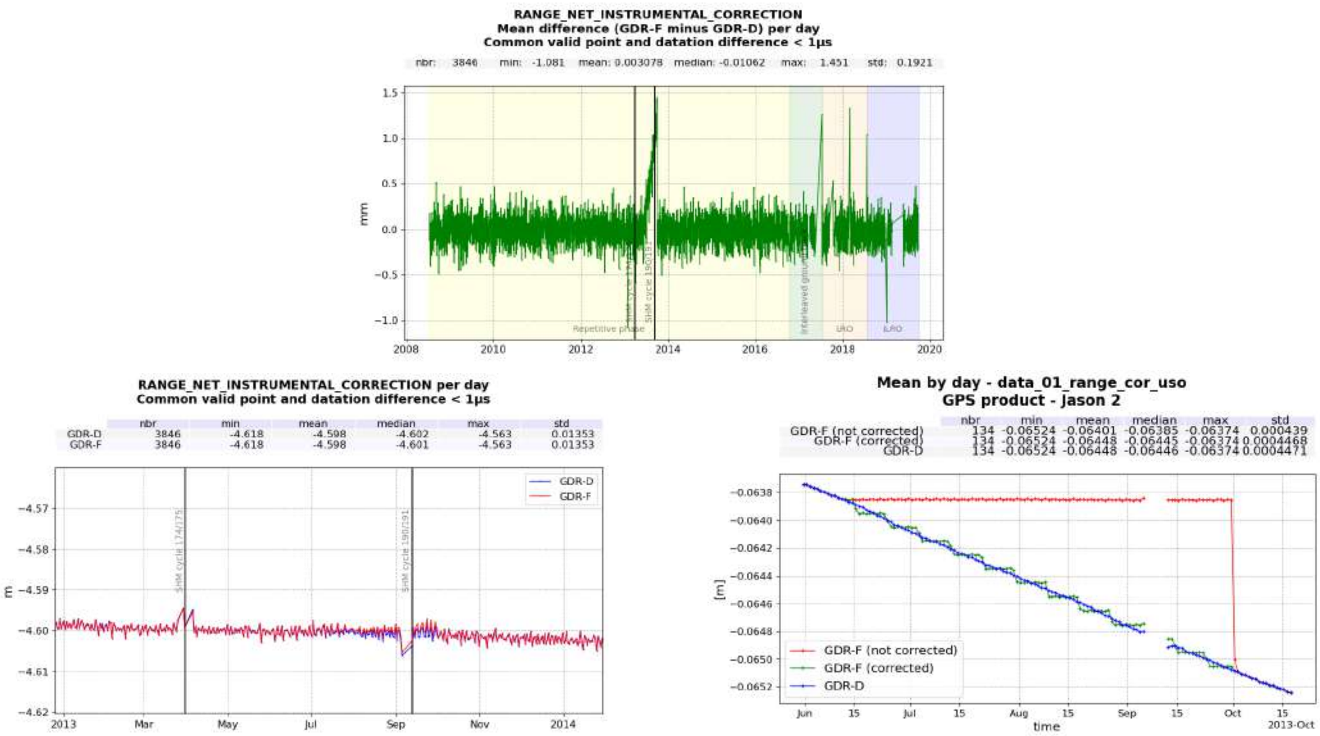

*Figure 26: Difference per day of range net instrumental correction between GDR-F and GDR-D before patching xref_doris_uso **(top)**, Range net instrumental correction **(bottom left)** and USO correction patch **(bottom right)** per day for GDR-D (blue), GDR-F before correction (red) and GDR-F after correction (green) during 2013 anomaly.*

5.4.2. Square off nadir angle from waveforms / Mispointing

There is no significant impact of reprocessing on mispointing from waveforms (<0.0015 deg^2 on daily averaging).

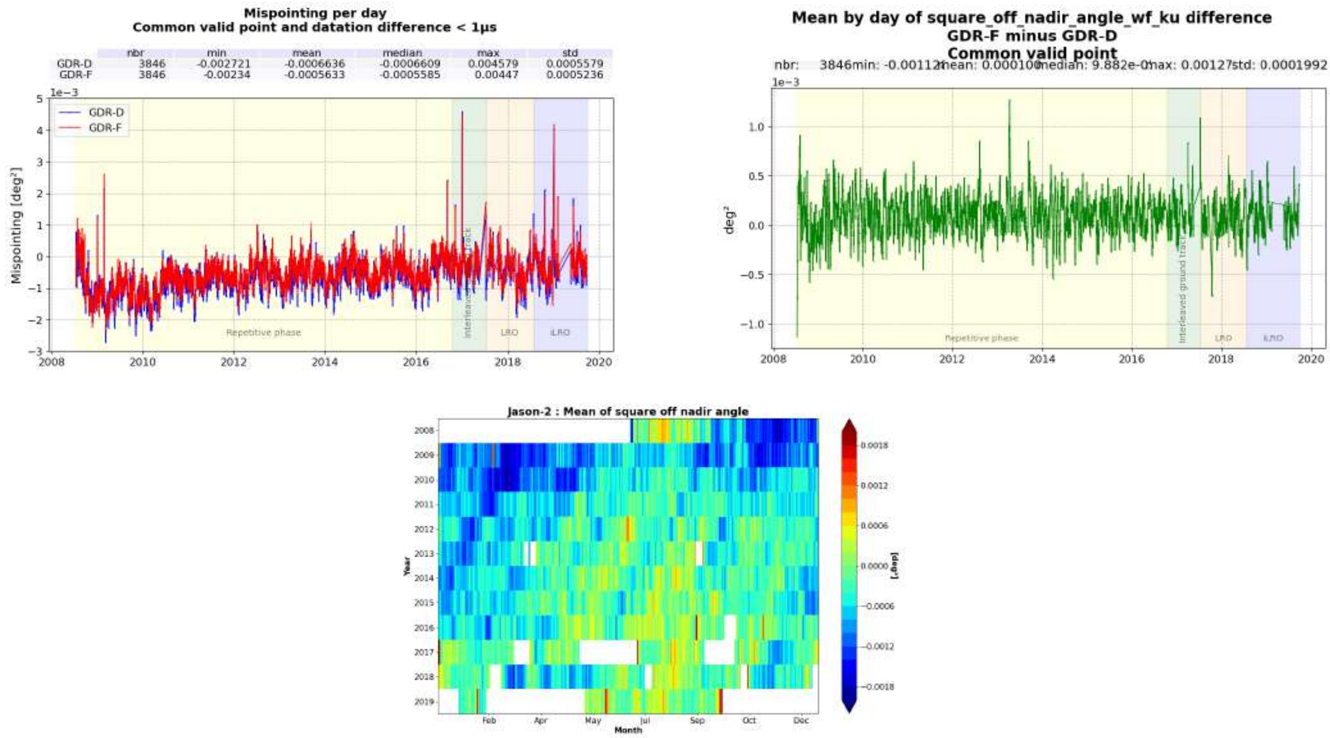

Figure 27: square_off_nadir_angle_wf_ku : Daily mean of GDR-F and GDR-D (top left), GDR-F minus GDR-D (top right) and GDR-F (bottom) (selection on SLA_MLE4 valid points only).

5.4.3. Significant Wave Height / SWH

There is no significant impact of reprocessing on swh estimations higher than 1 meter. Note that the processing for swh lower than 1m is different between GDR-D and GDR-F. As a consequence, there is no swh at 0m for GDR-F against near 0.5 % of point for GDR-D (bottom left of figure 28). This is directly linked to the evolution in Look Up Tables (LUT) correction applied to measured swh. Differences to ERA5 model are then slightly modified (bottom right of figure 28).

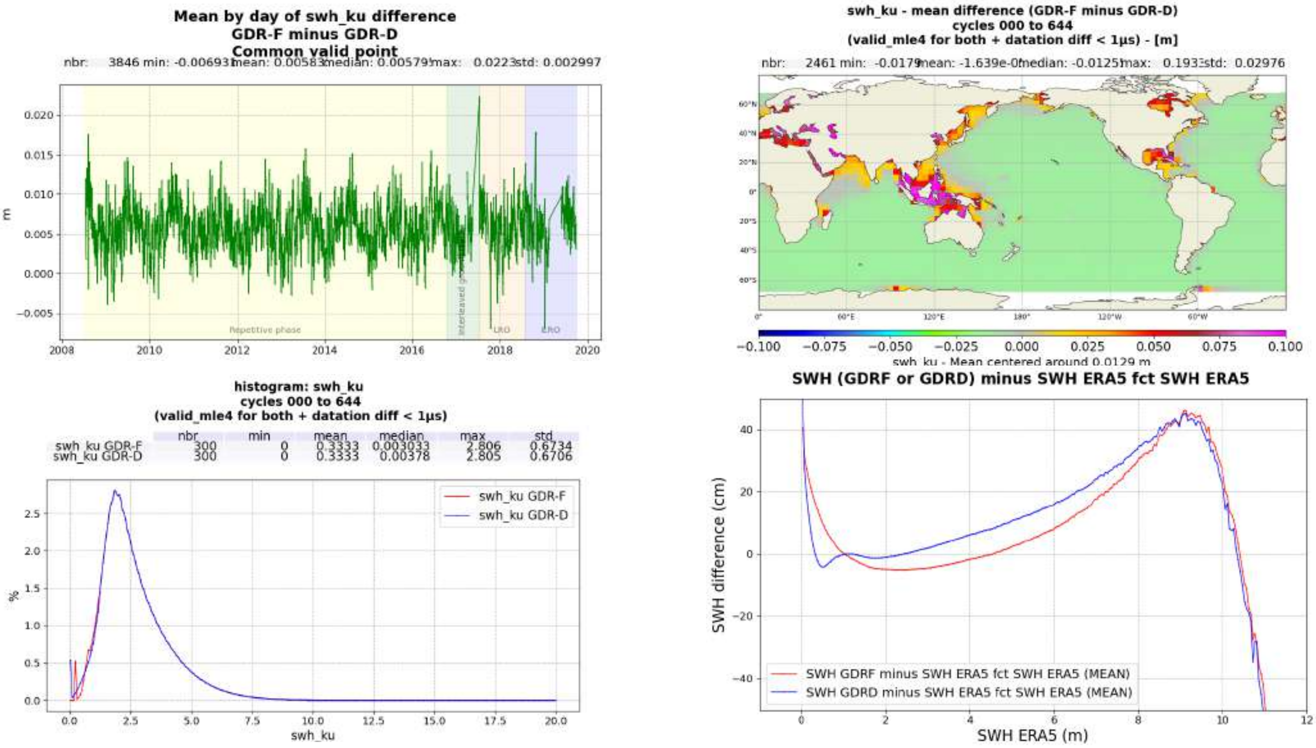

*Figure 28: Daily mean (m) of swh_ku GDR-F minus GDR-D **(top left)** and map averaging **(top right)**, histograms of swh for GDR-F and GDR-D **(bottom left)** and SWH (GDR-F and GDR-D) minus SWH ERA5 fct of SWH ERA5 **(bottom right)** (selection on SLA_MLE4 valid points only).*

One can notice some jumps and slope change on GDR-F histograms for SWH lower than 1.25 m (see figure 29). This changed are related to LUT, whose slope is very important for low swh. In addtition, LUT is calculated with constant interval of swh (25 cm) but after correction, this interval can varying between 15 and 25 cm. This new interval changed at 20.48 cm, 50.48 cm, 65.65 cm, 80.87 cm, 100.46 cm and 117.36 cm when there is slope change visible on swh histogram at the step 80.87 cm.

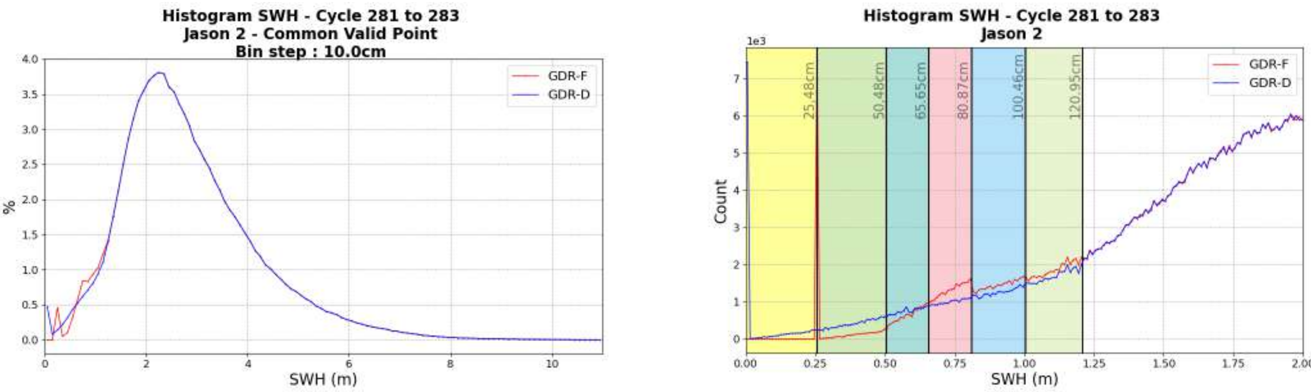

Figure 29: Histograms of SWH between cycle 283 to cycle 285 for GDR-F and GDR-D (selection on SLA_MLE4 valid points only) .

5.4.4. Backscatter coefficient / Sigma0

The GDR-F minus GDR-D difference of backscatter coefficient (top left of figure 30) shows a bias between -0.02 and 0.02 dB in daily averaging. This behavior is probably linked to the change in filter normalization (by averaging gates instead of by max gates) mentionned in table 8 and the associated Look Up Tables profiles with regard to SWH estimations. Some patterns on the map of this difference averaging over the whole period (top right of figure 30) appear and can be linked to these variations steps as there are also seen on dedicated to cycle 220 focused figures (at bottom part of figure 30).

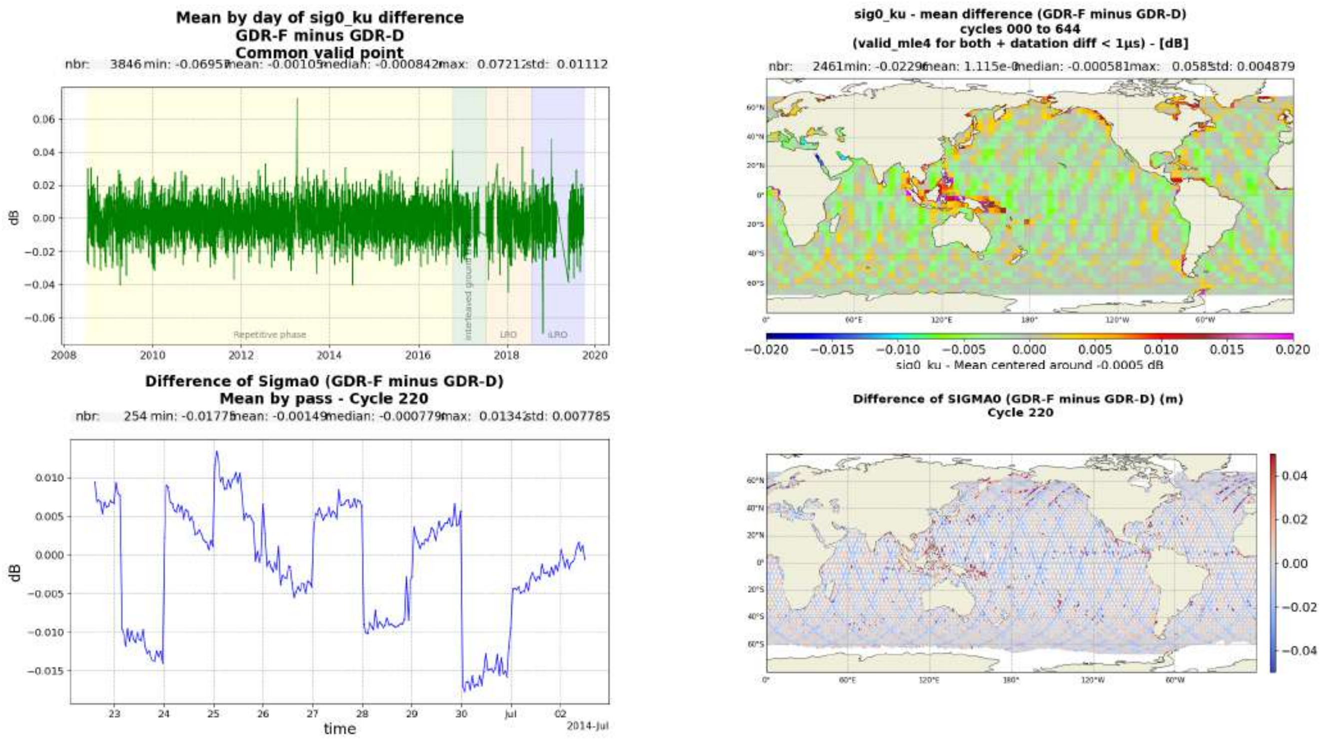

Figure 30: Daily mean ***(top left)*** *and map averaging* ***(top right)*** *of sig0_ku GDR-F minus GDR-D (selection on SLA_MLE4 valid points only). Mean by pass* ***(bottom left)*** *and map of value* ***(bottom right)*** *over cycle 220 (selection on SLA_MLE4 valid points only)*

5.4.5. Wind-speed

A dedicated to Jason-2 GDR-F bias is applied to sigma0 before computing the Collard algorithm. It results in slightly higher wind-speed estimations (+0.16 m/s in average) (figure 31).

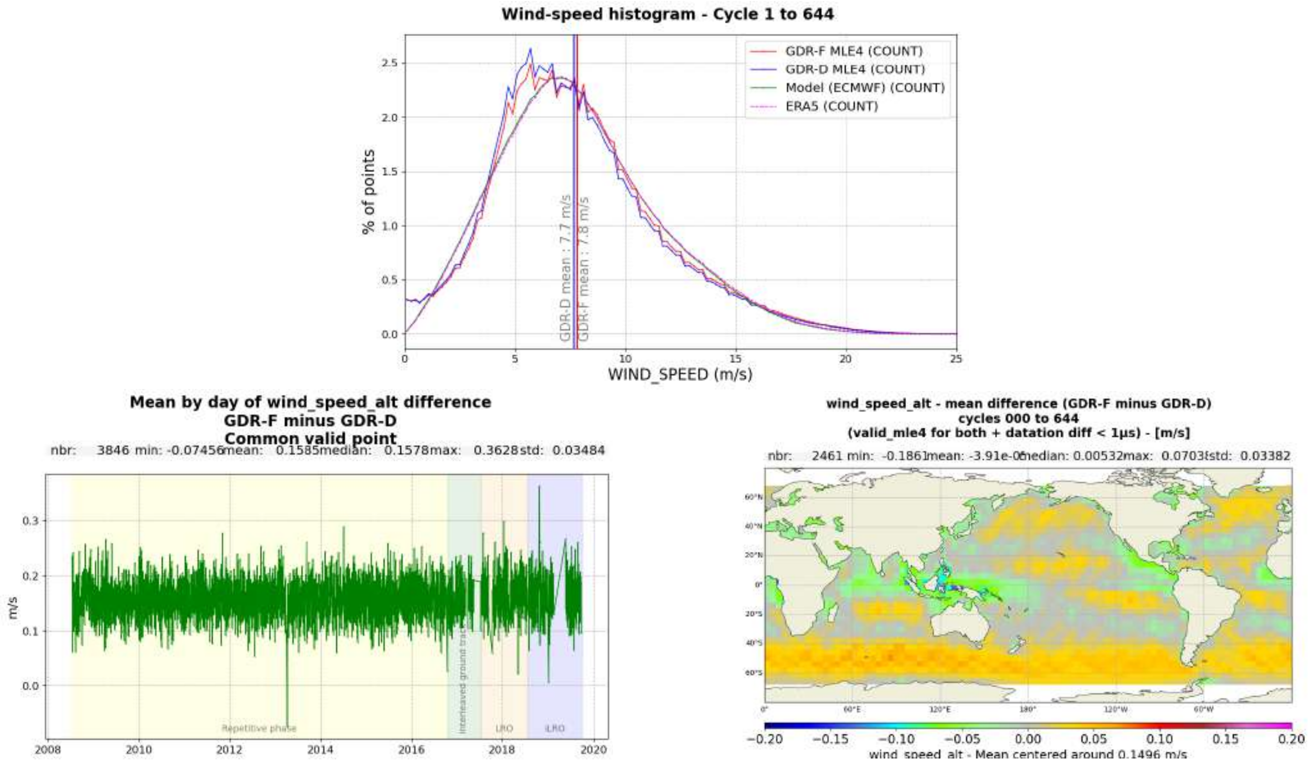

*Figure 31: Histograms of altimeter and model wind speed **(top)**, daily mean **(left)** and map averaging **(right)** of wind_speed_alt GDR-F minus GDR-D (selection on SLA_MLE4 valid points only).*

5.4.6. Sea State Bias

In GDR-D product, Sea State Bias (SSB) was computed with an empirical solution fitted on Jason-2 GDR-C data (Tran 2011). For GDR-F, SSB is computed using one year of 2016/2017 Jason-3 GDR-F dataset (Tran 2020). The global bias betwwen GDR-D and GDR-F sea state bias is -1.88 cm in avaerage, with difference fluctuations between -2 and -1.75 cm (figure 32).

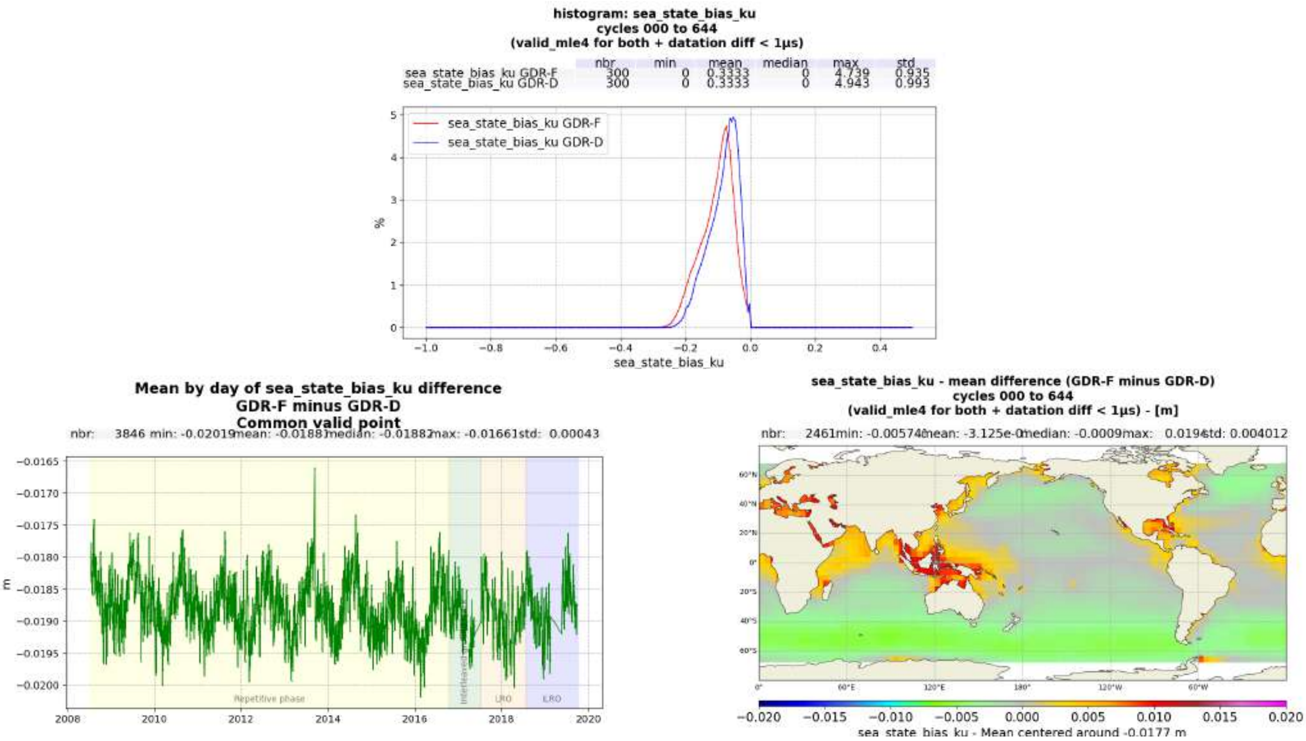

*Figure 32: GDR-F and GDR-D histograms of sea_state_bias_ku **(top)**, daily mean **(left)** and map averaging **(right)** of sea_state_bias_ku GDR-F minus GDR-D (selection on SLA_MLE4 valid points only).*

5.4.7. Dual-frequency ionospheric correction

An iterative filtering method was applied to the ionospheric correction in the GDR-F altimetry products. The process is applied to the non filtered solution computed from the formula:

$$Iono = \delta f[(Range_{Ku} + SSB_{Ku}) - (Range_C + SSB_C)] \tag{4}$$

with :

$$\delta f = (FrequencyC_{band})^2/((FrequencyKu_{band})^2 - (FrequencyC_{band})^2) \tag{5}$$

with, for Jason-2, frequency = 5.3 GHz for C-band and 13.575 GHz for Ku-band.

The iterative filtering scheme was developed to achieve two main goals:

- Base the correction on as many dual-band ionospheric observations as possible
- Improve the correction where altimetric observations are discontinuous or isolated.

The selection of the ionospheric observations used for the correction is independent from the quality of sea level observations. This maximizes the number of observations selected, but at the same time increases the number of potential outliers. The iterative filtering applies a median and a Lanczos filter in sequence, in order to progressively reduce the number of outliers in the ionospheric observations used to compute the final filtered correction. Since the filtered correction has long spatial correlation scales, a spline interpolation is used to fill gaps in the interpolated correction up to few hundreds kilometers.

More details and an overview of the main results on this method is presented in "Filtering ionospheric correction from altimetry dual frequencies solution" report [16]. In particular, it clarifies how more points are edited near coast and along the border of the Antarctic sea ice and less points are edited on open sea with iterative filtered corrections (part 4.2, figure 19 of [16]).

For Jason-2, adding this filtering solution to the ionospheric correction used during sea surface height computation leads to a variance reduction of the along-track SLA by 4.0 cm^2 (figure 33) in average. This reduction is visible everywhere (blue boxes = negative values on top left map of figure 33). A variance reduction at crossovers is also visible as shown on figure 10, and here at bottom of figure 33. There is no significant impact on mean of ssh differences at crossovers (not shown here).

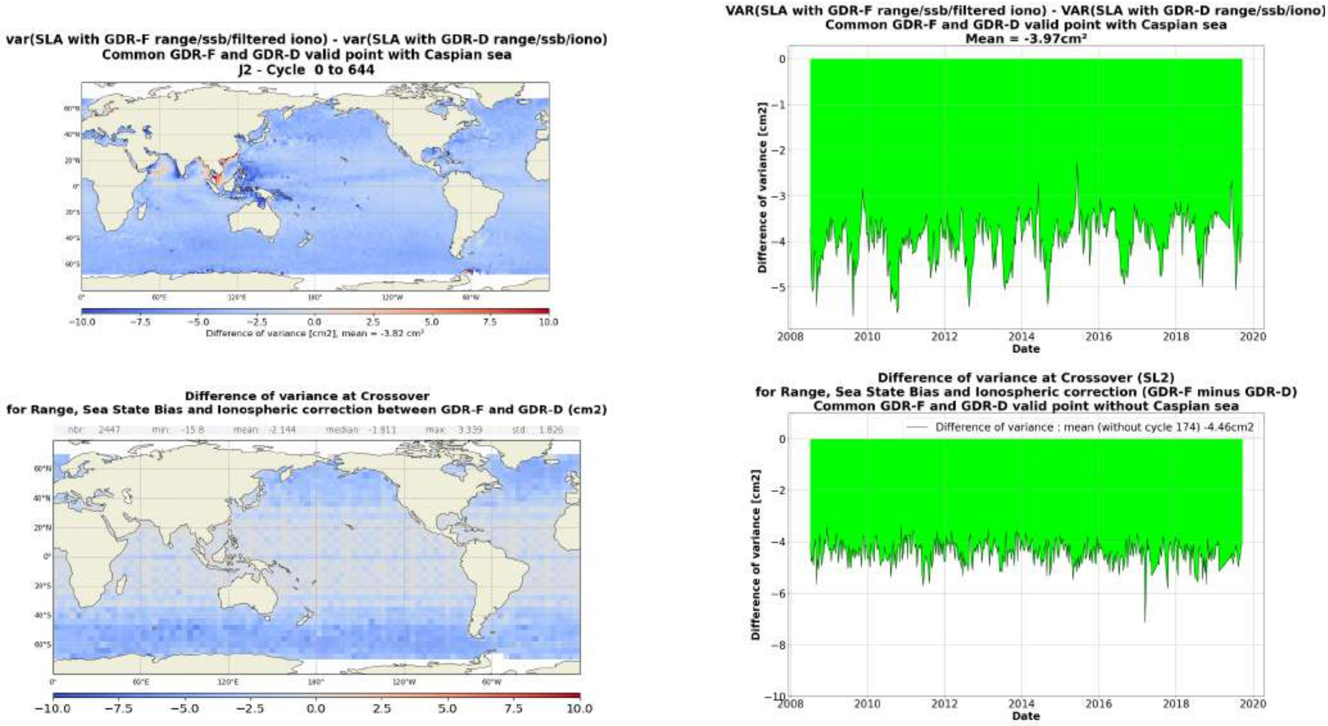

*Figure 33: Difference of GDR-F and GDR-D SLA variance using filtered ionospheric correction in case of GDR-F and non filtered solution in case of GDR-D **(left)**. Cyclic monitoring **(right)**. Variance difference at crossovers **(bottom)**, note that a section is done on $|latitude| < 50$, bathymetry<-1000m and on shallow waters on the difference at crossover monitoring (bottom right).*

Finally, note that a 3D sea state bias solution, including an additional input parameter from MFWAM (WAVERYS) mean wave period is now available into GDR-F. A dedicated study is done to analyse the impact of this new solution at the end of this report (see part 8).

5.5. Others corrections involved into SSH computation

5.5.1. Pole tide correction

The pole tide altimeter correction is used to correct the response of the solid earth and oceans to the polar motion. The Wahr (1985) model has been used for all missions since TOPEX and another model is now available (Desai 2015). Legeais et al. (in 2015) showed the last model has a significant positive impact on the regional mean sea level trends and the comparison with independent in-situ data (Argo profiles) has demonstrated that the use of this model reduces the amplitude of the annual signal of the global mean sea level. A new recommendation for Mean Pole Location equation was done in 2017: this model for the linear mean pole is recommended based on a linear fit to the IERS C01 time series spanning 1900 to 2015: in milliarcsec, Xp = 55.0+1.677*dt and Yp = 320.5+3.460*dt where dt=(t-t0), t0=2000.0 and assuming a year=365.25 days. The new mean pole location equation **has a significant impact on the regional mean sea level trends** thanks to the remove of the long term mean pole drift in pole tide computation (see part 8.2 in [13]). There is no significant impact on performances at crossover. A small reduction of along-track SLA variance (-0.12 cm^2) is visible in average over the whole mission period (figures 34).

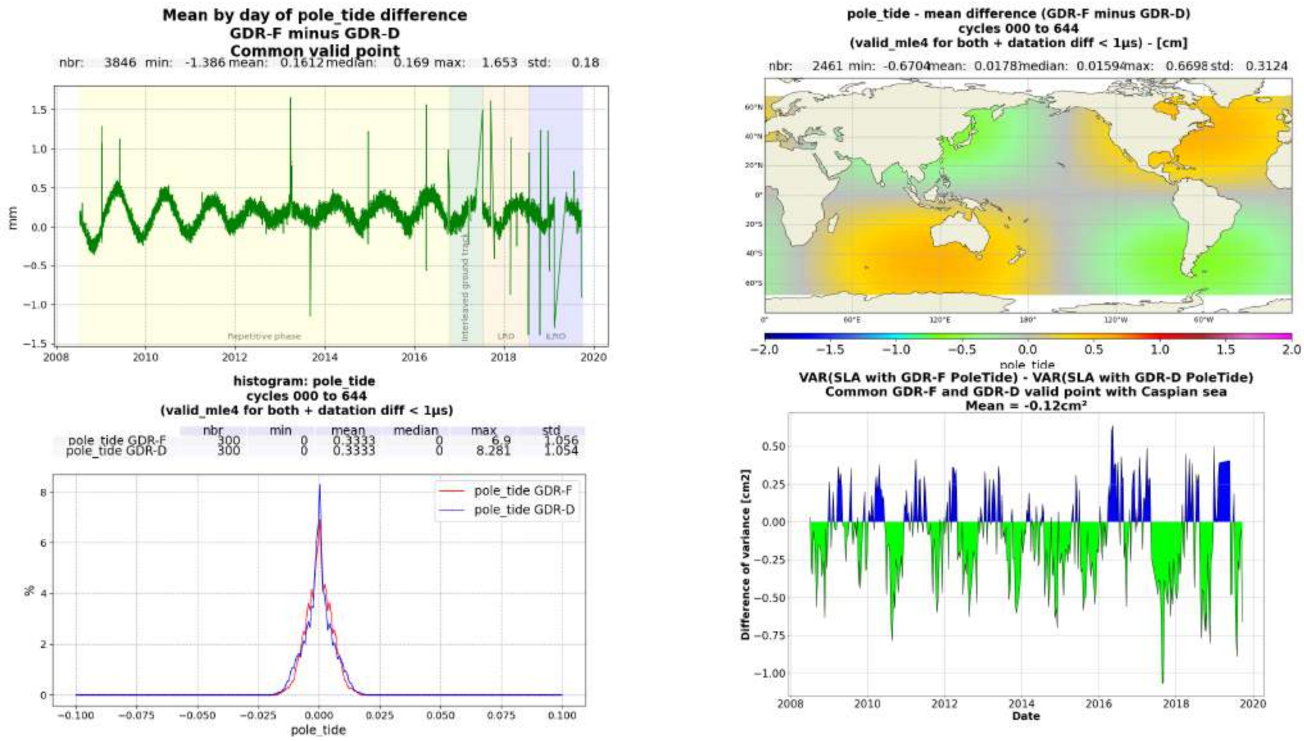

Figure 34: GDR-F minus GDR-D pole_tide difference ***(top)*** *(selection on SLA_MLE4 valid points only). GDR-F and GDR-D histograms of pole_tide over the whole mission period* ***(bottom left)****. Difference of SLA variance between GDR-F without pole tide models Wahr (1985) and Desai (2015) on bottom right*

5.5.2. Global tide models

The latest global tide versions of the GOT and FES models (GOT4.10c or FES2014b [25]) are available instead of GOT4.8 or FES2004. Daily mean of old minus new GOT (top left figure 35)) or FES (top right figure 35)) models shows slight differences of few milimeters, with a significant impact on 60 days signal in case of GOT. Note that in GDR-F, the reference SSHA uses the FES model instead of GOT in GDR-D. So that comparing GDR-F to GDR-D solution leads to compare FES14 to GOT4.8. In case of SSH difference at crossover points analysis, it has an impact on 120 days signal on cyclic mean, but no significant impact on local differences. (see bottom part of figure 35).

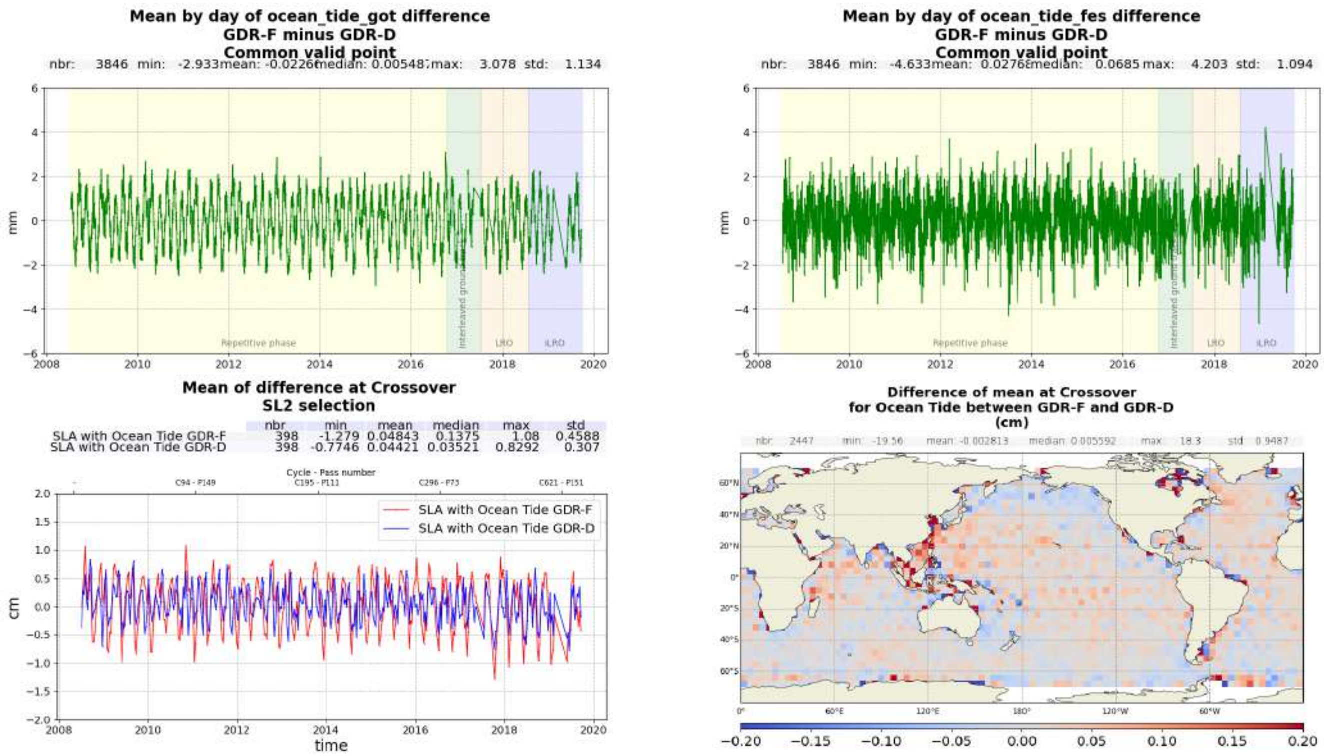

*Figure 35: Daily monitoring of GDR-F minus GDR-D GOT or FES ocean tide mean difference **(top)**. Mean difference of SSH at crossover between global tide models FES2014b and GOT4.8 **(bottom)***

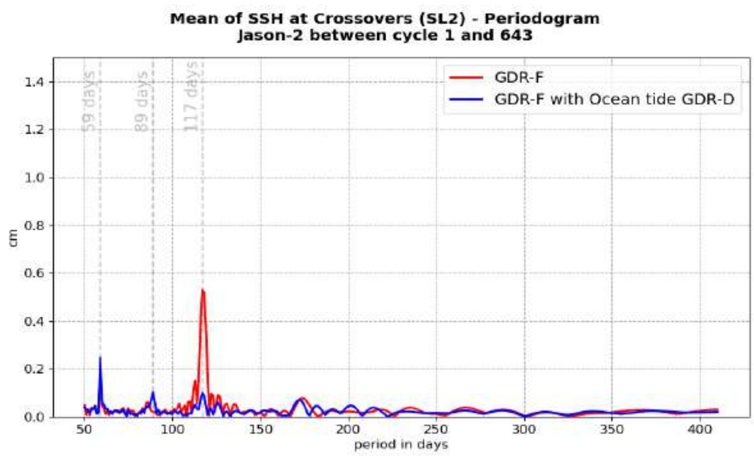

Figure 36: Periodgram of SSH mean at crossover for GDR-F (ocean tide FES14) and GDR-F with ocean tide from GDR-D (GOT4.8)

These solutions improve the coherence between ascending and descending passes as the global variance reduction of SSH crossover difference when using FES2014b instead of GOT4.8 has a value of about 0.56 cm^2 and variance of along-track SLA is lower using FES2014b than with GOT4.8 by 2.2 cm^2 (see figure 37). Global Mean Sea Level is equivalent with both solutions (GOT4.10c and FES2014, not shown here). Regional differences between SLA using FES2014 or GOT4.10 is not significant.

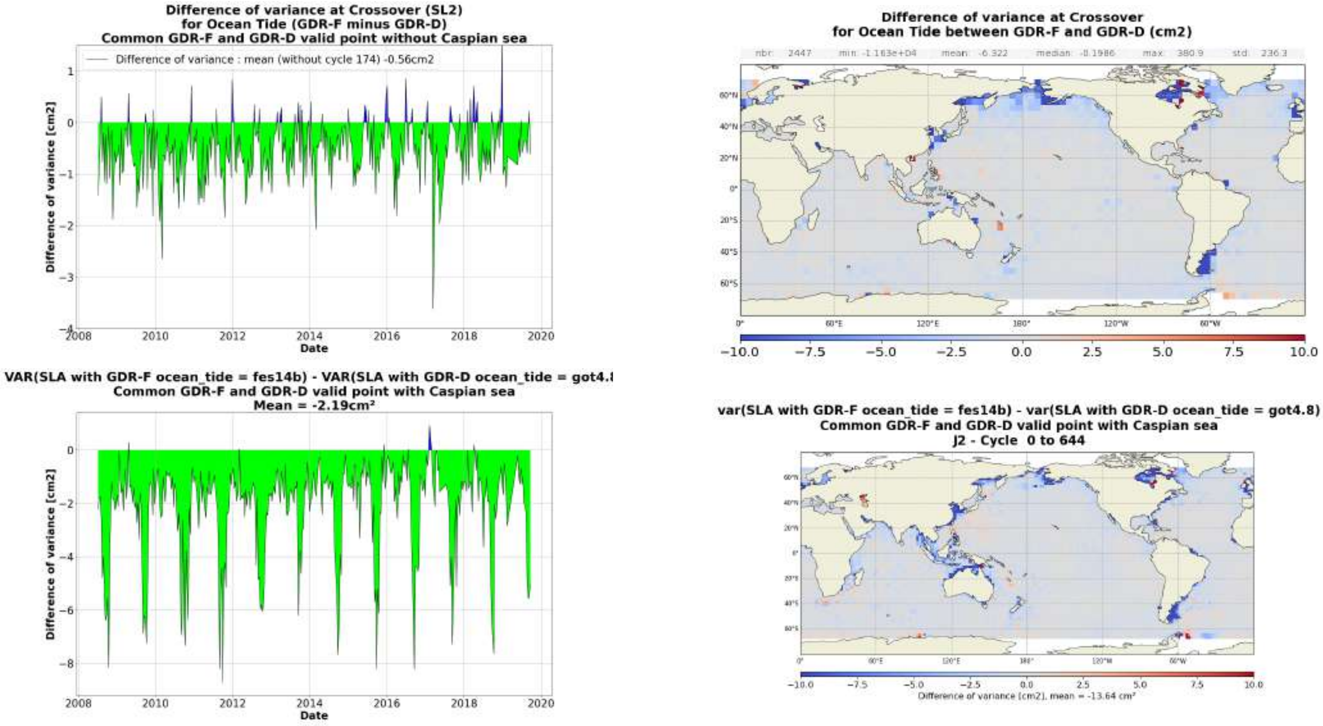

Figure 37: Difference of SSH differences at crossovers and along-track SLA variance between global tide models FES2014b and GOT4.8

<u>*Non equilibrium long period ocean tide height*</u> The long period non equilibrium part of global ocean tide model correction is deduced from FES14B 6 dynamic waves in GDR-F whereas it was from 4 waves from FES2004 model in GDR-D (see [1]). Note that this part of the correction is not included into ocean_tide_fes variable but it is now used into GDR-F SSHA variable computation (GDR-D ssha used ocean_tide_got solution, without this dynamic part). The GDR-F minus GDR-D difference of this correction is lower than 1 mm on daily averaging (figure 38).

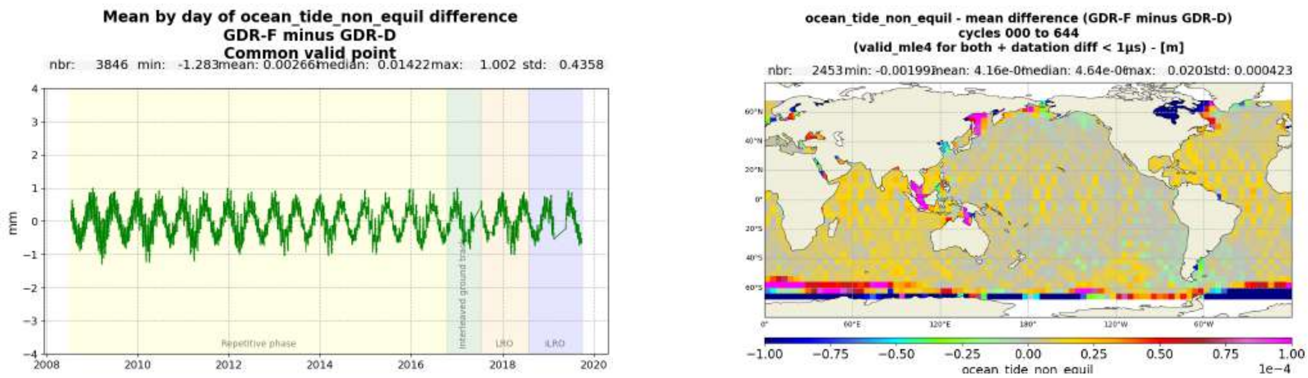

Figure 38: ocean_tide_non_equil GDR-F minus GDR-D difference (selection on SLA_MLE4 valid points only).

5.5.3. Internal tide

Following the scientific community recommendations, the correction related to internal tides is now available into GDR-F (Zaron Hret8.1 model for M2, K1, O1 and S2 waves). *[More information about internal tide correction in [26]]*. To take into account internal tide correction improves SSHA performance indicators on along-track Sea Level Anomaly and error at crossover. Over Jason-2 period, there is no significant impact on SSH difference at crossover points (bottom figure 39) or on Global Mean Sea Level trend estimation taking into account internal tides or not (not shown here). Variance of SSH differences at crossovers are compared using different solutions as a key performance indicator. In our case, this difference is lower by around 0.46 cm^2, with significant geographically correlated patterns where internal tides areas are defined (top right of figure 39). In the same way, a reduction is also visible in case of global along-track SLA variance (0.25 cm^2), with geographical 'blue' patterns (figure 40).

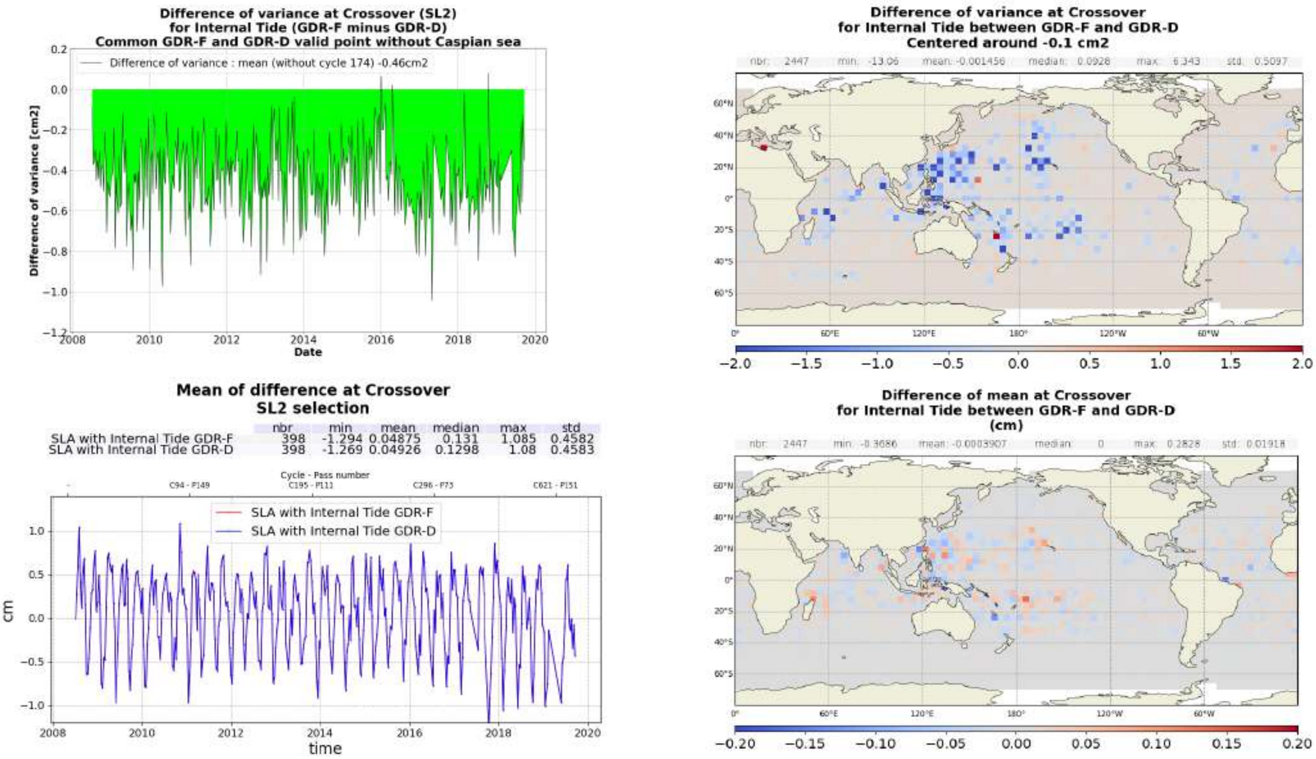

Figure 39: Variance and mean difference of SSH at crossover between GDR-F without internal tide and GDR-F with internal tide

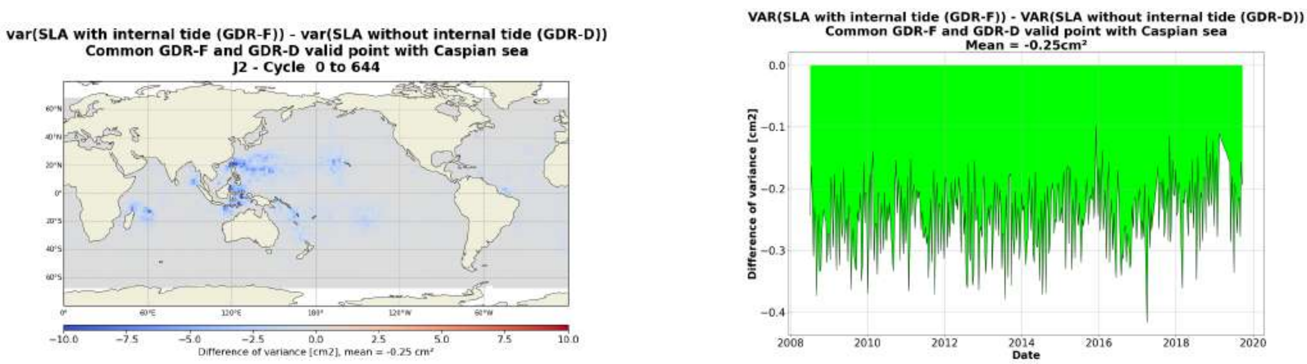

Figure 40: Difference of SLA variance between GDR-F without internal tide and GDR-F with internal tide

5.5.4. Mean Sea Surface (MSS)

GDR-D L2 products included non homogeneous versions of MSS. GDR-D MSS standard was CNES/CLS 11 (referenced over 7 years) and applied until cycle 327. After move to Long Repeat Orbit phase (at cycle 500), the CNES/CLS 15 (referenced over 20 years) solution had been used in order to improve the performance of SLA estimations. This was particularly useful out of the historical ground-tracks.
Two solutions (CNES/CLS 2015 and DTU 2018) are now available into GDR-F. The map of differences between the two MSS solutions (applicable only for cycles until 327, as the same solutions are used into GDR-D and GDR-F on LRO and iLRO, there is there no bias) shows a global bias of 2.4 cm. This is directly linked to the change of the reference period from 7 years to 20 years, associated to the global mean sea level rise over the 13 years [20]. Note that the change in reference ellipsoid (70 cm on global averaging) has been applied to mean sea surface before computing this analysis. Finally, the variance of along-track SLA is then reduced by 13.9 cm^2 (see figure 41), as the new solution better represents the Jason-2 period (see also part 4.2.).

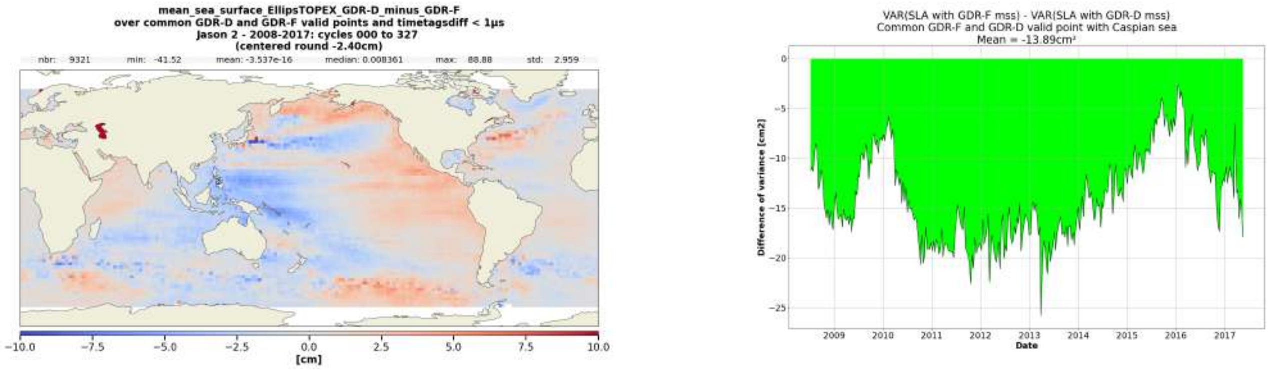

*Figure 41: GDR-F minus GDR-D MSS difference **(left)**. Difference of SLA variance between MSS CNES/CLS11 and MSS CNES/CLS15 **(right)***

5.6. Other ancilliary data

5.6.1. Mean Dynamic Topography (MDT)

Mean Dynamic Topography move from CNES/CLS-2009 for GDR-D to CNES/CLS-2018 for GDR-F. The latest version is +2.8 cm higher in average. Geographically correlated patterns of the difference can reach near 35 cm locally (see figure 42).

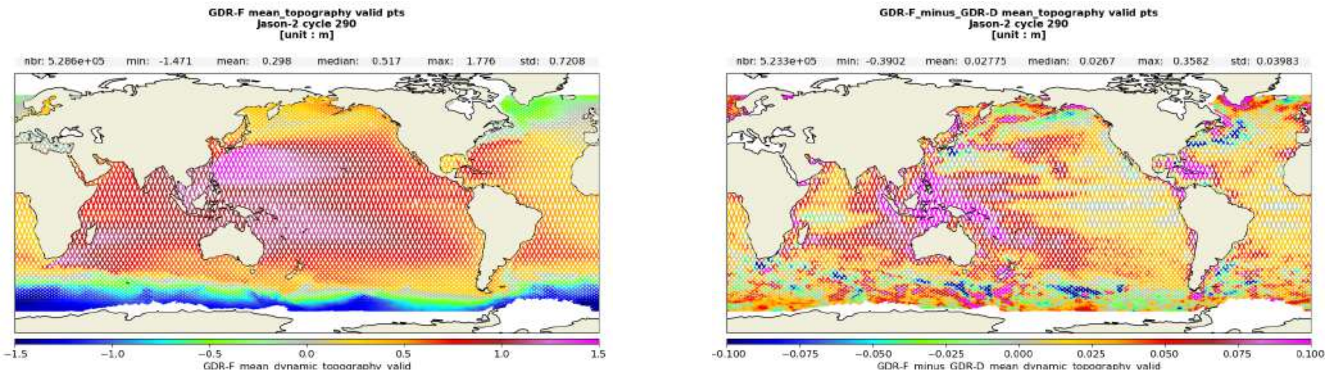

*Figure 42: mean_topography over 1 cycle (selection on SLA_MLE4 valid points only): GDR-F **(left)** and GDR-F minus GDR-D difference **(right)**.*

5.6.2. Geoid

Geoid variable has been updated from EGM96 to EGM2008. Difference between both solutions is about 29 cm in average over ocean (figure 43). Note that the change in reference ellipsoid (70 cm on global averaging) has been removed in difference when computing this analysis.

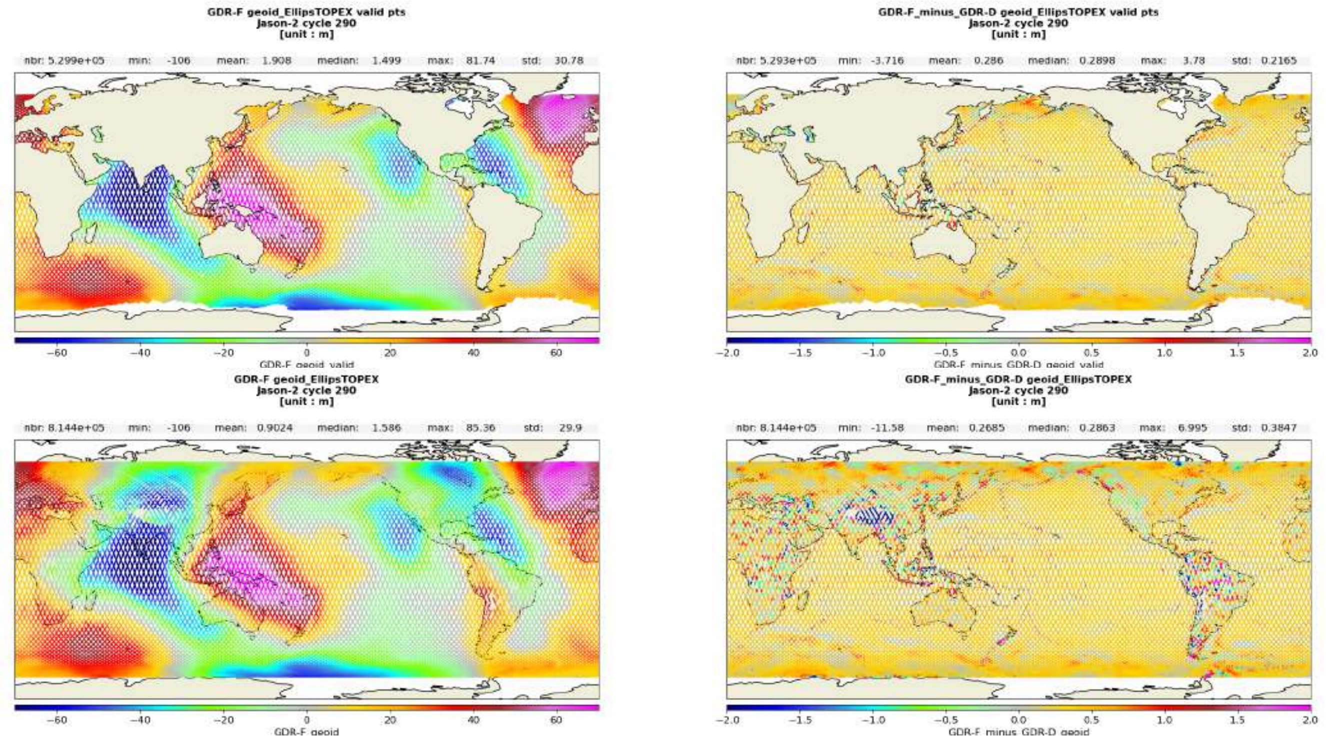

*Figure 43: geoid over 1 cycle (selection on SLA_MLE4 valid points only **(top)** or all along-track global monitoring **(bottom)**): GDR-F **(left)** and GDR-F minus GDR-D difference **(right)**.*

5.6.3. Bathymetry

The bathymetry (renamed variable depth_or_elevation in GDR-F) solution moved from DTM2000 to ACE2 model. There is a difference of -5.6 m in average (ocean valid point only) between both solutions with important geographical differences (figure 44).

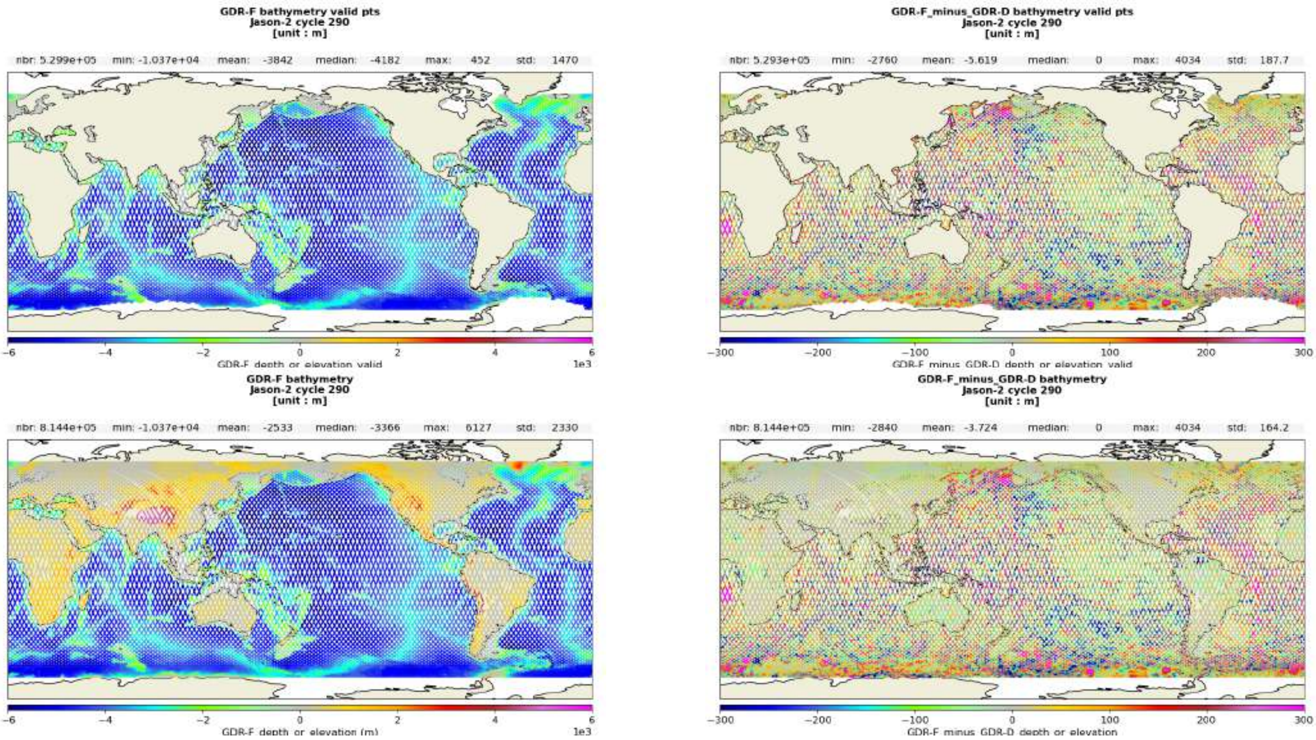

*Figure 44: bathymetry over 1 cycle (selection on SLA_MLE4 valid points only **(top)** or all along-track global monitoring **(bottom)**): GDR-F **(left)** and GDR-F minus GDR-D difference **(right)**.*

5.6.4. Surface type

Surface classification evolution is described in part “Data coverage”, see table 3 and figure 1.

5.6.5. Rain flag

GDR-D binary flag (0: no rain, 1: rain) is replaced by a 6-states flag in GDR-F.

	Previous classification (GDR-D)	New classification (GDR-F)
0	no rain	no rain
1	rain	rain
2	-	high rain probability from altimeter
3	-	high probability of no rain from altimeter
4	-	ambiguous situation possibility of ice
5	-	evaluation not possible

Table 9: Previous (GDR-D) and new (GDR-F) rain flag values

Over land, rain flag was set to 1 (corresponding to *rain*) in GDR-D whereas it is flagged to 5 (corresponding to *evaluation_not_possible*) in GDR-F as seen on figure 45.

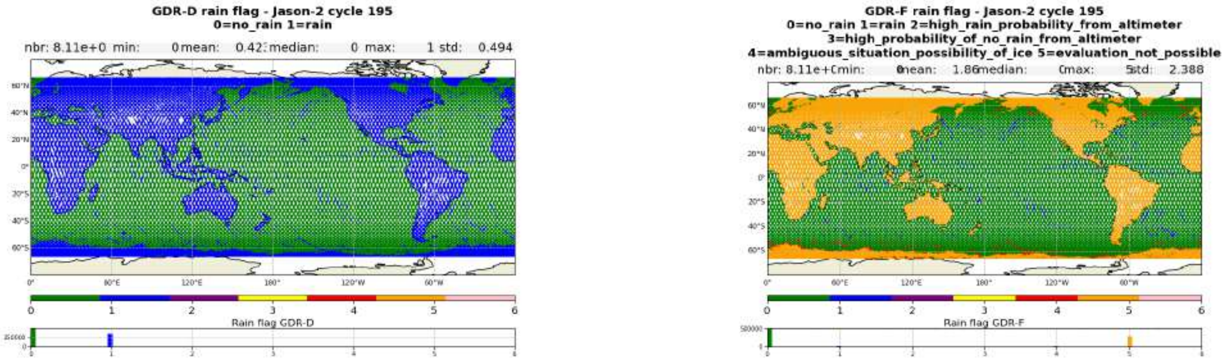

*Figure 45: Global rain flag for GDR-D (**left**) and GDR-F (**right**) over cycle 195.*

Over latitude higher than 50 °, each flagged measurement out of land is set to 4 (corresponding to *ambiguous situation possibility of ice*) for GDR-F solution (in red on right part of figure 46).

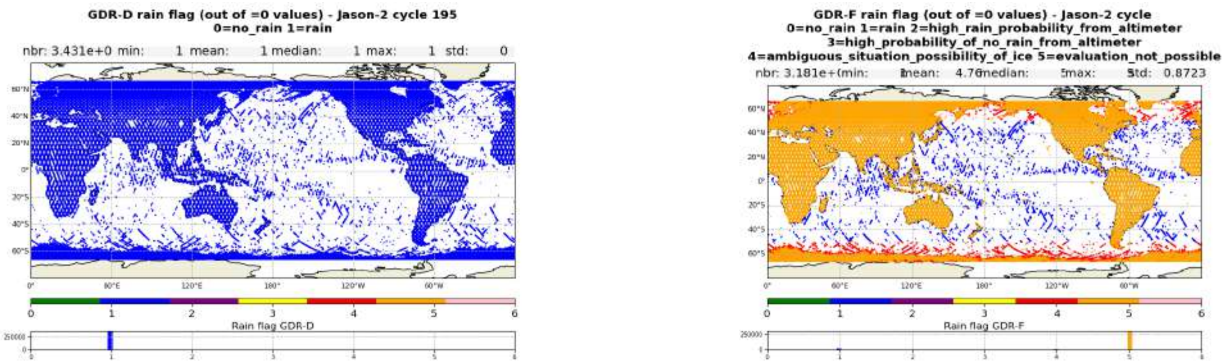

*Figure 46: Rain flag activated (= not set to 0) for GDR-D (**left**) and GDR-F (**right**) over cycle 195.*

In some cases, flagged to 1 (as rain measurements) on GDR-D data are set to *no rain* in GDR-F (green points on figure 47 showing the GDR-F rain flag values in case of GDR-D rain flag set to 1). This is particularly visible near coast (which is probably linked to the surface type evolution).

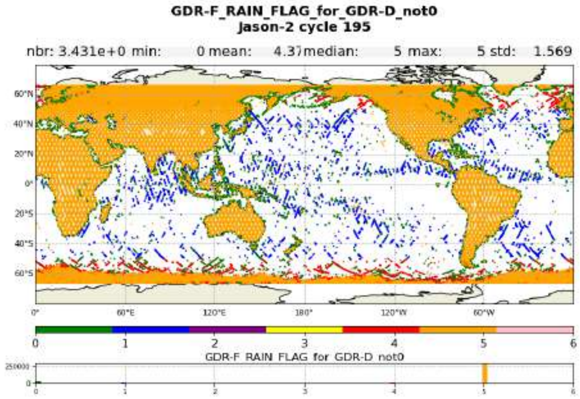

Figure 47: Rain flag for GDR-F when activated flag in GDR-D.

Finally, considering the valid measurements (after the process described in part 3.2.), there are significantly less measurements with rain flag activated in GDR-F than GDR-D (see figure 48).

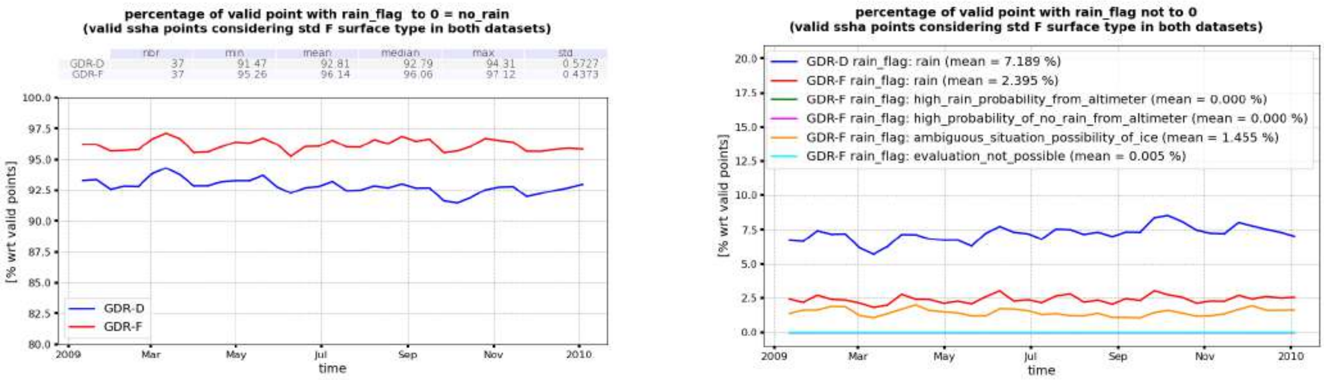

*Figure 48: Rain flag for GDR-D and GDR-F. Percentage of valid points with no rain (**left**) or with other values (**right**)*

6 Global and Regional Mean Sea Level long term monitoring

The global mean sea level is one of the most important indicators of climate change as it incorporates the reactions from several different components of the climate system. First, the analysis of the global surface height biases are detailed in this chapter. Then, the changes concerning the MSL trends are presented.

6.1. Sea Level Anomalies along-track analysis

The global bias is quite stable along the time (in black on figure 49) considering two periods before and after MSS solution changed in GDR-D (from CNES/CLS11 to CNES/CLS15).

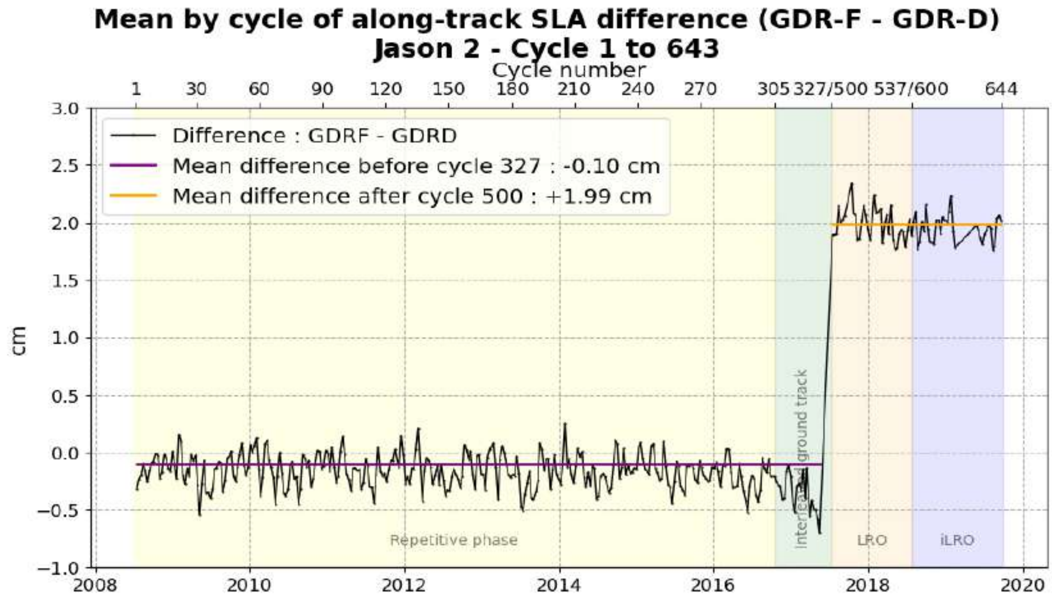

Figure 49: Cyclic mean of along-track SLA, without Caspian sea.

6.1.1. Global bias between Jason-2 GDR-F and GDR-D

The values on the table below is caluclated with gridded statictic on map over each whole period. A global bias of about -1 mm is visible in average for SSHA GDR-F minus GDR-D (see left of figure 52), each component contribution is detailed in table 10.

SLA parameter	GDR-D	GDR-F	Mean difference for valid points GDR-D minus GDR-F (except for orbit) until cycle 327	after cycle 500
Dynamical atmospheric correction Dry tropospheric correction Solid earth tide	No change from GDR-D to GDR-F		0 mm	0 mm
Internal tide	Not available	HRET8.1 (Zaron2019)	0 mm (in average)	0 mm (in average)
Pole tide	WAHR85 with MPL TOPEXlegacy	DESAI2015 with MPL2017	-0.2 mm	-0.2 mm
Ocean tide	GOT4.8	FES14b	-0.5 mm	0 mm
Wet tropospheric correction	Radiometer	Radiometer (new coefficients)	+7.1 mm	+4.1 mm
Ionospheric correction	Dual-frequency	Dual-frequency	-1.9 mm	-2.5 mm
Sea state bias	Non-parametric	Non-parametric	ku: +18.0 mm	ku: +18.0 mm
Range	Ku: MLE4	Ku: MLE4	ku: +0.1 mm	ku: +0.1 mm
Orbit	POE-D until cycle 245, POE-E cycle 245 onwards	POE-F	(GDR-F minus GDR-D) 0.8 mm	(GDR-F minus GDR-D) 0.2 mm
Mean sea surface	CNES/CLS11 until cycle 327, CNES/CLS15 cycle 500 onwards	CNES/CLS15	-24.0 mm	0 mm

Table 10: Contributions in sea surface height anomaly global bias between cycle 0 to 327 (repetitive and interleaved ground track phases) and between cycle 500 to 644 (LRO and iLRO phases)

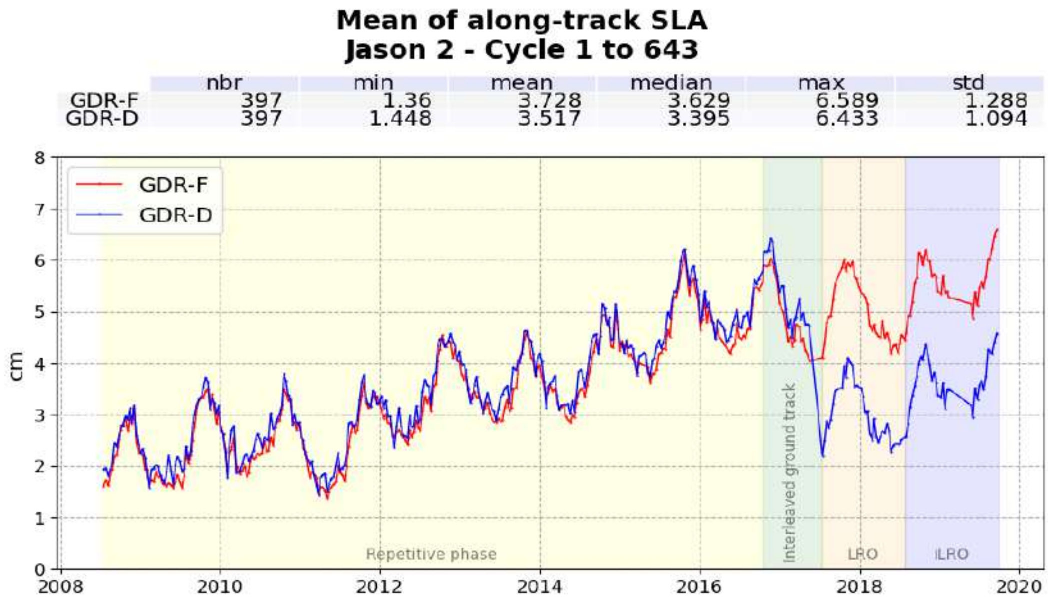

Figure 50: Cyclic mean of along-track SLA, without Caspian sea.

The periodogram of the SLA difference (figure 51) indicates 2 to 3 major peaks :

- near 90 days signal, linked to the use of the FES14B solution for ocean tide correction in GDR-F instead of GOT4.8 for GDR-D.
- at annual and semi annual signals.

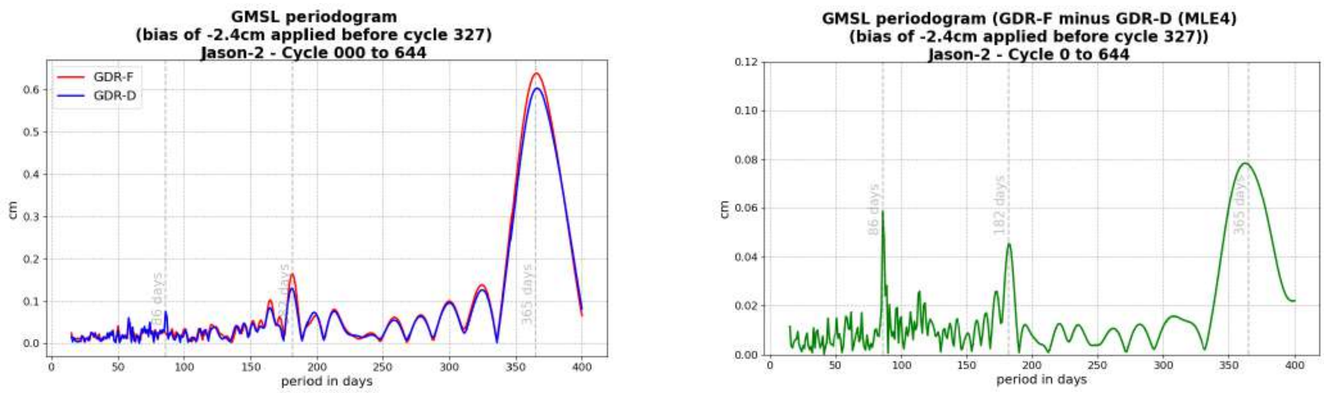

*Figure 51: Periodogram of GDR-D and GDR-F SLA (**left**) and difference (GDR-F - GDR-D)(**right**). Bias applied on GDR-D during reference and interleaved orbit phase correspond to MSS change (see part 5.5.4.).*

6.1.2. Regional biases between Jason-2 GDR-F and GDR-D

Regional patterns of several centimeters are visible on the difference between GDR-F and GDR-D sea level anomaly when averaging over the whole period (figure 52). These are mainly due to the change of mean sea surface from CNES/CLS11 (reference : 7 years) to CNES/CLS15 (reference : 20 years) over the repetitive phases, as shown on figure 52 and figure 53 (see also part 5.5.4.). The change in the period of reference directly contain the global bias of +2.4 cm due to mean sea level rise (as explained in [20] and [21]). SLA difference is strongly reduced (bottom on figure 53) over cycles 500-644 period as MSS are identical into GDR-D and GDR-F.

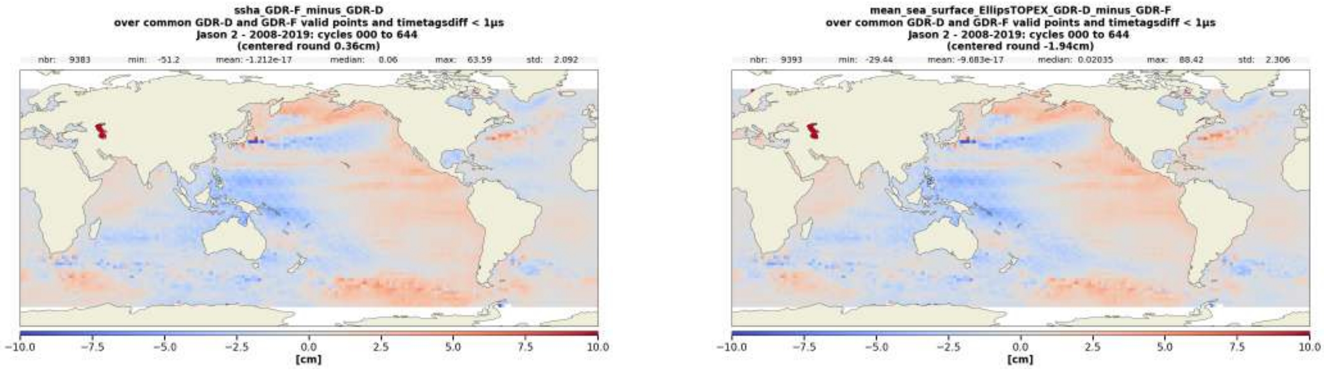

Figure 52: GDR-F minus GDR-D : Sea surface height anomaly (left) and mean sea surface (right) over the whole Jason-2 period (selection on valid points only)

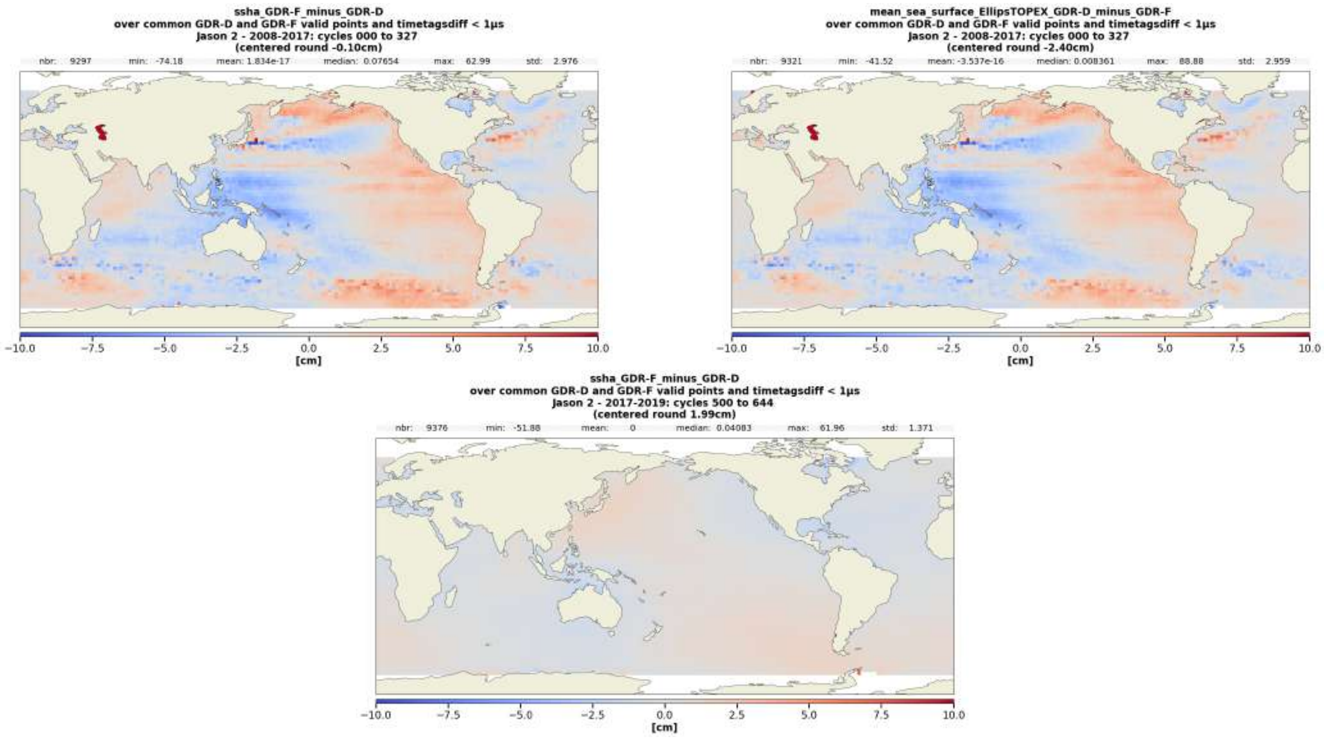

*Figure 53: GDR-F minus GDR-D : Sea surface height anomaly **(left)** and mean sea surface **(right)** over common valid points between cycle 0 to 327 **(top)** and between cycle 500 to 644 **(bottom)***

The regional contribution of orbit-range is lower than 1 cm (top left of figure 54). Once the patterns due to MSS are explained, the regional residual differences are mainly due to corrections applied to the range measurement (top right of figure 54). The involved corrections are SSB and pole tide (bottom figure 54).

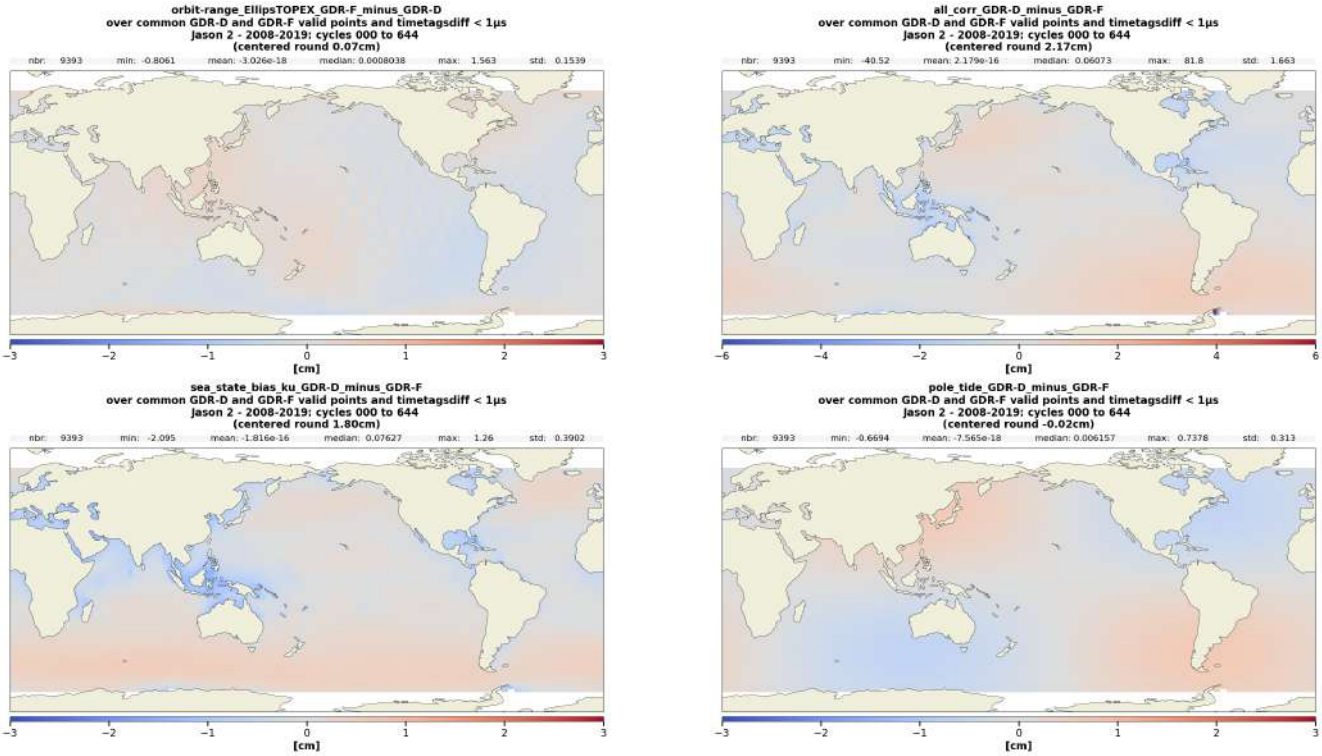

*Figure 54: GDR-F minus GDR-D : orbit minus range difference (**top left**) and GDR-D minus GDR-F : sum of range corrections differences (**top right**), sea state bias (**bottom left**) and pole tide (**bottom right**) contributions.*

6.1.3. Tandem phases analysis

6.1.3.1. Difference between Jason-3 and Jason-2

The Sea Level Anomalies (SLA) are computed along track with the SSH calculated as defined in previous sections 4.1.1. (for Jason-2) and 2.3. (for Jason-3). In order to take advantage of the Jason-3/Jason-2 tandem flight (cycle 281 to 303 for Jason-2), we performed direct SLA comparisons between both missions during this period. Colocated Jason-2 minus Jason-3 $orbit - range - mss$ and SLA differences averaged over the period of tandem phase are shown on figures 55, before (top) and after (bottom) reprocessing. The global bias between Jason-3 GDR-F and Jason-2 $orbit - range - mss$ evolves from 4.66 cm using Jason-2 GDR-D to 2.24 cm with Jason-2 GDR-F (linked to the 2.4 cm bias from mss differences). The bias between their corrected SLA is reduced from 3.37 cm (J2 GDR-D wrt J3 GDR-F) to 3.18 cm (J2 GDR-F wrt J3 GDR-F) in average. Considering GDR-F maps only, patterns are slightly different taking into account all range corrections compared to $orbit - range - mss$ but their amplitude are still under 1 cm (from bottom left to bottom right of figure 55). As both satellites measure the same oceanic features only 80" apart, only a weak hemispheric bias is visible when using the same MSS. Patterns for the top figures, comparing Jason3 GDR-F and Jason-2 GDR-D, where mainly due to MSS differences ([17]).

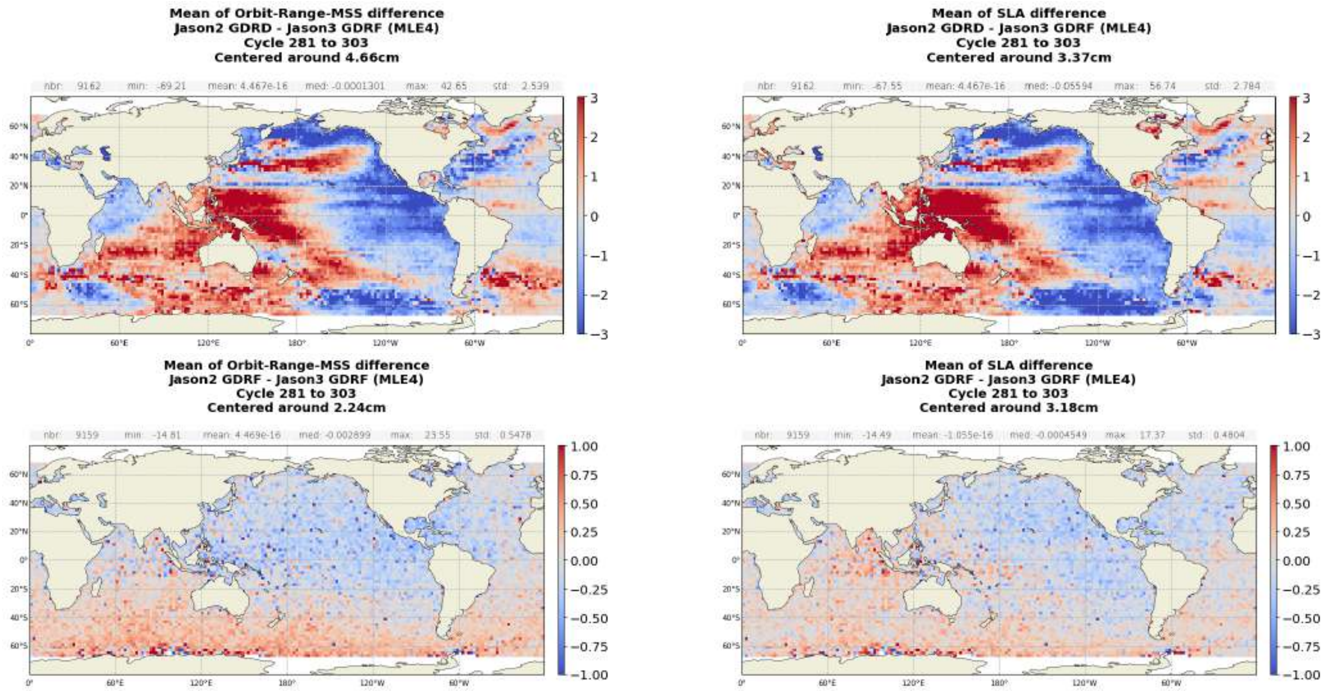

*Figure 55: Mean per cycle of Orbit-Range-MSS (**left**) and SLA (**right**) of residuals (= interpolated over theorical ground track) SLA along-track. Jason2 GDRD - Jason3 GDRF (**top**) and Jason2 GDRF - Jason3 GDRF **bottom**. **Caution: Different color range is used on this figure***

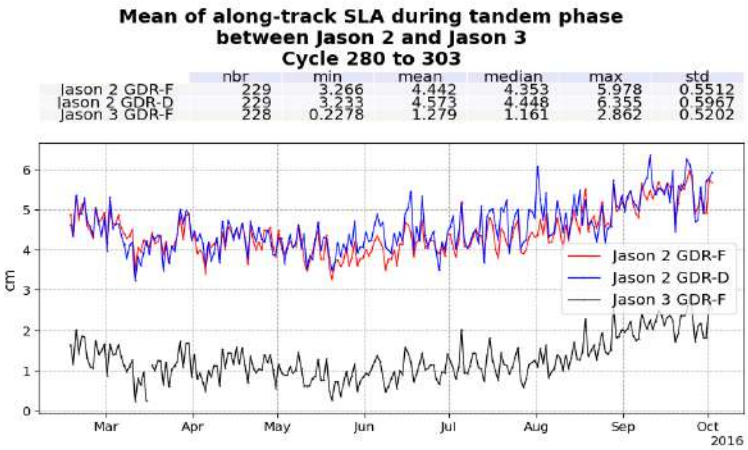

Figure 56: Daily mean of along-track SLA far Jason 2 (GDR-F and GDR-D) and Jason3 (GDR-F) during tandem phase

6.1.3.2. Difference between Jason-2 and Jason-1

The Sea Level Anomalies (SLA) are computed along track with the SSH calculated as defined in previous sections 4.1.1. (for Jason-2) and 2.4. (for Jason-1). *Note in particular that Jason-1 and Jason-2 L2P (DT21) include a composite / hybrid version for MSS (SCRIPPS, CNES/CLS15, DTU15).*
In order to take advantage of the Jason-1/Jason-2 tandem flight (cycle 001 to 020 for Jason-2), we performed direct SLA comparisons between both missions during this period. Colocated Jason-2 minus Jason-1 $orbit - range - mss$ and SLA differences averaged over the period of tandem phase are shown on figure 57 and figure 58, before and after reprocessing. About $orbit - range - mss$ differences (figure 57), MSS differences lead Jason-2 GDR-D to Jason-1 L2P SLA differences. When updating Jason-2 data to

L2P DT21 version, based on Jason-2 GDR-D but homogeneized with Jason-1 L2P geophysical corrections and MSS, a weak hemispheric bias is visible (bottom of figure 57). It is due to orbit differences, as both satellites measure the same oceanic features. Finally, using GDR-F version for Jason-2 mainly lead to a modification of global bias (from -0.84 cm to -0.92 cm) as their are limited impact on regional patterns from hybrid L2P and pure CNES/CLS2015 MSS.

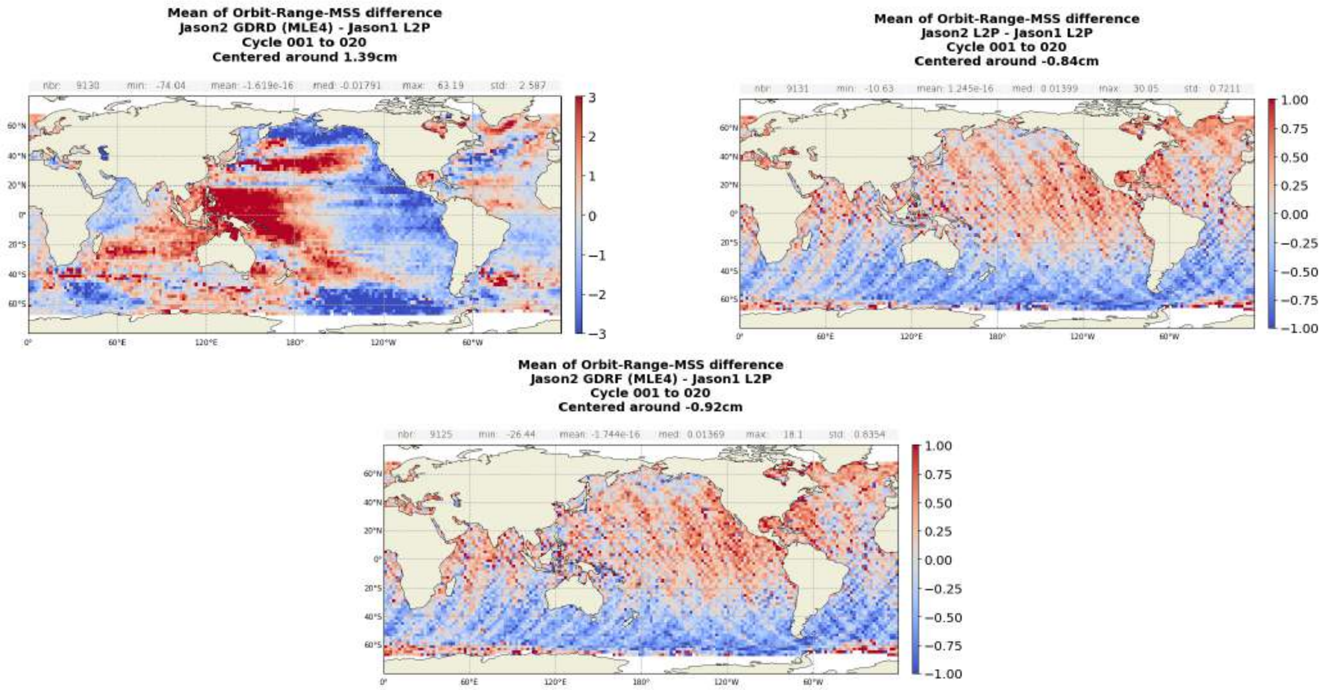

*Figure 57: Mean per cycle of (orbit - range -mss) residuals (= interpolated over theorical ground track). Jason2 GDRD - Jason1 L2P (**top left**), Jason2 L2P - Jason1 L2P (**top right**), and Jason2 GDRF - Jason1 L2P (**bottom**).*

Considering GDR-F maps (figure 58), MSS differences lead Jason-2 GDR-D to Jason-1 L2P SLA differences. Comparisons between Jason-1 and Jason-2 L2P show diffrent patterns taking into account all range corrections compared to $orbit - range - mss$ but their amplitude are still under 1 cm. SSB (part 5.4.6.) and wet tropospheric correction (part 5.3.2.) updates between L2P and GDR-F reprocessing for Jason-2 show increased global (18mm due to ssb and 7mm due to wtc) and regional patterns between Jason-1 and Jason-2 (bottom figure 58).

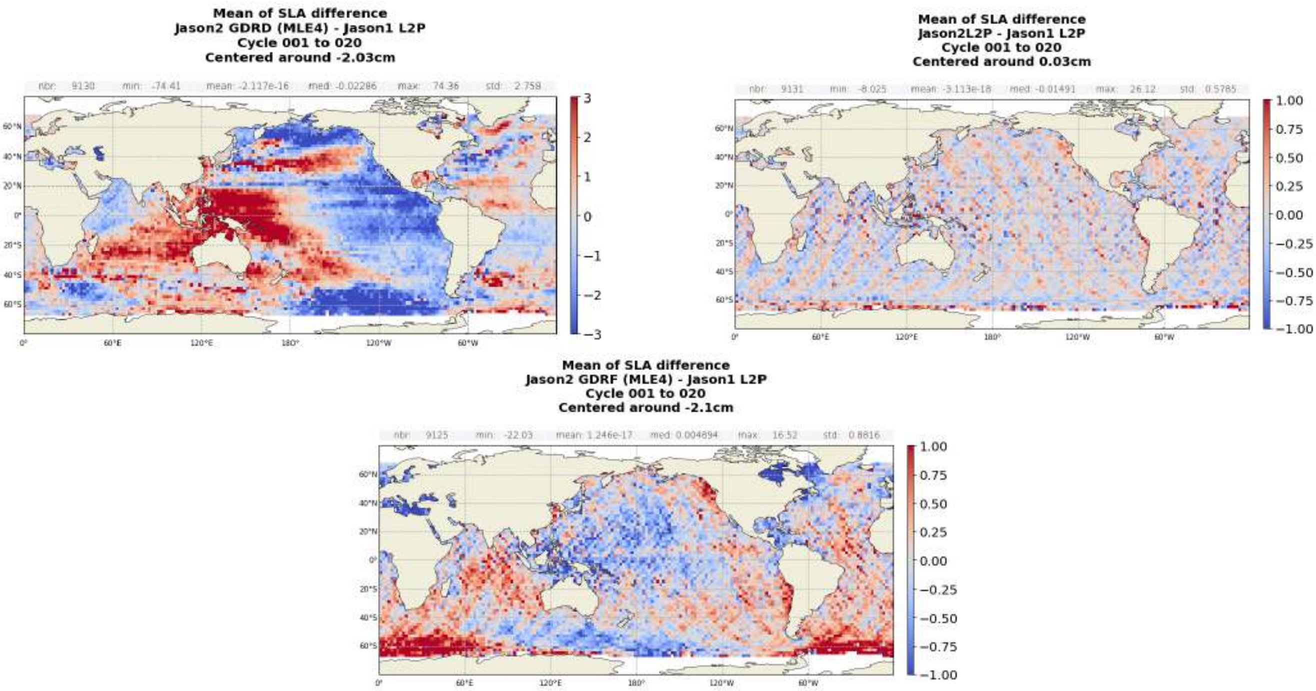

*Figure 58: Mean per cycle of corrected SLA residuals (= interpolated over theorical ground track). Jason2 GDRD - Jason1 L2P (**top left**), Jason2 L2P - Jason1 L2P (**top right**), and Jason2 GDRF - Jason1 L2P (**bottom**).*

6.2. Reprocessing impact on Global Mean Sea Level trends

The global mean level of the oceans is one of the most important indicators of climate change. Precise monitoring of changes in the mean level of the oceans, particularly through the use of altimetry satellites, is vitally important, for understanding not just the climate but also the socioeconomic consequences of any rise in sea level. The method to compute GMSL time serie and the altimeter standards used are described on [15]. GMSL analysis are done as described in aviso web site [17]. The method differs of what has been done for SLA along-track analysis (in part 6.1.) where all valid measurements are used with the same weight. GMSL is then a result of along-track SLA with a gridding process (reducing impact of representativity along latitude), filtering and removing annual and semi-annual signal. In this part, GMSL trends are computed over 2 different periods:

- repetitive and interleaved ground track phases
- LRO and iLRO phases

Here cyclic mean of along-track Sea Level Anomaly is monitored following the GMSL computing method described in [15], except that annual and semi-annual signals are note removed (what is called "raw GMSL on figure): as the real annual and semi-annual signals are supposed to be the same for GDR-D and GDR-F datasets, there are not removed before computing the differences here. It highlights a trend difference of 0.1 mm/year between GDR-D and GDR-F (figure 59) over the repetitive period.
This trend is mainly due to some jumps in GDR-F / GDR-D differences (see figure 61). First the change of orbit solution from POE-D to POE-E in GDR-D in may 2015 (cycle 254) induces a -0.66 mm jump in SLA estimations. A second jump happened at cycle 305, linked to the move to interleaved orbit : due to averaging effects on a differently covered global ocean from nominal to interleaved ground track, the mean sea surface differences between GDR-F and GDR-D lead to an additional -0.41mm jump. Finally, GDR-F versus GDR-D radiometer Wet Tropospheric Correction (presented on part 5.3.2.) differences lead again to some jumps, and in particular a -1.61mm one at 2017/01/01. As a consequence, the difference in GMSL trends from GDR-D to GDR-F is reduced to 0.01 mm/year between L2P and GDR-F as L2P21 orbit solution was homogeneized, and L2P21 mean sea surface solution was CNES/CLS15. Seasonal

signal are also significantly reduced between GDR-F minus L2P compared to GDR-F minus GDR-D as geophysical corrections had been already updated into L2P. The main jump that remains is the one linked to new GDR-F wet tropospheric correction.

Note that as L2P MSS solution is hybrid CNES/CLS2015, a near 2cm global bias remains when comparing to GDR-F, mainly due to sea state bias update.

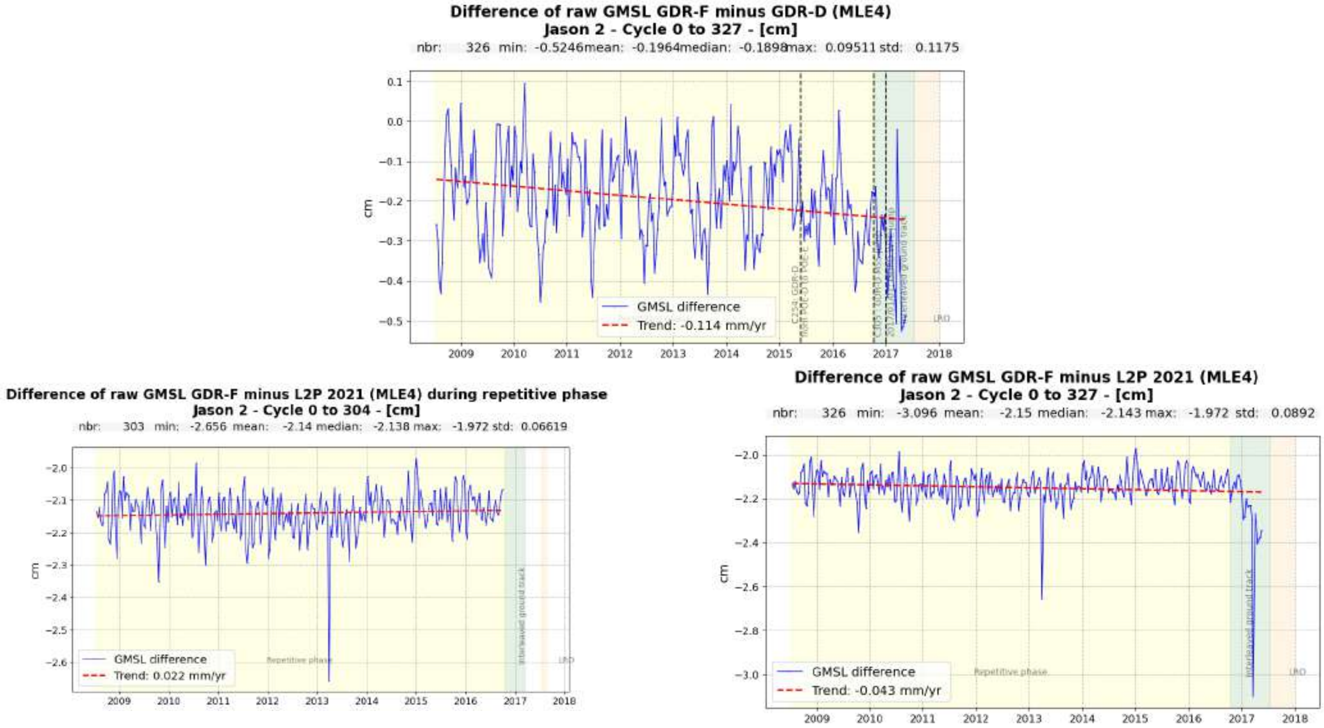

*Figure 59: Mean per cycle of GMSL difference GDR-F - GDR-D between cycle 0 to 327 **(top left)**. Mean per cycle of GMSL difference GDR-F - L2P during repetitive phase (**bottom left**) and during repetitive phase + interleaved ground track (**bottom right**)*

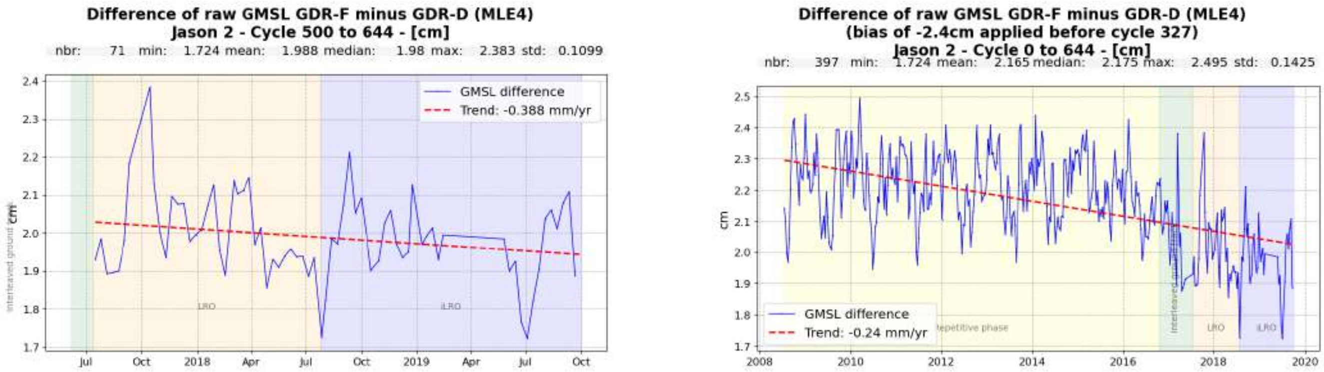

*Figure 60: Mean per cycle of GMSL difference GDR-F - GDR-D between cycle 500 to 644 **(left)** and on over the whole period (**right**)*

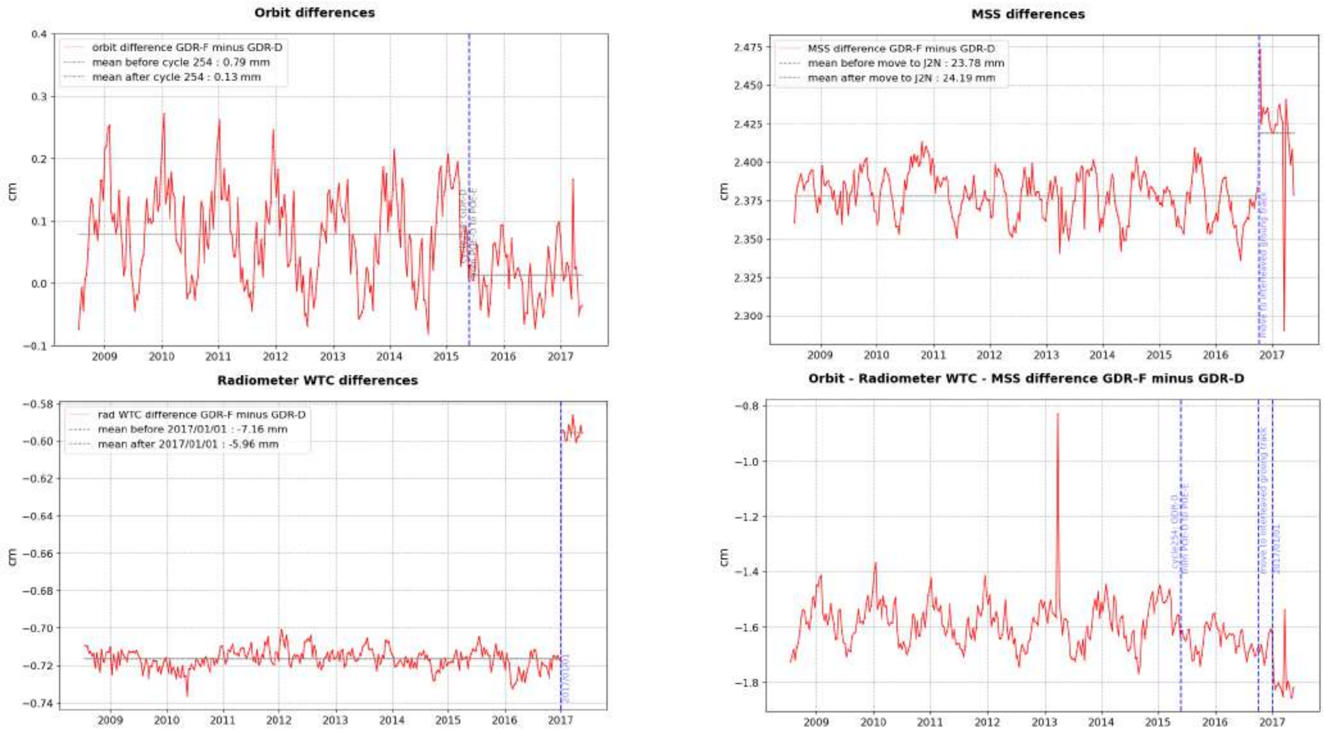

Figure 61: Mean per cycle of GMSL difference GDR-F - GDR-D jumps root cause over repetitive phases (nominal and interleaved). Bottom right : 3 cumulated biases

Geographical patterns can be observed on MSL difference between GDR-F and GDR-D (top of figure 62), specially in pacific ocean with an important East/West difference over the repetitive phase. Due to the short period of LRO and iLRO phases, differences are not significant on top right of figure 62 (there are shown here for information). The regional trends evolution between L2P and GDR-F shows a trend difference varying between -1 and +1 mm/year, particularly in antarctica ocean (bottom figure 62).

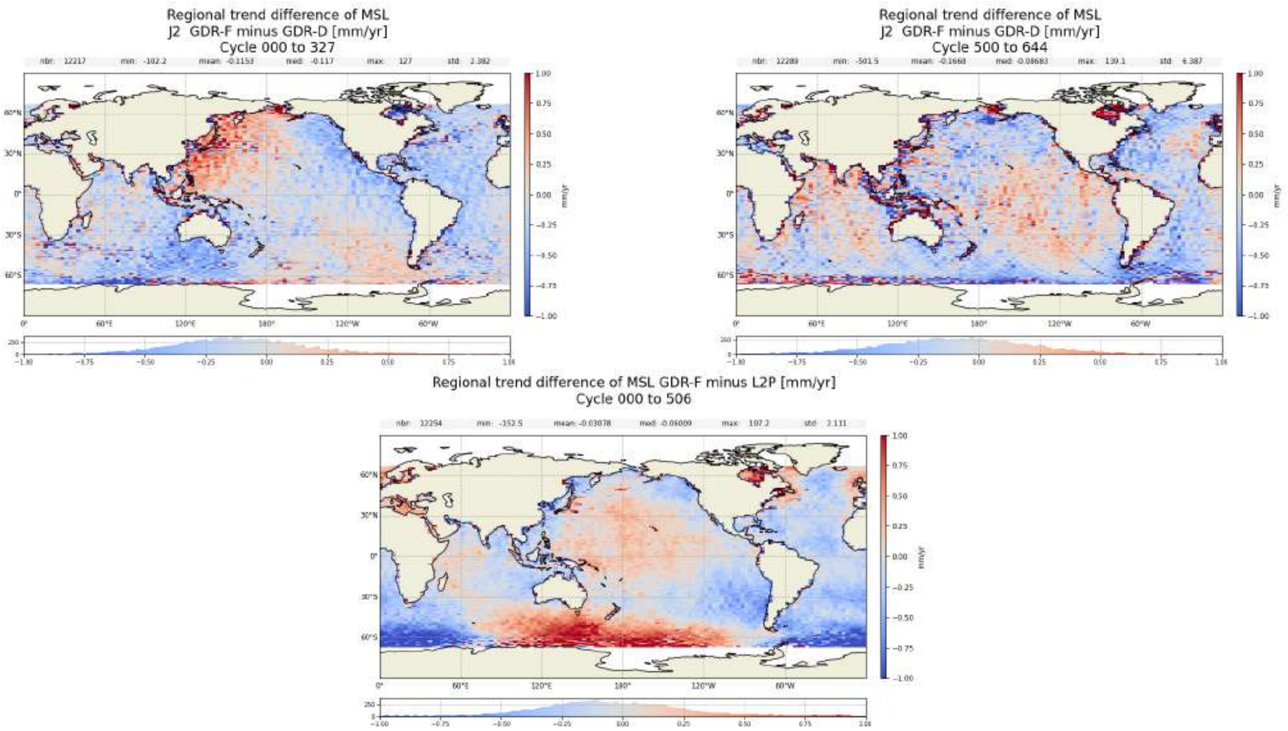

Figure 62: MSL trend difference GDR-F - GDR-D between cycle 0 to 327 ***(left)*** *and between cycle 500 to 644* ***(right)****. MSL trend difference GDR-F - L2P (****bottom****)*

7 Analysis of the new retracker solution : the Adaptive retracker

Jason-2 GDR-F product contain a retracking solution called “Adaptive retracking” in addition to the historical MLE3 and MLE4. The objective of this part is to provide an estimation of the Jason-2 Adaptive retracker available in GDR-F product quality by comparison with historical Jason-2 MLE4 retracker in terms of Sea Level Anomaly (SLA) evaluation and crossover performance. Adaptive retracking have 4 major evolutions :

- A parameter correlated to the mean square slope (describing the sea surface roughness) of the reflective surface has been introduced in the mathematical formulation of the backscattered energy
- The Adaptive algorithm directly accounts for the real in-flight Point Target Response of the instrument, by numerically convolving its discretized values to the analytical model of the backscattered energy. It makes the 1Hz Look Up Table correction unnecessary. All drifts or instabilities of the PTR are thus “natively” accounted for (without any approximation) in the Adaptive solution making this solution an excellent reference for evaluating and confirming the quality of the current GMSL estimation.
- A true Maximum Likelihood Estimation method (using the exact likelihood function) is used that accounts for the statistics of the speckle noise corrupting the radar echoes
- The algorithm adapts the width of the window on which the fitting procedure is performed in order to reject spurious reflections coming from off nadir directions, in particular when the satellite is approaching the coastlines

Benefits of Adaptive retracking solution for Jason and CFOSAT are described in many documents :

- IGARSS publication on the benefits for SLA, waves, wind (Jason3) [18],
- annex part of the CalVal at 1Hz activities annual report (using Jason-3 GDR-F preliminary 1 year of data) [14],
- benefits for retracking altimeter nadir echoes (CFOSAT) [19].

The analysis of this new retracker for Jason-3 is available in part 7 of [11].

7.1. Waveforms classification

A waveform classification has been done in order to adapt the retracking process to their shape (see figure 63). The list of classes defined for the Jason-2 waveform classification (the same as for Jason-3) is detailed in table 11. The method to defined this classification is detailed in “Jason-2 Products Handbook” [1]. The main class selected by classification neural network trained on shape features of the waveforms is available in the variable “wvf_main_class” of the GDR 1Hz product.

Waveform classification value	Waveform classification meaning
0	No wave
1	Brownian echoes, mainly found in open ocean
2	Peaky echoes, mainly encountered over narrow rivers, small lakes (smaller than the altimeter footprint) and water leads in sea ice regions
3	Several peaks, corresponds to multiple reflection in the footprint, encountered over land or heterogeneous areas
4	Strong peak with a very low trailing edge, corresponds to high reflective surfaces, often encountered on sea ice, most of the time over First Year Ice (FYI)
5	Brownian shape with a peak on the trailing edge, mainly found in coastal areas where the altimeter is close to the coast and a "bright point" is present in the footprint (but not at nadir)
6	Brownian shape with a peak on the leading edge or Brownian shape with a sharp trailing edge. Can be encountered over sea ice.
7	Brownian shape with a flat or increasing trailing edge. Can be found in rain cells or over land ice (it can also be a sign of a platform mispointing even if Jason-3 have good pointing performances).
8	Peaky echo shifted at the end of the analysis window, mainly found on hydrology and land
9	Trash echoes
10	Brownian shape with a high thermal noise level mainly found on land, land ice and sometimes on very heavy rain event
11	Double leading edge, can be encountered over land
12	Shifted Brownian, can be found over land ice and hydrology (big lake with a non-optimal tracker command)
13	Brownian shape with a noisy leading edge
15	Linear rise, can be found over land
18	Linear decrease, can be found over land

Table 11: Waveform classification definition

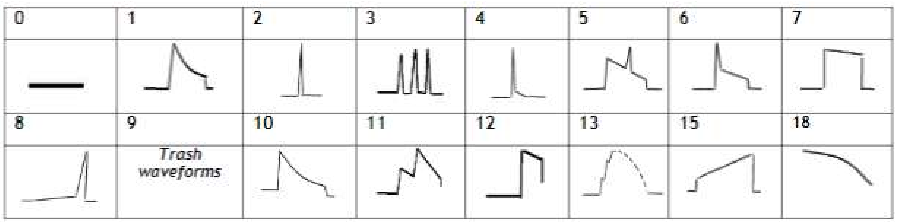

Figure 63: Waveform classification

7.2. Point to point validation process (editing)

The following results are obtained using the same validation point procedure for MLE4 and Adaptive outputs. Details on this procedure are available in part 3.2 of [14]. Note in particular that the same thresholds are used with both retrackers outputs, as described in handbook.
Adaptive data are globally more valid than with MLE4 data (figure 64), with **+1.17%** of additional valid data over ocean in average. The differences are mainly located in low SWH and rain areas (figure 65). Detailed sources of differences are available in Table 12. As adaptive model correlations between range/swh and sigma0 are different than in MLE4, sigma0 is less impacted by range/swh noise. This is visible on bottom right part of figure 67 as sigma0_rms from 20Hz elementary measurements used to compute the 1Hz data is significantly lower for adaptive than mle4, so that rejected on this variable thresholds criterion rate is reduced in Table 12.

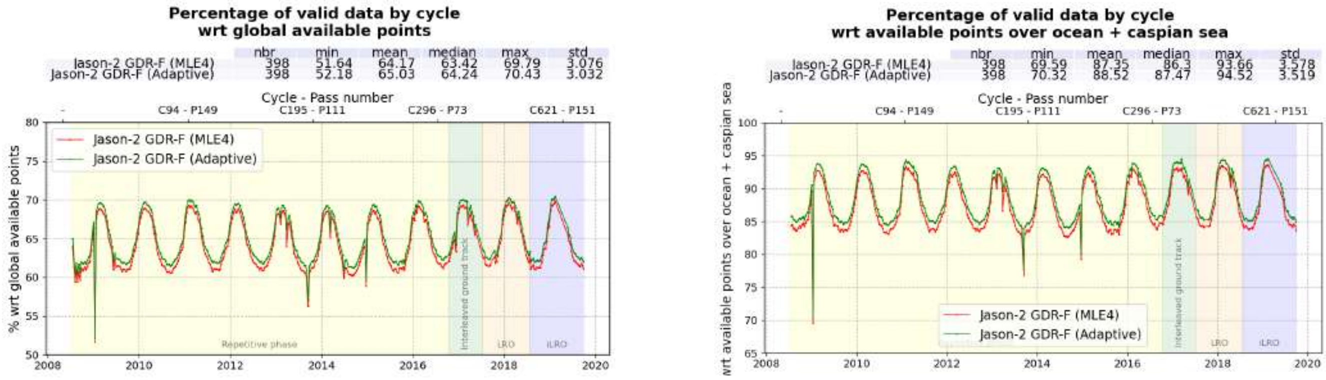

Figure 64: Pourcentage of valid point for GDR-F MLE4 and GDR-F Adaptive

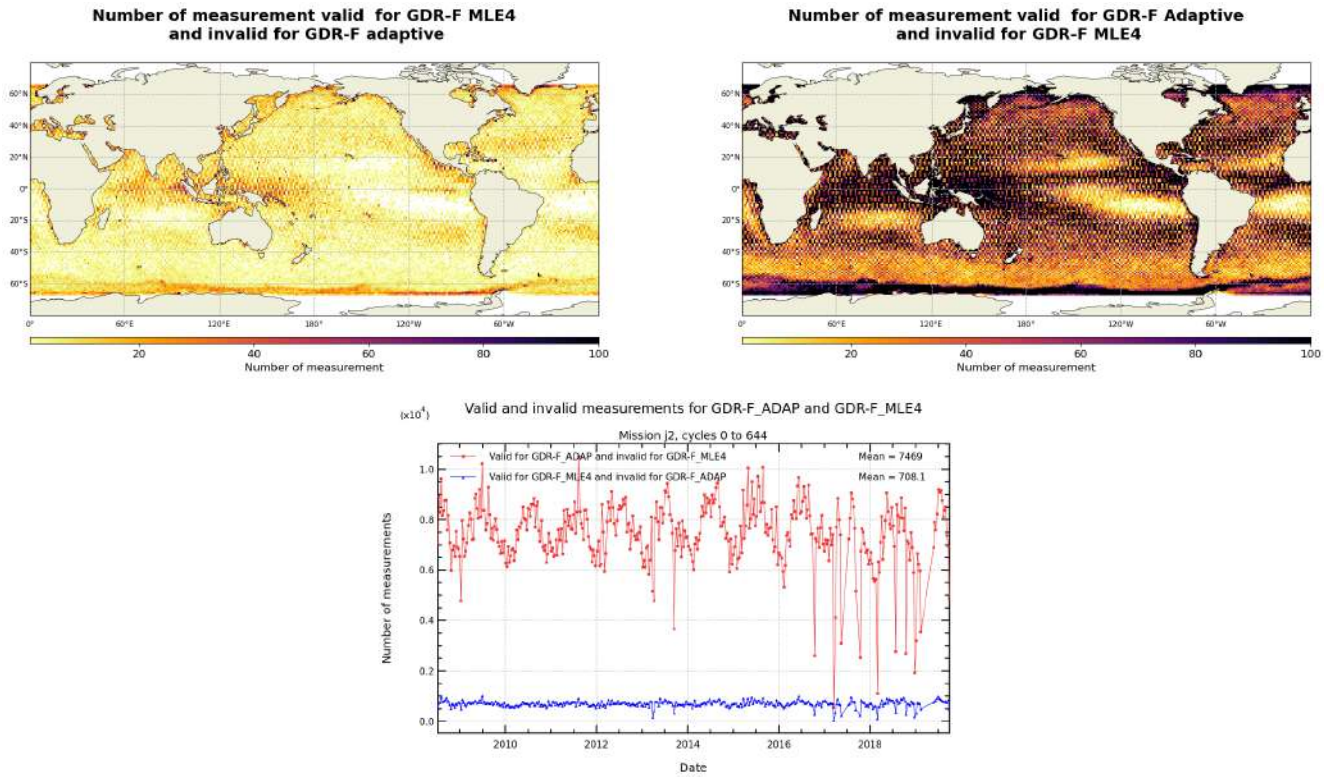

Figure 65: Number of measurements that are valid for GDR-F MLE4 and invalid for GDR-F Adaptive (top left, and bottom blue). Number of measurements that are invalid for GDR-F MLE4 and valid for GDR-F Adaptive (top right and bottom red)

Parameter	Threshold: min	Threshold: max	GDR-F MLE4	GDR-F Adaptive
swh	0	11m	0.71 %	0.09 % ↘
square off nadir angle	-0.2 deg^2	0.64deg^2	0.65 %	Same as MLE4
sea surface height (orbit - range)	-130 m	100 m	0.84 %	0.21 % ↘
range : number of 20Hz meas.	10	20	1.11 %	0.47 % ↘
range : std of 20Hz meas.	0	0.2 m	1.47 %	0.75 % ↘
sigma0	7 dB	30 dB	0.63 %	0.31 % ↘
sigma0 : number of 20Hz meas.	10	20	1.10 %	0.45 % ↘
sigma0 : std of 20Hz meas.	**0**	**1 dB**	**1.99 %**	**0.75 %** ↘
wind speed from altimeter	0	30 m/s	1.07 %	0.72 % ↘
sea state bias	-0.5 m	0	0.59 %	0.05 % ↘
ionospheric correction (filtered)	-0.4 m	0.4 m	0.95 %	0.74 % ↘
radiom. wet tropospheric corr.	-0.5 m	-0.001 m	0.22 %	Same as MLE4
sea level anomaly	-2 m	+2 m	1.58 %	1.02 % ↘
ocean tide (FES)	-5 m	5 m	$<$0.01 %	Same as MLE4
ocean tide (GOT)	-5 m	5 m	$<$0.01 %	Same as MLE4
cyclic mean number of edited points by thresholds (GDR-F: filtered iono)			17642	10748
percentage of rejected points by thresholds wrt non ice (ocean + caspian sea)			3.38 %	2.07% ↘

Table 12: Thresholds editing rates MLE4 vs Adaptive, from 2008 to 2019 (cycles 001 to 644)

Please note some differences between Jason-3 GDR-F Adaptive and Jason-2 GDR-F Adaptive:

- First about the high SWH estimations process. Due to the initial choice of classe 13 processing, a saturating effect was observed in waves higher than 10.5m for Jason-3 adaptive during the GDR-F reprocessing period. A change in classe 13 retracking method (now considered as 'ocean') was applied during this Jason-2 data reprocessing, and for Jason-3 operational production since cycle 210 (L2 library v6.8). The impact is illustrated in left part of figure 66 as there are now more available valid adaptive swh between 10 and 12 meters.
- The second change impacts the process of points near coast. This evolution applied to Jason-3 since cycle 318 is available on the whole Jason-2 period. As a consequence, there is more valid point for Jason-2 between 0 and 30km to coastal distance than Jason-3 (until this evolution had been applied to Jason-3 operational production). This difference is visible on right part of figure 66.

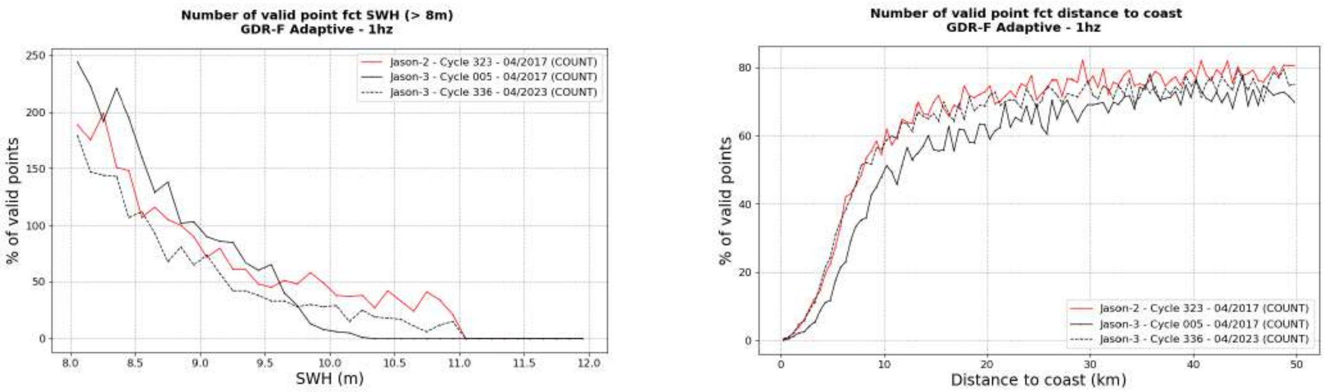

*Figure 66: Number of SSHA valid point for GDR-F MLE4 and GDR-F Adaptive wrt high SWH (**left**) and distance to coast (**right**)*

7.3. Focus on altimeter parameters

The metric presented here qualify the Adaptive retracking using 1Hz data. The rms of the 20 elementary measurements used to compute the 1Hz range is higher for MLE4 solution than with Adaptive (bottom left part of figure 67). Same results for the rms of the Sigma0 20 elementary measurements (bottom right part of figure 67). This reduction is coherent with SLA spectrum shown on figure 68. The difference in range evaluation between the two solutions is linked to the SWH estimations (see top part of figure 67), these differences are included into ssb corrections.

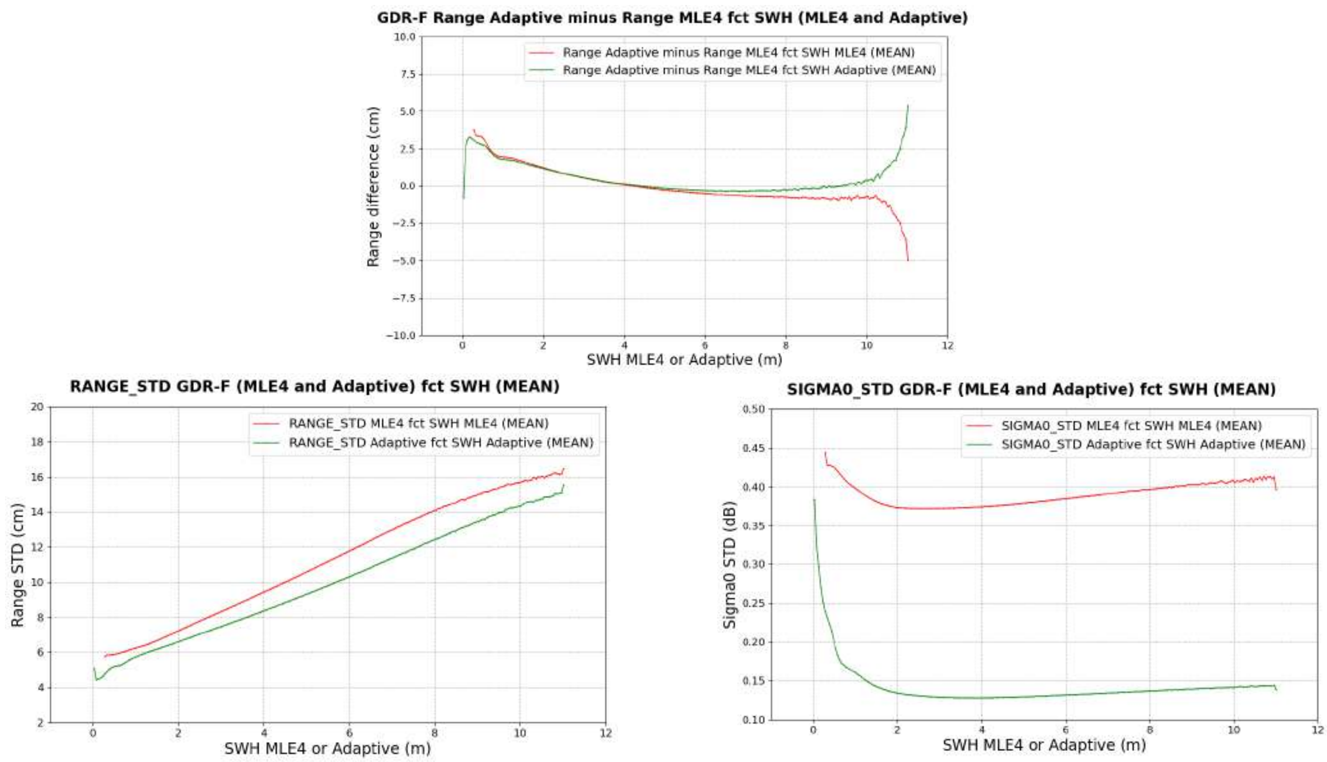

*Figure 67: Difference between range Adaptive fct swh Adaptive and range MLE4 fct swh MLE4 **top**. Standard deviation of range **bottom left** and sigma0 **bottom right** fonction of SWH for **MLE4** and **Adaptive***

A reduction of about 12% of the range noise level is observed with the adaptive solution, mainly thanks to the use of an exact MLE criterion in the estimation procedure (see figure 68). Taking into account the SSB correction applied to range measurements reduces the level energy. In particular, by recomputing at 20 Hz sea state bias ('SSB updated' curves on bottom figure 68) reduce the spectral bump compared to use a copied from 1Hz (only available solution in GDR-F) solution.

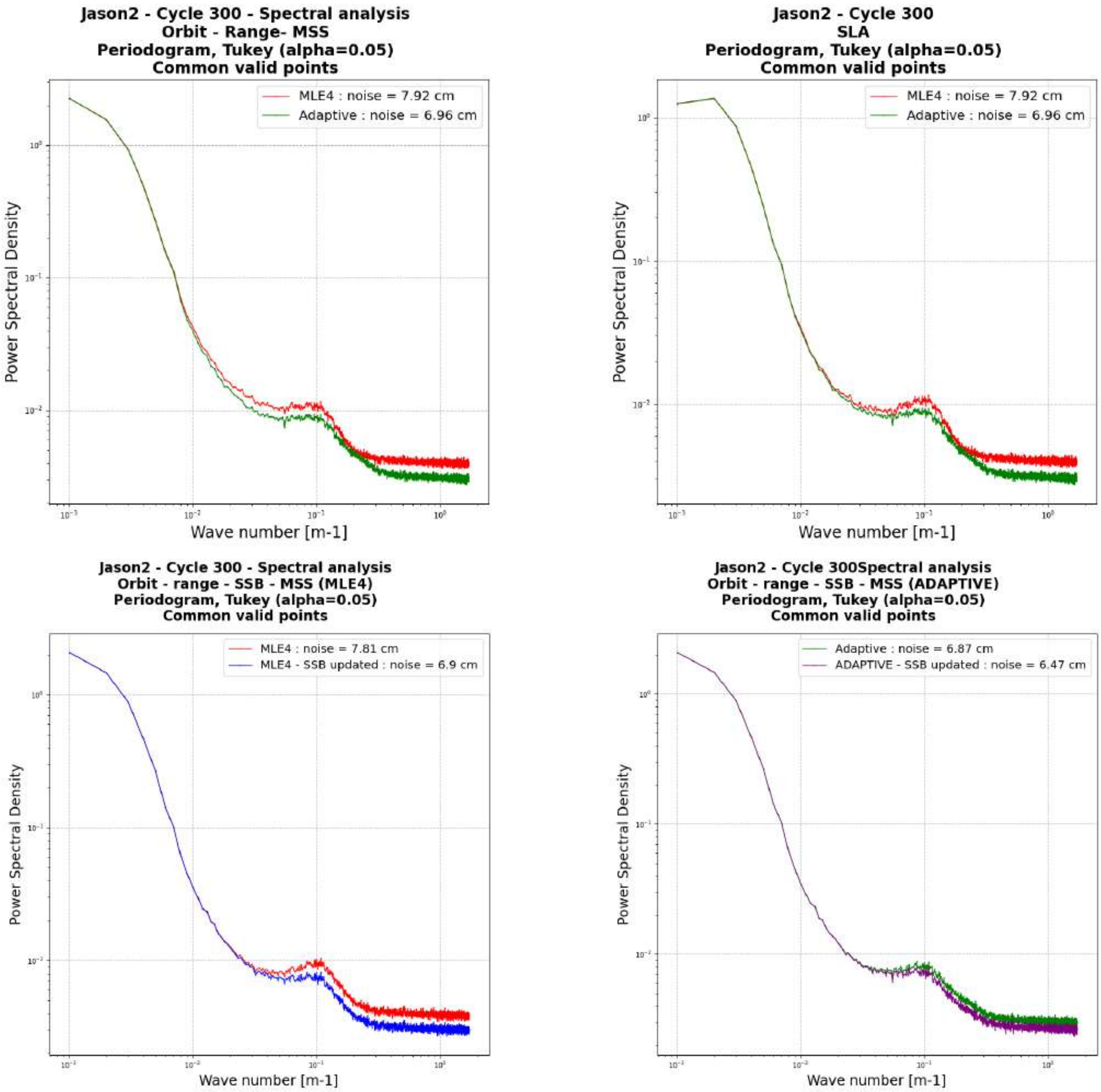

Figure 68: SLA spectrum 20hz for cycle 300 - Jason 2

Over the common valid points datasets, Adaptive and MLE4 SWH are different by about 4.6 cm in average, these differences are swh dependant (top left of figure 69). Note that as there is no LUT applied on Adaptive retracking outputs, there is no peak at 25 cm swh for green curve compared to red curve on top right of figure 69.

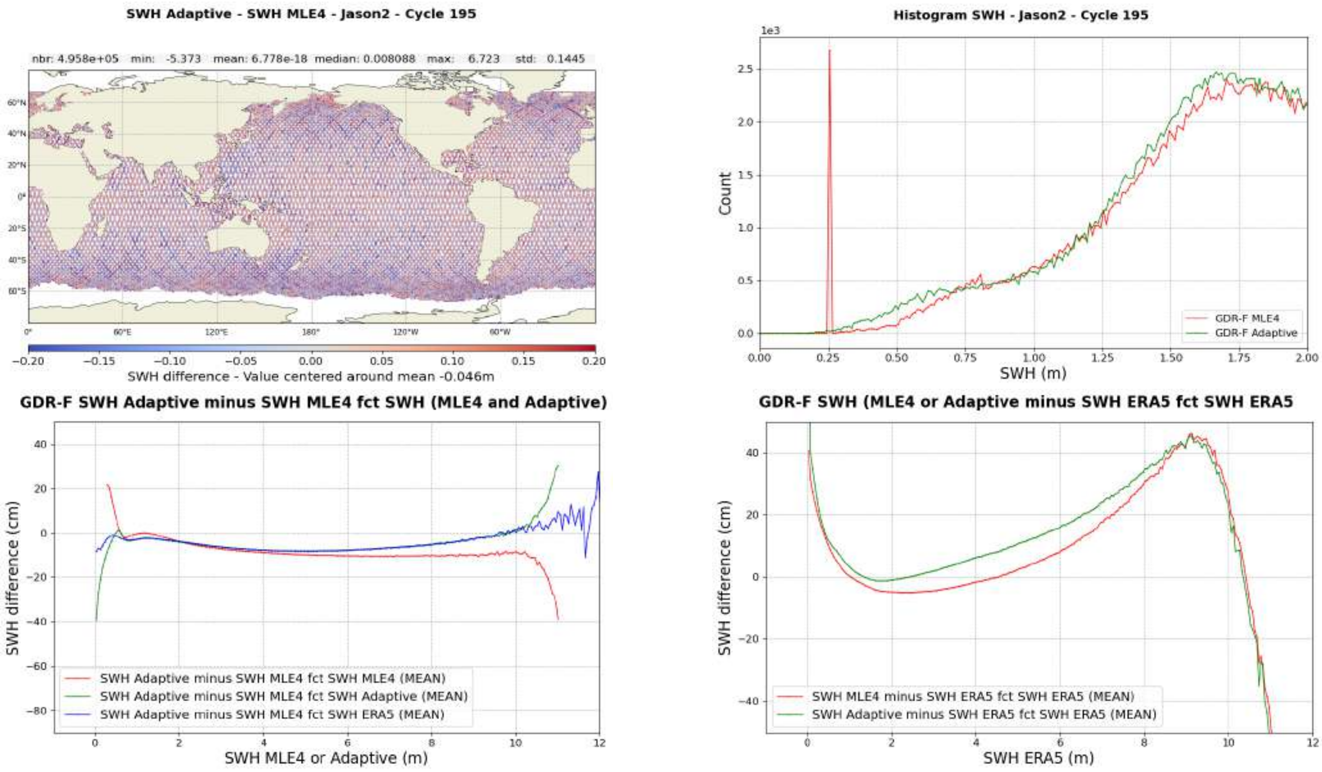

*Figure 69: Histogram (**top left**) of SWH for GDR-F MLE4 and GDR-F Adaptive retracking and Adaptive minus MLE4 SWH difference (**top right**) over cycle 195. SWH differences wrt altimeter or ERA5 model over the whole period (**bottom**)*

7.4. Performances

7.4.1. Performances at crossovers

SSH crossover differences are the main tool to estimate the whole altimetry system performances. They allow to analyze the SSH consistency between ascending and descending passes: it should not be significantly different from zero. More importantly, special care is given to the geographical homogeneity of the mean difference at crossovers. However in order to reduce the impact of oceanic variability, we select crossovers with a maximum time lag of 10 days. Mean and standard deviation of SSH crossover differences are computed from the valid dataset to perform maps or a cycle by cycle monitoring over all the altimeter period. In order to monitor the performances over stable surfaces, additional editing is applied to remove shallow waters (bathymetry above -1000m), areas of high ocean variability (variability above 20 cm rms) and high latitudes ($> |50| deg$). SSH performances are then always estimated with equivalent conditions.

The performed comparisons between SSH with MLE4 and Adaptive outputs show no global neither regional impact on mean of SSH difference at crossovers (figure 70). Global variance of SSH difference at crossovers is reduced by **0.54cm^2** in average with Adaptive retracker compared to MLE4 (left of figure 71). Geographic reduction (right of figure 71, in blue) of variance of SSH difference at crossovers shows no geographically correlated pattern. *Note that only points that are valid with both solutions are used to compute this analysis.*

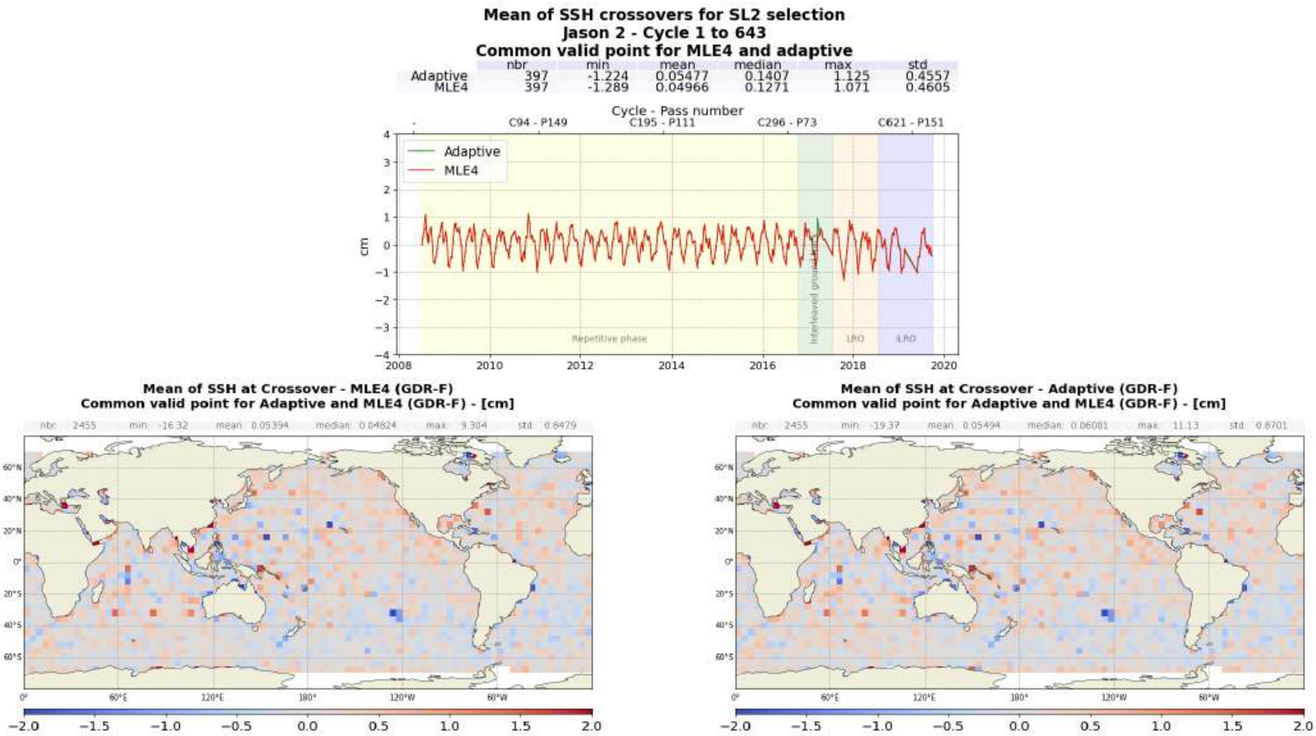

*Figure 70: Mean of SSH difference at crossover points (selection on common valid points, $|latitude| < 50$, oceanic variability $<$ 20cm and bathymetry $<$ -1000m): cyclic monitoring (**top**), and map averaging (**bottom**) for GDR-D (**left**) or GDR-F (**right**).*

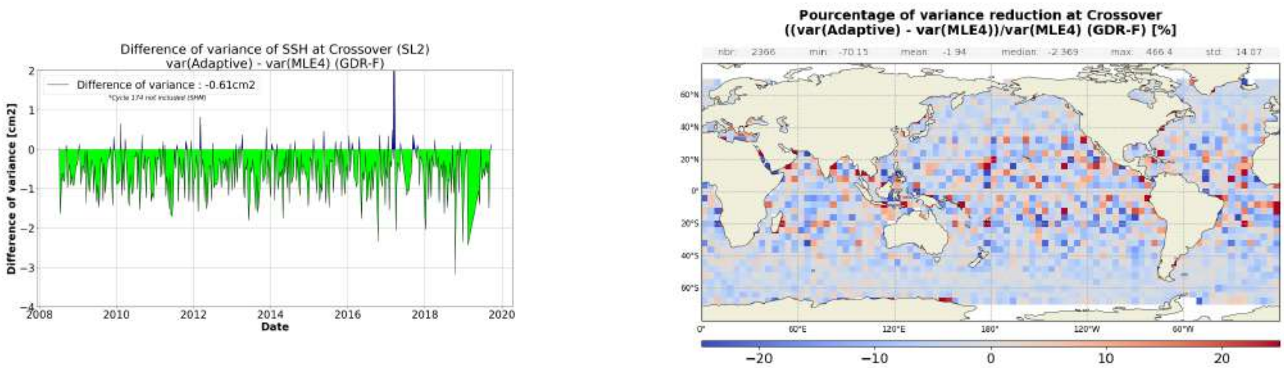

*Figure 71: Difference of SSH at crossover points : Variance difference (**left**) (selection on common valid points, $|latitude| < 50$, oceanic variability $<$ 20cm and bathymetry $<$ -1000m), pourcentage of error reduction without geographic selection (**right**)*

7.4.2. Performances of along-track SLA

The Sea Level Anomalies (SLA) are computed along track from the substraction of the mean sea surface to the SSH: SLA = SSH $-$ MSS. SLA analysis is a complementary indicator to estimate the altimetry system performances. It allows to study the evolution of SLA mean (detection of jump, abnormal trend or geographical correlated biases), and in particular the evolution of the SLA variance highlighting the long-term stability of the altimetry system performances .

Figure 72 present along-track SLA variance difference between GDR-F Adaptive and GDR-F MLE4. Variance is lower for GDR-F Adaptive than GDR-F MLE4 by **0.49cm^2**. There are better results near coasts (top right of figure 72). Opposite results was observed for Jason-3 (see part 7.4 in [11]). It is probably due to an evolution that has been implemented in Jason-3 from cycle 210 onwards and is available for the whole Jason-2 data series.

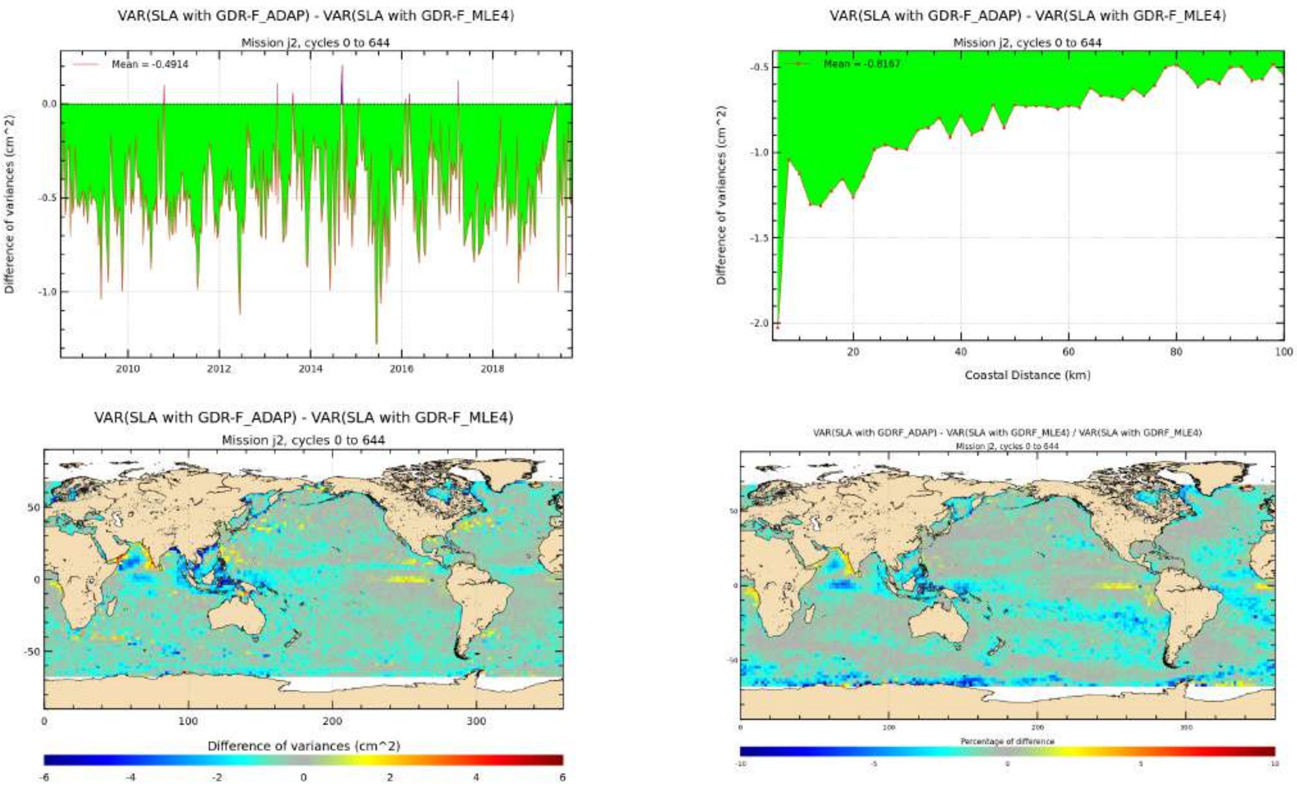

*Figure 72: Along track SLA variance difference between GDR-F Adaptive and GDR-F MLE4 (caspian sea not included). Cyclic monitoring (**top left**), in function of distance to coast (**top right**). Map of absolute difference of variance (**bottom left**) and percentage relative to MLE4 level of variance (**bottom right**)*

7.5. SLA and GMSL

There is a global bias of **-2.2 cm** from MLE4 SLA to Adaptive SLA, slightly correlated to SWH patterns in average (right of figure 73).

Geographical patterns can be observed on MSL trend difference between MLE4 and Adaptive. The cyclic mean of along-track Sea Level Anomaly differences is monitored and highlights a trend difference of 0.1 mm/year (figure 74). This estimation has to be considered with care as some jumps are observed on LRO and iLRO phase (right of figure 73). In most of cases, these can be linked to PTR evolution (figure 75), in particular fro important jumps that can occur at instrument reset. However, some other jumps on PTR are observed with no impact on SLA (for exemple on cycles 143 and 193). This has to be further investigated to a better understanding of this behaviour.

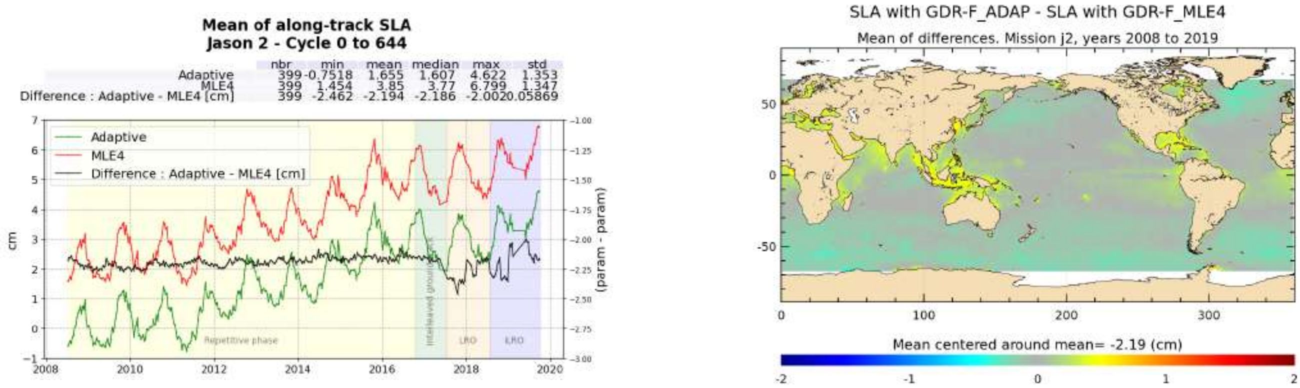

Figure 73: Difference of cyclic mean of Sea Level Anomaly (GDR-F Adaptive - GDR-F MLE4)

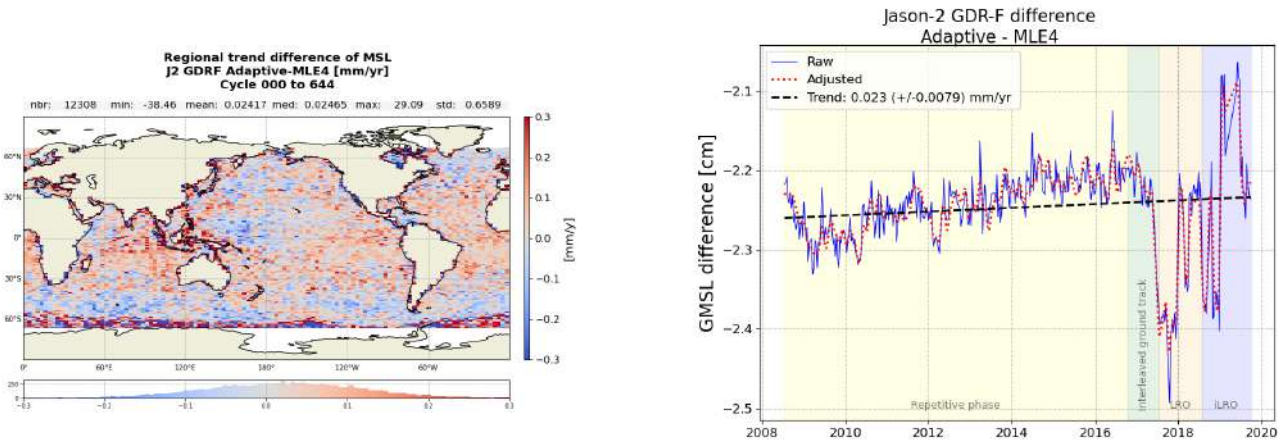

*Figure 74: MSL trend difference Adaptive-MLE4 (**left**) and mean per cycle of GMSL difference Adaptive-MLE4 (**right**)*

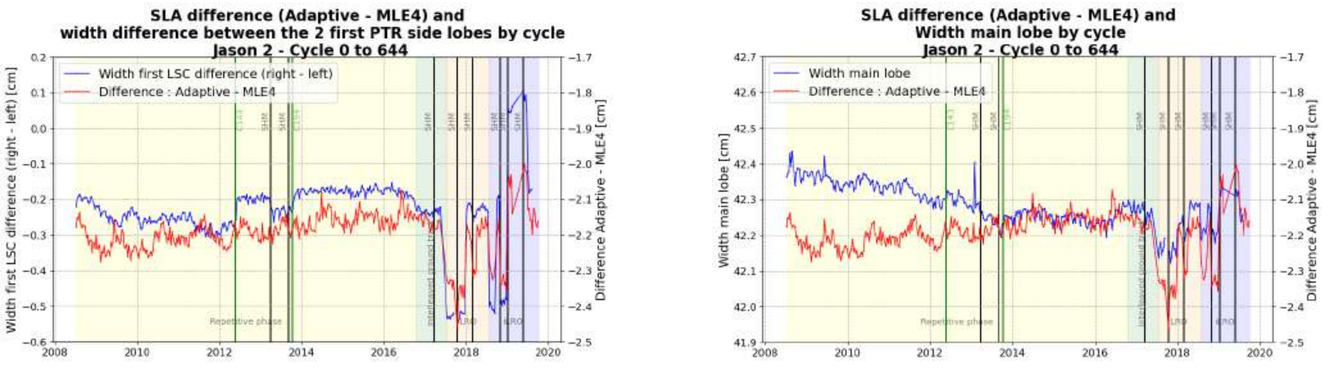

*Figure 75: SLA difference Adaptive-MLE4 compared with the difference between the 2 fisrt PTR side lobes (PTR) on **left**) and with width main lobe on (**right**)*

8 Analysis of the new sea state bias solution : add of mean wave period information

Jason-2 GDR-F includes new alternative solutions for sea state bias corrections. These solutions use an additional parameter as input: the mean wave period (available into GDR product as *mean_wave_period_t02*). These new sea state bias corrections (*sea_state_bias_3d_mp2* and *sea_state_bias_adaptive_3d_mp2*) were fitted on one year of preliminary Jason-3 GDR-F data and reused for Jason-2 GDR-F (it will be named in this analysis *SSB_3d* in opposition the the reference *SSB* described in part 5.4.6.). For more details on *SSB_3d*, see [27]. This part studies the differences and impact on system performances between the reference SSB and this new solution for MLE4 and Adaptive sea level anomalies.

8.1. Mean wave period and direction

MFWAM is a forcasting model of sea state (wind sea and swell). Mean wave direction gives average direction (degrees) of sea surface wave where they come from. Mean wave period gives the average periodicity (seconds) of sea surface wave, and so help to better consider the sea surface conditions. For Jason-2 GDR-F reprocessing, the MFWAM **WAVERYS** version is used.

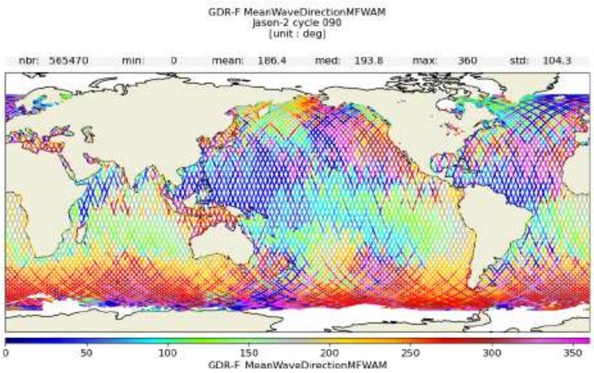

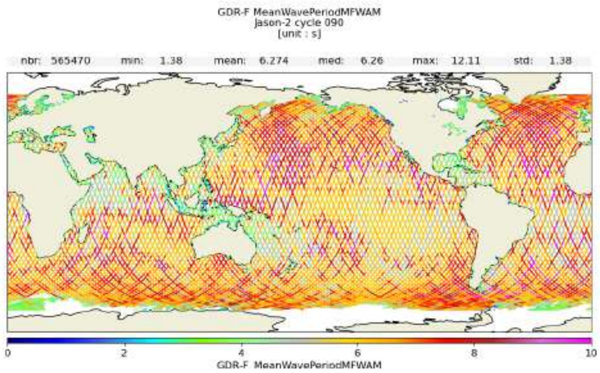

*Figure 76: Mean wave direction **left** and period **right** for one Jason-2 GDR-F cycle*

8.2. Results on MLE4 retracking

The same editing procedure is applied to Sea Level Anomaly replacing the reference sea state bias with the new solution. All points that are valid (meaning within thresholds) for SSB all also valid using SSB_3d (red curve at left of figure 77). On contrary, 5040 points per cycle in average are valid with SSB but invalid with SSB_3d in average (blue curve), mainly at high latitudes (see figure 77), this is directly linked to the mean wave period unavailabiliy at high latitudes.

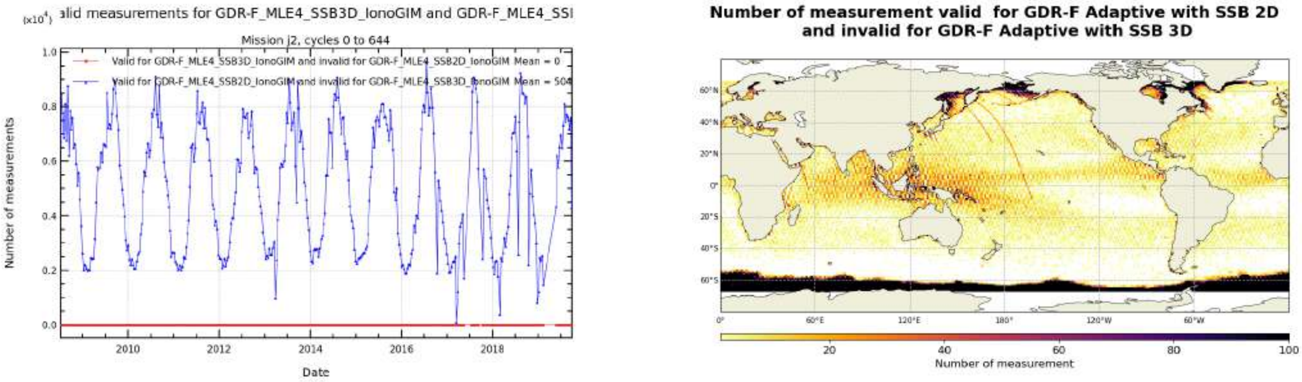

Figure 77: Difference of editing point between SSB and SSB 3D (MLE4 retracking)

No significant impact is observed on mean difference of SSH at crossover between both solutions (figure 78). A variance reduction of about 1.6 cm^2 is measured with the 3d solution compared to the reference (figure 79).

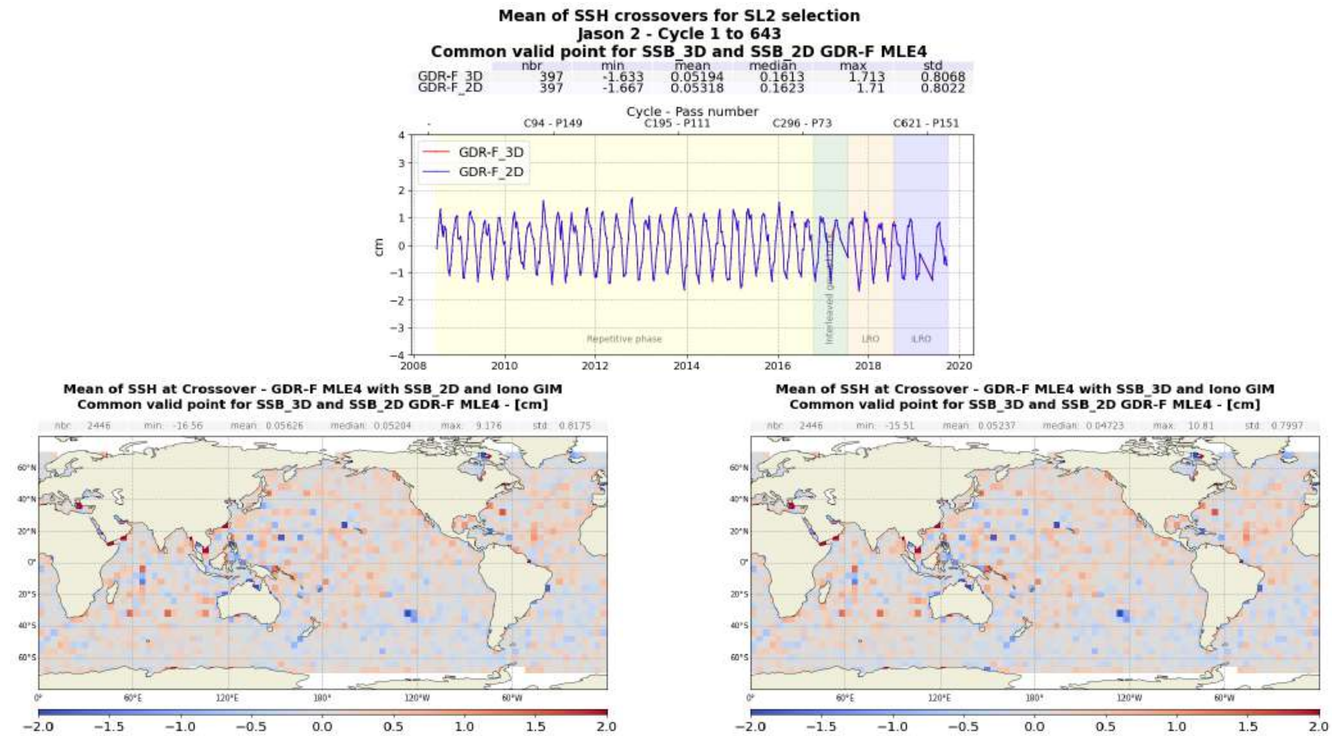

Figure 78: SSH difference at crossover for SSB_3d and SSB (with iono GIM). Note that figures are computed over a common valid points dataset.

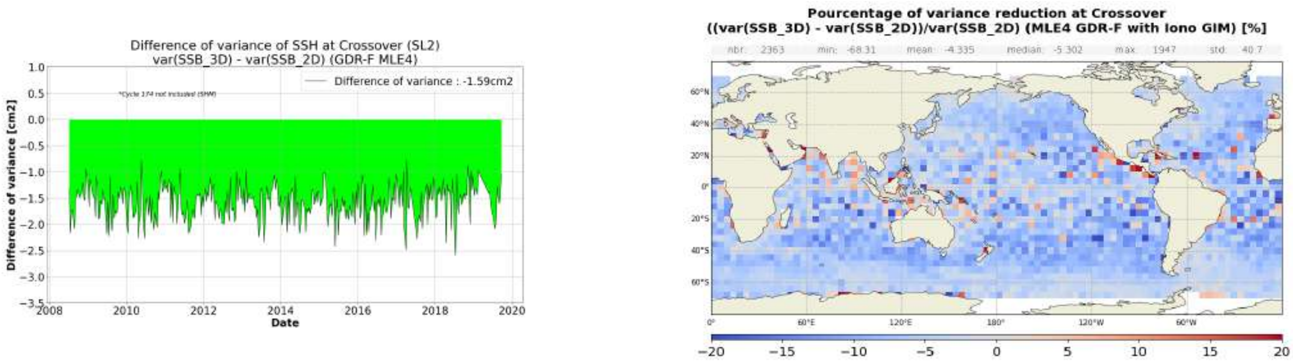

Figure 79: SSH at crossover for SSB_3d and SSB (with iono GIM): difference of variance (SSB_3d - SSB) and pourcentage of error-reduction (SSB_3d - SSB). Note that figures are computed over a common valid points dataset.

Performances on along-track SLA are improved with a reduction of variance of -1.1 cm^2 in average, depending on seasonal signal (figure 80).

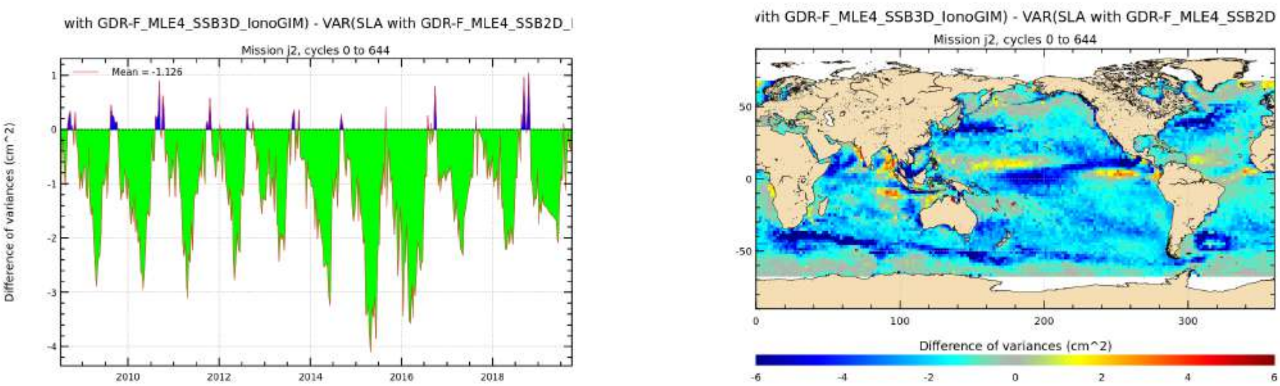

*Figure 80: SLA for SSB_3d and SSB (with iono GIM). Difference of variance (SSB_3D - SSB_2D) on cyclic monitoring (**left**) or geobox averaging (**right**). Note that figures are computed over a common valid points dataset.*

Geographical patterns can be observed on MSL difference between SSB_2D and SSB_3D, specially between North and South hemisphere. Cyclic mean of along-track Sea Level Anomaly is monitored (no include of any remove of annual and semi-annual signals). It highlights a trend difference of -0.42 mm/year for the difference SSB_3D - SSB_2D (figure 81).
Further investigations have to be done in order to better understand how the mean wave period impacts the GMSL trends estimations.

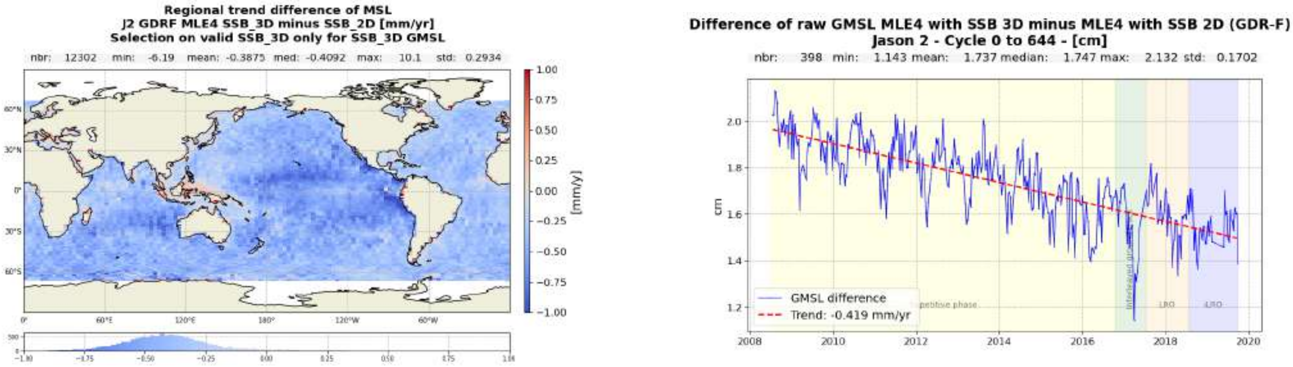

*Figure 81: MSL trend difference GDR-F MLE4 SSB_3D - SSB_2D (**left**) and mean per cycle of GMSL difference GDR-F MLE4 SSB_3D - SSB_2D (**right**)*

8.3. Results on Adaptive retracking

Like for MLE4, all points that are valid (meaning within thresholds) for SSB all also valid using SSB_3d (red curve at left of figure 82). 4586 points per cycle in average are valid with SSB but invalid with SSB_3d in average (blue curve), mainly at high latitudes (see figure 82), against 5040 for MLE4 (see figure 77). This difference is mainly located in low SWH and rain areas, this can be linked to Adaptive validation result (part 7.2.).

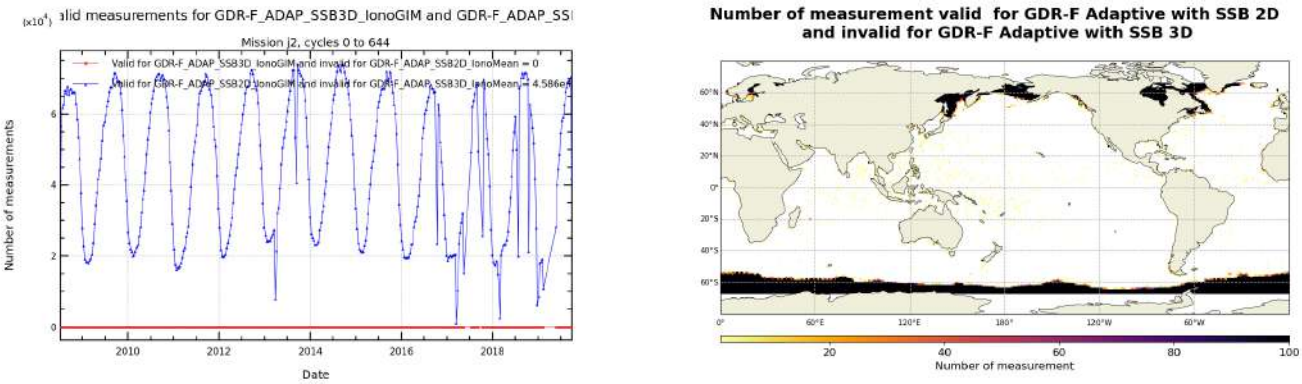

Figure 82: Difference of editing point between SSB and SSB 3D (Adaptive retracking)

Results are quite equivalent with the Adaptive solutions than in previous part on MLE4. The related figures are available below (from figure 83 to figure 86).

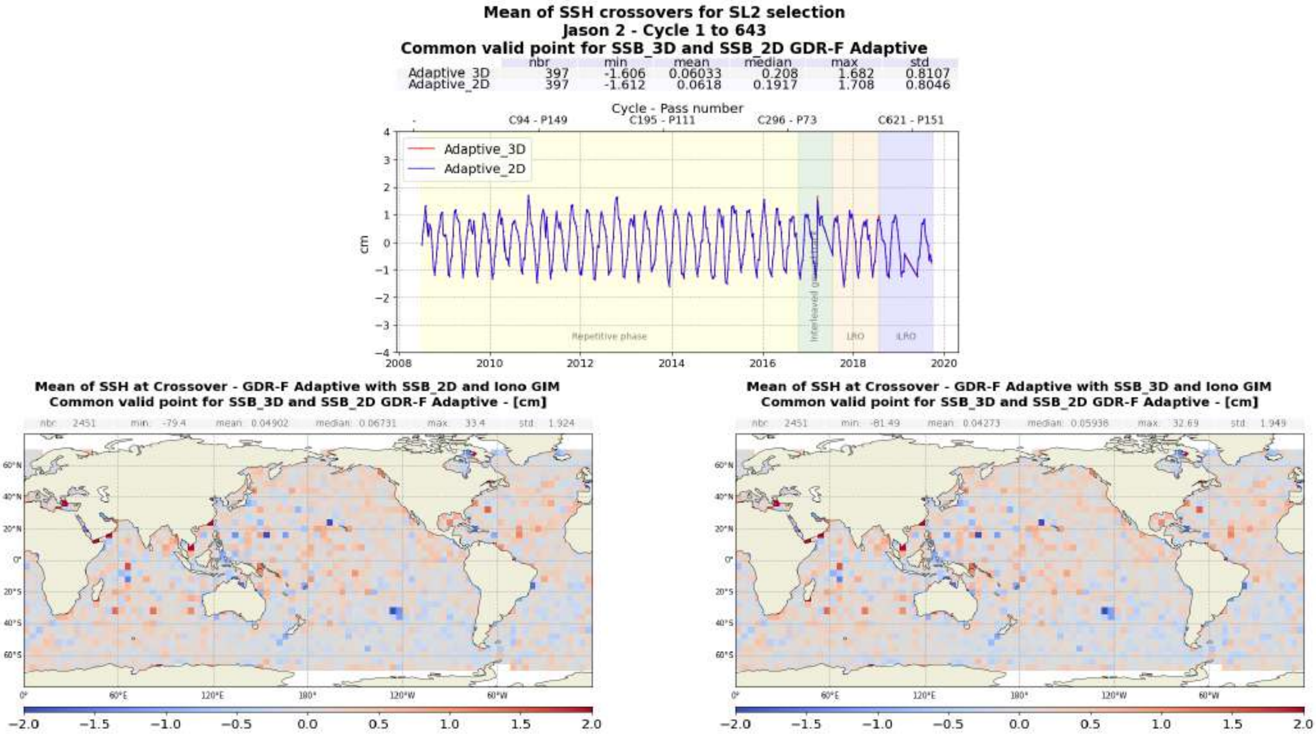

Figure 83: SSH (Adaptive retracking) difference at crossover for SSB_3d and SSB (with iono GIM). Note that figures are computed over a common valid points dataset.

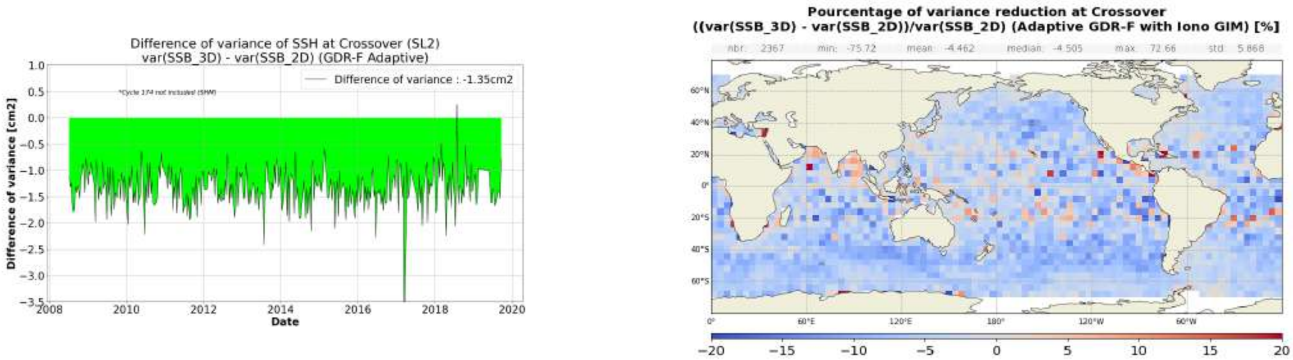

Figure 84: SSH (Adaptive retracking) difference at crossover for SSB_3d and SSB (with iono GIM): difference of variance (SSB_3d - SSB) and pourcentage of error-reduction (SSB_3d - SSB). Note that figures are computed over a common valid points dataset.

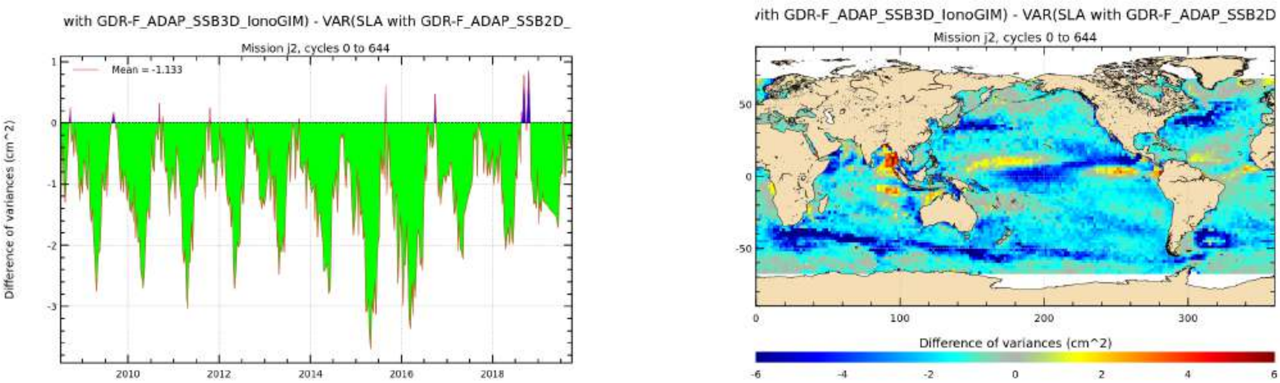

Figure 85: SLA for SSB_3d and SSB. Difference of variance (SSB_3D - SSB_2D) on cyclic monitoring (**left**) or geobox averaging (**right**). Note that figures are computed over a common valid points dataset.

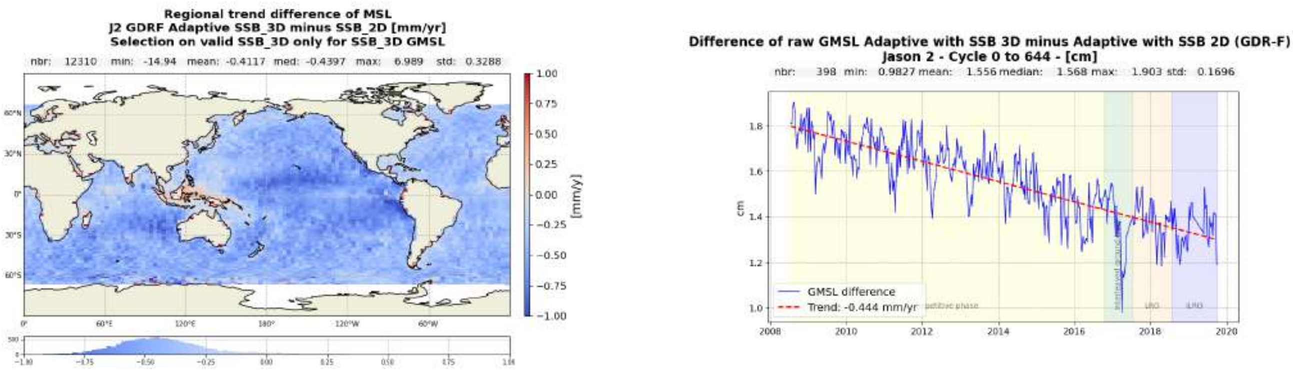

Figure 86: MSL trend difference GDR-F Adaptive SSB_3D - SSB_2D (**left**) and mean per cycle of GMSL difference GDR-F Adaptive SSB_3D - SSB_2D(**right**)

9 Conclusion

An overview of the impact of the GDR-F version of Jason-2 altimeter system over ocean has been presented in this report. Comparisons have been done with previous version data (GDR-D). Comparison during the tandem flight phase with Jason-3 GDR-F data (between February 12 2016 to October 2 2016), taking advantage that both satellite were only 80 seconds apart on the same ground track, have also been presented. Same comparison is done with Jason-1 L2P data (between July 4 2008 to January 26 2009) when there is 55 seconds apart on the same ground track.

The reprocessing of the Jason-2 altimetric mission allows several modifications that improve the sea surface height estimations quality:

- Due to a change in surface classification, more points are identified over ocean.
- Thanks to a new filtered solution for ionospheric correction, measurements are more valid over open ocean on GDR-F dataset than on GDR-D dataset but there are more rejected data in GDR-F near ice and coasts.
- At crossovers, geographically correlated patterns are slightly reduced for mean of SSH differences, global variance decreases everywhere between 5 and 25 %. The main contributor to this variance reduction is the filtering version of the ionospheric correction.
- In terms of along-track performance of Sea Level Anomaly, the variance is also reduced with GDR-F (-14.6 cm^2 using the filtering version of ionospheric correction).

Note the following evolutions:

- The GDR-F and the GDR-D data contain the Precise Orbit Ephemeris standard F (POE-F). Before cycle 254, GDR-D used the Precise Orbit Ephemeris standard D (POE-D), then used the standard E (POE-E) onward.
- Using the latest global tide model FES2014b instead of GOT4.8 allows to reduce variance at crossovers by -0.56 cm^2, and along-track SLA variance by -2.19 cm^2.
- Internal tide is a new correction available in GDR-F compared to GDR-D: it contributes to an improvement of -0.46 cm^2 for variance reduction at crossovers
- The computation of a dedicated sea state bias (fitted on Jason-3 GDR-F data whereas instead of a solution fitted on Jason-2 that was available in GDR-D), the updated associated ionospheric correction and the filtered solution for ionospheric correction contribute to an improvement of -4.46 cm^2 for variance reduction at crossovers, and -3.97 cm^2 for along-track SLA variance
- Pole tide correction was modified between GDR-D (Wahr 1985) and GDR-F (Desai 2015): it contribute to gain of variance for SLA along-track can be observed (-0.12 cm^2).
- GDR-D L2 products included one MSS solution (CNES/CLS 11 before cycle 327 , referenced over 7 years, CNES/CLS15 on cycle 500 onwards) whereas two solutions in GDR-F (CNES/CLS 2015 and DTU 2018) : This change have positive impact on variance of SLA along-track (-13.9 cm^2).

The analysis of the data from Adaptive retracking confirm the benefits of this solution against MLE4 retracking.

Finally, a new solution of SSB (including the mean wave period information) was compared to actual version and leads to quite good results.

10 References

References

[1] Jason-2 handbook available at https://www.aviso.altimetry.fr/fileadmin/documents/data/tools/hdbk_j2.pdf

[2] Jason-2 validation and cross calibration activities (End of mission 2019) https://www.aviso.altimetry.fr/fileadmin/documents/calval/validation_report/J2/SALP-RP-MA-EA-23540-CLS_EndOfLife_J2_CalVal_2019_v1-2.pdf

[3] Boy, François and Jean-Damien Desjonqueres. 2010. Note technique datation de l'instant de reflexion des échos altimètres pour POSEIDON2 et POSEIDON3. Reference: TP3-JPOS3-NT-1616-CNES

[4] Roinard H. Jason-2 validation and cross calibration activities (Annual report 2017). https://www.aviso.altimetry.fr/fileadmin/documents/calval/validation_report/J2/annual_report_j2_2017.pdf

[5] Roinard H. Jason-2 validation and cross calibration activities (Annual report 2016). https://www.aviso.altimetry.fr/fileadmin/documents/calval/validation_report/J2/annual_report_j2_2016.pdf

[6] Roinard H. Jason-2 validation and cross calibration activities (Annual report 2015). https://www.aviso.altimetry.fr/fileadmin/documents/calval/validation_report/J2/annual_report_j2_2015.pdf

[7] Roinard H. Jason-2 validation and cross calibration activities (Annual report 2014). https://www.aviso.altimetry.fr/fileadmin/documents/calval/validation_report/J2/annual_report_j2_2014.pdf

[8] Roinard H. Jason-2 validation and cross calibration activities (Annual report 2013). https://www.aviso.altimetry.fr/fileadmin/documents/calval/validation_report/J2/annual_report_j2_2013.pdf

[9] Roinard H. Jason-2 validation and cross calibration activities (Annual report 2009). https://www.aviso.altimetry.fr/fileadmin/documents/calval/validation_report/J2/annual_report_j2_2009.pdf

[10] https://www.aviso.altimetry.fr/fileadmin/documents/data/tools/hdbk_L2P_all_missions_except_S3.pdf

[11] Roinard H. and Coquelin J. Jason-3 validation of GDR-F data over ocean https://www.aviso.altimetry.fr/fileadmin/documents/calval/validation_report/J3/SALP-RP-MA-EA-23480-CLS_Jason3_Reprocessing_Report_v1-2.pdf

[12] Roinard H. Jason-3 validation and cross calibration activities (Annual report 2017). https://www.aviso.altimetry.fr/fileadmin/documents/calval/validation_report/J3/SALP-RP-MA-EA-23187-CLS_Jason-3_AnnualReport2017_v1-2.pdf

[13] Roinard H. Jason-3 validation and cross calibration activities (Annual report 2019). https://www.aviso.altimetry.fr/fileadmin/documents/calval/validation_report/J3/SALP-RP-MA-EA-23399-CLS_Jason-3_AnnualReport2019_v1-1.pdf

[14] Roinard H. Jason-3 validation and cross calibration activities (Annual report 2020). https://www.aviso.altimetry.fr/fileadmin/documents/calval/validation_report/J3/SALP-RP-MA-EA-23473-CLS_Jason-3_AnnualReport2020_v1-1.pdf

[15] Ablain M. SALP annual report (2017) of Mean Sea Level Activities. https://www.aviso.altimetry.fr/fileadmin/documents/calval/validation_report/SALP-RP-MA-EA-23189-CLS_AnnualReport_2017_MSL.pdf

[16] Nencioli Francesco, Roinard Hélène, Bignalet-Cazalet Francois. 2021. Filtering ionospheric correction from altimetry dual-frequencies solution. DOI 10.24400/527896/a02-2021.001. https://www.aviso.altimetry.fr/fileadmin/documents/data/tools/NT-Nencioli_FilteredIonosphericCorrection.pdf

[17] Mean sea level rise and the Greenhouse effect https://www.aviso.altimetry.fr/en/applications/ocean/mean-sea-level-greenhouse-effect.html

[18] P. Thibaut et al., Benefits of the "Adaptive Retracking Solution" for the JASON-3 GDR-F Reprocessing Campaign, 2021 IEEE International Geoscience and Remote Sensing Symposium IGARSS, 2021, pp. 7422-7425, doi: 10.1109/IGARSS47720.2021.9553647. https://ieeexplore.ieee.org/document/9553647. Available at https://www.aviso.altimetry.fr/fileadmin/documents/data/tools/NT-Thibaut_AdaptiveRetrackingForJason3GDRF.pdf

[19] Benefits of the Adaptive Algorithm for Retracking Altimeter Nadir Echoes: Results From Simulations and CFOSAT/SWIM Observations. IEEE Transactions on Geoscience and Remote Sensing. 2021 | journal-article. DOI: 10.1109/TGRS.2021.3064236

[20] DUACS/Aviso team : 'A new version of SSALTO/Duacs products available in april 2014' https://www.aviso.altimetry.fr/fileadmin/documents/data/duacs/Duacs2014.pdf

[21] Pujol et al. OSTST2013. A 20-YEAR REFERENCE PERIOD FOR SSALTO/DUACS PRODUCTSSSALTO/DUACSPRODUCT https://www.aviso.altimetry.fr/fileadmin/documents/OSTST/2013/oral/pujol_ChgtRef.pdf

[22] Filtered dual-frequency altimeter range measurement [Guibbaud et al. 2015]

[23] Desai, Shailen and Wahr, John and Beckley, B.. (2015). Revisiting the pole tide for and from satellite altimetry. Journal of Geodesy. 89. DOI:10.1007/s00190-015-0848-7. And J. C. Ries and S. Desai: Conventional model update for rotational deformation. In Fall AGU Meeting, New Orleans, LA, 2017

[24] Cartwright and Edden [1973] Corrected tables of tidal harmonics - J. Geophys. J. R. Astr. Soc., 33, 253-264.

[25] Lyard F. H. and all. FES2014 global ocean tide atlas: design and performance https://os.copernicus.org/articles/17/615/2021/os-17-615-2021.html

[26] Loren Carrere, Brian K. Arbic, Brian Dushaw, Gary Egbert, Svetlana Erofeeva, Florent Lyard, Richard D. Ray, Clément Ubelmann, Edward Zaron, Zhongxiang Zhao, Jay F. Shriver, Maarten Cornelis Buijsman, and Nicolas Picot. Accuracy assessment of global internal-tide modelsusing satellite altimetry. Ocean Sci., 17, 147–180, 2021 https://doi.org/10.5194/os-17-147-2021 https://os.copernicus.org/articles/17/147/2021/os-17-147-2021.pdf

[27] Tran N., D. Vandemark, E.D. Zaron, P. Thibaut, G. Dibarboure, and N. Picot (2019): "Assessing the effects of sea-state related errors on the precision of high-rate Jason-3 altimeter sea level data", Advances in Space Research / special issue " 25 Years of Progress in Radar Altimetry", Volume 68, Issue 2, Pages 963-977, https://doi.org/10.1016/j.asr.2019.11.034, 2021